Study of Magnetic, Electric and Thermal Properties in Fe$_3$Se$_4$ System: Interplay of Spin, Charge and Phonon

Thesis Submitted to AcSIR
For the Award of the Degree of
DOCTOR OF PHILOSOPHY
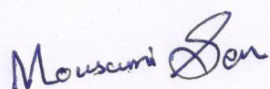**In Physical Sciences**

AcSIR

By
Mousumi Sen
Registration Number: 10PP12A26083

Under the guidance of
Dr. Pankaj Poddar
Physical and Materials Chemistry Division
CSIR-National Chemical Laboratory
Dr. Homi Bhabha Road
Pune 411008

Dedicated to my beloved grandfather
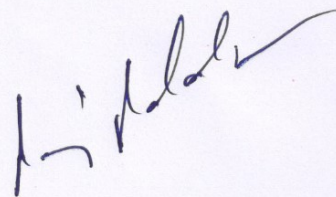*Late Anil Kumar Sen,*
Maa, Baba and Arit

CERTIFICATE

This is to certify that the work incorporated in this Ph.D. thesis entitled **Study of magnetic, electric and thermal properties in Fe_3Se_4 system: Interplay of spin, charge and phonon** submitted by **Ms. Mousumi Sen** to Academy of Scientific and Innovative Research (AcSIR) in fulfillment of the requirements for the award of the Degree of *Doctor of Philosophy in Physical Sciences*, embodies original research work under my supervision/guidance. I further certify that this work has not been submitted to any other University or Institution in part or full for the award of any degree or diploma. Research material obtained from other sources has been duly acknowledged in the thesis. Any text, illustration, table etc., used in the thesis from other sources, have been duly cited and acknowledged.

Mousumi Sen

(Student)

Dr. Pankaj Poddar

(Supervisor)

DECLARATION

I hereby declare that the work described in this thesis entitled **"Study of magnetic, electric and thermal properties in Fe_3Se_4 system: Interplay of spin, charge and phonon"** submitted for the degree of ***Doctor of Philosophy in Physical Sciences*** has been carried out by me at the Physical and Materials Chemistry Division of the CSIR-National Chemical Laboratory, Pune, India under the supervision of Dr. Pankaj Poddar. Such materials as have been obtained by other sources have been duly acknowledged in this thesis. The work is original and has not been submitted in part or full by me for award of any other degree or diploma in any other University.

Date: 20 – 02 - 2017

Place: Pune

Mousumi Sen

(Research Student)

ACKNOWLEDGEMENT

champ) for always keeping the lab cheerful. I will never forget the experiences we've shared and hope to stay in touch. I thank my closest friends Padhye, and Puneet for the stimulating discussions, for the sleepless nights we were working together before deadlines, and for all the fun we had in the last five years. These friends have been there for me when the challenges of PhD seemed too big to overcome. I would like to thank my friends Sandip, Shyamu, Vandita and Deep for their constant encouragement.

A special thanks to Preeti for being together in good, bad and grand times. ☺ With you I learned, I experimented, I discussed and we enjoyed. Many of things worked out, many didn't, but the memories will be there for life. A special thanks to Nikhil too, for listening to our tantrums every day, and enjoying and celebrating. Thank you two for being there.

I would like to express the deepest gratitude to my Maa and Baba for believing in me and allowing me to pursue my ambition. Your encouragement, counselling, consolation and guidance provided support, encouragement and interest in my thesis work. I would not be who am I today without your blessings. I would also like to thank my sisters Dada and Manu for their constant help and support and being with me in my hard times. I thank my mother and father-in-law, Arin and Aparna for their encouragement and continued support over the years.

I especially thank my extended family in Pune, Raja (P) and Subhoshree for their endless emotional support and making time for me whenever I needed.

Finally, I specially acknowledge my husband Arit for his unconditional support, love and care. In the days of my frustration, depression and disappointments he has been the pillar of strength for me and helped starting a day with new hope again. His un-ending passion for knowledge and hard work is an inspiration for me. Thank you for sharing my responsibilities at home and never giving up on me. Your call for small celebrations even for my little achievements made my day. You have been my best friend, philosopher and guide. ☺

How could I forget to thank my nephew and niece Dev and Tanvi whose unconditional love and innocence brings smile on my face in any difficult situations.

*I will always be indebted to my grandfather (**Karta**) whose whole life is a teaching to me. You were an ocean of knowledge who taught me my values and life goals and ways to achieve them. Even in childhood, I could see and feel the bigger outside world through you. The simple stories you always told made me understand mythologies, geography, philosophy, science and what not so easily. It is your blessings that hold my hand and show me the way through all journeys.*

I could not have completed my research without the support of all these wonderful people! Last but not least, I want to thank almighty God for blessing me with this beautiful life.

*….. **Mousumi Sen***

PREFACE

The monoclinic phase of iron selenide (Fe_3Se_4) has been studied for last seven decades now; still, this material is full of surprises. Although the oxygen counterpart of the material, magnetite (Fe_3O_4), has always been in the limelight among the researchers for its widespread applications, Fe_3Se_4 is relatively very less explored and understood. In this thesis, efforts are dedicated to understand the physical properties and explore new properties which were not studied before in monoclinic iron selenide. It will be evident from the results discussed in the coming chapters; Fe_3Se_4 holds tremendous potential for both fundamental studies and technical applications.

In the **first chapter**, the transition metal chalcogenides are introduced and their applications in various fields are discussed. It is highlighted in the chapter as why Fe_3Se_4 is fundamentally and technologically an important compound to study. Brief literature review of Fe_3Se_4 is given and scope of the thesis is discussed.

The **second chapter** consists of two main sections with the objective of improving the energy product by modification of Fe_3Se_4. In the first section, the effect of manganese ion doping on the magnetic properties are studied in detail. Various samples with different manganese concentration were prepared and the optimum doping concentration was found for which the energy product was maximum without changing the Curie temperature. In the second section, a nanocomposite was made from Fe_3Se_4 and Fe_3O_4 nanoparticles forming a hard: soft exchange spring magnet. A single-phase behavior is obtained in magnetism although two crystallographically different phases were present in the composite.

The **third chapter** deals with the change in magnetic entropy and specific heat capacity in Fe_3Se_4 nanoparticles were studied in a broad temperature (215-340 K) and magnetic field range (0-60 kOe). The isothermal magnetic entropy change (ΔS_M) is estimated by an indirect method from the isothermal magnetization curves measured in this temperature range. The ΔS_M was obtained $- 46 \times 10^{-2}$ J/kg.K at ~317 K when the field was changed from 0 to 60 kOe. The nature of this transition was analyzed by universal curve behavior. The temperature and magnetic field dependence of specific heat capacity was studied and analyzed to estimate the adiabatic temperature change (ΔT_{ad}).

In the **fourth chapter**, a very important discovery is discussed. For the first time, spontaneous and reversible polarization in Fe_3Se_4 is observed. Experimental evidences of the coexistence of magnetic and ferroelectric ordering and magneto-electric coupling at room temperature in Fe_3Se_4 nanorods are discussed. We observed that the ferroelectric and magnetic Curie temperature coincide and shows a coupling manifested by an anomaly in the dielectric constant and Raman shift at T_C. We do not completely understand the origin of the ferroelectric ordering at this point however the simultaneous presence of magnetic and ferroelectric ordering at room temperature in Fe_3Se_4 along with hard magnetic properties will open new research areas for devices.

Chapter 6 will describe the conclusion of the overall work presented in this thesis. The future direction of this thesis also presented in this chapter.

LIST OF ABBREVIATIONS

1.	Ferroelectricity	FE
2.	Ferromagnetism	FM
3.	Antiferromagnetic	AFM
4.	Magneto-electric	ME
5.	X-ray diffraction	XRD
6.	Transmission electron microscope	TEM
7.	Selected area electron diffraction	SAED
8.	Physical Property Measurement System	PPMS
9.	Vibrating sample magnetometer	VSM
10.	Zero field-cooled and Field-cooled	ZFC-FC
11.	AC measurement system	ACMS
12.	Magnetization vs. field	M-H
13.	Full-width half maximum	FWHM
14.	Magnetization vs. temperature	M-T
15.	Room temperature	RT
16.	Coercivity	H_C
17.	Energy product	BH_{MAX}
18.	Magnetocaloric effect	MCE
19.	Inverse magnetocaloric effect	IMCE
20.	Entropy change	ΔS_M
21.	Adiabatic temperature change	ΔT_{ad}
22.	Relative cooling power	RCP
23.	Specific heat	C_P
24.	Differential scanning calorimeter	DSC

Table of contents

Chapter1: Introduction

In this chapter, brief introduction to the transition metal chalcogenides and their vast area of applications is given. The iron-selenium binary phases are discussed in details. The uniqueness of Fe_3Se_4 is highlighted and brief history of this material is presented. The crystal structure, magnetic structure, synthesis methods, and, magnetic properties of this sample is studied in details. The scope of this thesis is mentioned at the end of this chapter.

Mousumi Sen

1.1. Transition metal chalcogenides

The energy issue is the most important agenda in the current scenario and chief concern among the scientific community. There is a burning requirement for a cost-effective, efficient, environment-friendly energy conversion and storage devices that can power energy demanding areas. The performance of these devices depends hugely on the properties of the materials used. Among these materials, metal chalcogenides (MC), particularly the late transition metal chalcogenides consisting of metal atoms (Fe, Co and Ni) and chalcogen atoms (S, Se, Te) have renewed interest as very attractive candidates for applications in devices including fuel-cells, solar-cells, light-emitting-diodes, sensors, memory-devices, thermoelectric devices, supercapacitors, Li- ion batteries, magnetic materials etc.; and for these reasons these compounds are studied extensively in last few decades[1,2].

Some of the metal sulphides are active photovoltaic materials, and, are cheap and abundant as they are generally present as minerals in earth crust for example— chalcocite (Cu_2S) and pyrite (FeS_2)[3–5]. Pyrite (also known as fool's gold) has a suitable band gap (~0.95 eV), strong light absorption leading to display of high quantum efficiencies in devices (~ 90%). The fabrication of this material is inexpensive and can be done on large surfaces by roll to roll deposition of nanoparticle ink or paint on flexible substrates[3]. Metal chalcogenide semiconductors, for examples CdS, CdSe, PbS, ZnS, are becoming increasingly popular as it is easy to convert them into quantum dots at ambient conditions for application in narrow wavelength (pure colour) LED's for display[6–8].

Materials such as cobalt sulphide (Co_9S_8) and nickel sulphide (Ni_3S_2) have gained attention as cathode materials because of their metallic conductivity[9]. Cobalt selenides,

Mousumi Sen

tellurides and their hybrids show impressive oxygen reduction reaction (ORR) activity and act as catalyst for fuel cells[10,11].

Ultrathin 2-dimensional layered transition metal dichalcogenides (TMD's) are fundamentally and technologically fascinating[2,12–14]materials. TMD's have two in-equivalent valleys in the *k*-space with large separation between them leading to important applications in the field of valley-coupled spintronics applications[15–17]. The interlayer space in TMD's helps in hosting varieties of guest species, thus making them good energy storage materials[12,18,19]to be used in Li-ion batteries, supercapacitors etc.

Compounds belonging to the family M_2X_3 (where M = Bi, Pb, Sb and X = S, Se, Te)are potential low bandgap thermoelectric (TE)materials[20–22]. The criteria to be a good TE material are low electrical resistivity and high Seebeck coefficient. The telluride materials are considered as best thermoelectric materials and occupy the most of market shares. But, because of the shortage and toxicity of tellurium, alternate materials and developed and researched. Especially, the thermoelectric properties enhances when these materials are formed as oriented nanostructures[23–25]. Enhanced thermoelectric properties were observed for highly crystalline and oriented nanostructures of Bi_2S_3which is closely related to the structure of dense array of *c*-axis oriented nanorods[20]. The chemical bonds in Bi_2S_3 are highly anisotropic, the covalent bonds are directed across *c*-axis and along *a* and *b*-directions bonding are made of weak ionic and van-dar Waal's forces. It has been proved that career mobility in *c*-axis direction is higher than a-axis because of effective-mass anisotropy. Thus, oriented nanostructures are preferable for enhancing the transport property and hence good TE properties. Because of the simplicity and reliability of thermoelectric materials they are extensively used in the space power generation, cooling

Mousumi Sen

applications, temperature control in LASER, modern cars and variety of other power generation applications.

According to some recent studies, bismuth selenide (Bi_2Se_3) can serve as a parent matrix compound for topological devices, where the career transport will have a purely quantum topological origin[26–28]. These topological insulators are a new class of quantum matter where the surface states are robust and protected by time-reversal symmetry and possess immense potential in the field of dissipation-less electronics and spintronics.

The discovery of high temperature superconductivity in α-FeSe[29,30] phase evoked a huge interest among the researchers about the iron-selenium phases. Iron-selenium systems present us the most unique diversity ranging from superconductor to semiconductor to metallic behavior and permanent magnet like characteristics[31–33]. Recently, large ferrielectric polarization was predicted in $BaFe_2Se_3$,which was surprising as till now this material was investigated as a member of the high-temperature iron-based superconductor family[34].Few other members of iron-selenium family (such as $CdCr_2Se_4$)were also found to show some interesting multiferroic behaviors[35,36] which we will discuss in detail in chapter 4.

The MC's has shown their potential in the field of biomedical applications too. Nanoparticles of bismuth selenide have been used for realizing both real-time monitoring of tumor and therapeutic functions[37]. The drug loaded on Bi_2Se_3 nanoparticles were capable of thermo-chemotherapy and real-time imaging simultaneously. Iron sulphide and cobalt selenide nanoparticles have been used as theranostic platform to perform both imaging and photothermal therapy[38,39]. High near infra-red absorbance combined with super-paramagnetic nature of iron sulphide nanoparticles make it suitable for magnetic resonance imaging.

Mousumi Sen

The vast areas of application in the field of transition metal chalcogenides is summarized in tabulated form in figure 1.1.
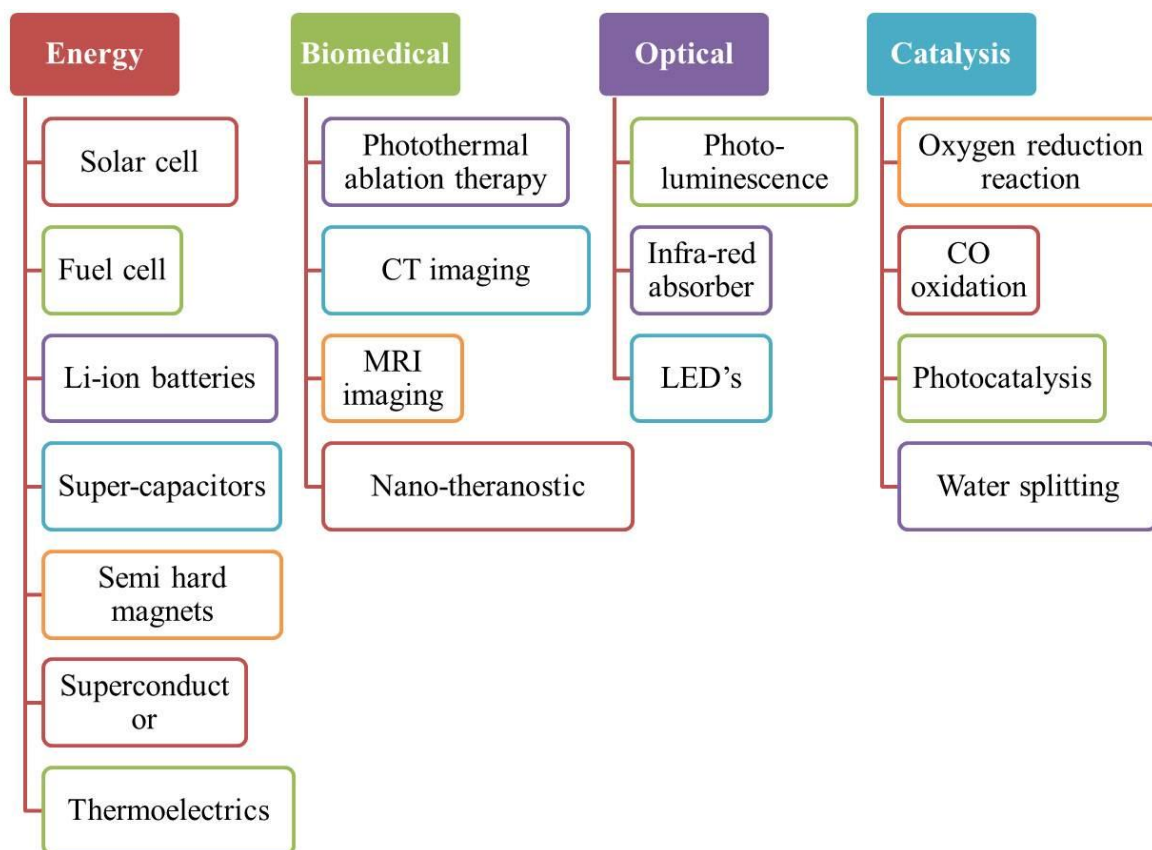
Figure 1.1: Schematic to show the diversity in applications of transition metal chalcogenides. Some of the areas are indicated under each class where these materials are used.

1.2. Why are chalcogenides so different from oxides?

By the term chalcogenides, we refer generally to the sulphides, selenides and tellurides of the material. The chalcogenides are distinctly different from their oxide counterparts. The reasons behind the differences between chalcogenides and oxides can be understood by simple qualitative arguments given by Jellinek in his review article in 1988[31]. Mostly these differences occur because of the differences between oxygen atom and chalcogen atoms (S, Se, Te). The chalcogen atoms are larger and heavier than oxygen atom and also, they are less electronegative than oxygen. As a result, the metal-chalcogen bonds have more covalent character than metal –oxygen bonds. Usually in transition metal chalcogenides oxygen has the oxidation state of -2, but, due to its smaller size and electronegativity chalcogen atoms can have less negative oxidation states (for e.g. -1). Chalcogen atoms also possess accessible *d* orbitals in contrast to oxygen, which are often used to make metal-chalcogen bonds.

The energy-gap between the top of the valence band and bottom of the conduction band is smaller in chalcogenides as compared to oxides. As oxygen is more electronegative than chalcogens, its valence band lies at lower energy than chalcogens whereas, the conduction bands remains mainly unchanged. This reduced bandgap in chalcogenides gives rise to many disparate optical and electrical properties in chalcogenides.

To highlight the difference, a comparison between Fe_3O_4, Fe_3S_4 and Fe_3Se_4 magnetic properties are tabulated in table 1.1.

Mousumi Sen

Compound	Magnetic ordering temperature	Saturation magnetization at room temperature
Fe_3O_4(bulk)	$T_C \sim$ 858 K	$\sim$ 90 emu/g[40]
Fe_3S_4(bulk)	$T_C \sim$ 600 K	$\sim$38 emu/g[41]
Fe_3Se_4 (bulk)	$T_C \sim$ 330 K	$\sim$ 7 emu/g

Table 1.1: Comparison of magnetic properties of Fe_3O_4, Fe_3S_4 and Fe_3Se_4

1.3. The binary Fe-Se system:

The iron – selenium system was studied by thermo-analytical and X-ray diffraction methods. Combining all the measurement results, a phase diagram (temperature-concentration) was constructed from 623-1323 K and 20-66 atomic % selenium in the decade of 1970[S31,42]. Three important phases in Fe-Se systems with different structures were identified. These three phases, their structures and stability ranges are discussed here.

a) The tetragonal monoselenide:

This phase has 49.02 atomic % of selenium with PbO structure with approximate composition $Fe_{1.04}Se$. In this phase the surplus iron atoms are present in the interstitial positions. This phase caught the worldwide attention of researchers after the discovery of superconductivity in this phase with transition temperature 8 K[29]. The crystal structure of α-FeSe is composed of layers of edge sharing $FeSe_4$-tetrahedra. This material has the

Mousumi Sen

simplest crystal structure among the iron based superconductors. With the application of high pressure (1.48 GPa), the upper critical temperature of FeSe is raised to 27 K[30].

b) Phases with NiAs-related structure:

These phases are described by the general formula $Fe_{1-x}Se$ with a wide range of homogeneity between 51 to 59 atomic % of selenium. In the composition Fe_7Se_8 (53.3 %), hexagonal NiAs structure is found and in Fe_3Se_4 a monoclinic deformation to the NiAs structure is found. These phases are characterized by the presence of metal ion vacancies in the structure. The ordering of iron vacancies leads to the ferrimagnetism in both stoichiometric compound Fe_3Se_4 and Fe_7Se_8. There iron vacancies are confined to every alternate layer of metal atom in monoclinic Fe_3Se_4

c) Phases with orthorhombic marcasite structure:

This phase is the richest in selenium content and has a very narrow homogeneity range (66.6 at% selenium).Iron diselenide ($FeSe_2$) adopts marcasite structure at room temperature and shows semiconducting properties with bandgap ~1 eV[32,43–45]. In the lattice, each iron atom is surrounded octahedrally by 6 Se atoms and each Se atom is attached tetrahedrally to 3 iron atoms and one Se atom. $FeSe_2$ shows a broad absorption at ~1100 nm[46]. The optical properties make $FeSe_2$suitable for solar energy applications.

Figure 1.2 shows the iron-selenium phase diagram constructed by Wilfried *et. al.*[31]combining all the available data in literature. At very high temperatures, the only solid state that exists is the NiAs-type structure. The tetragonal phase undergoes a reaction forming NiAs-structure and iron at 458 °C. Fe_3Se_4 goes through a λ-transition at 704 °C into hexagonal structure. $FeSe_2$ melts incongruently at 585 °C and forms NiAs-structure and selenium rich liquid.

Mousumi Sen

Figure 1.3 sums up the three important phases found in the binary Fe-Se system.
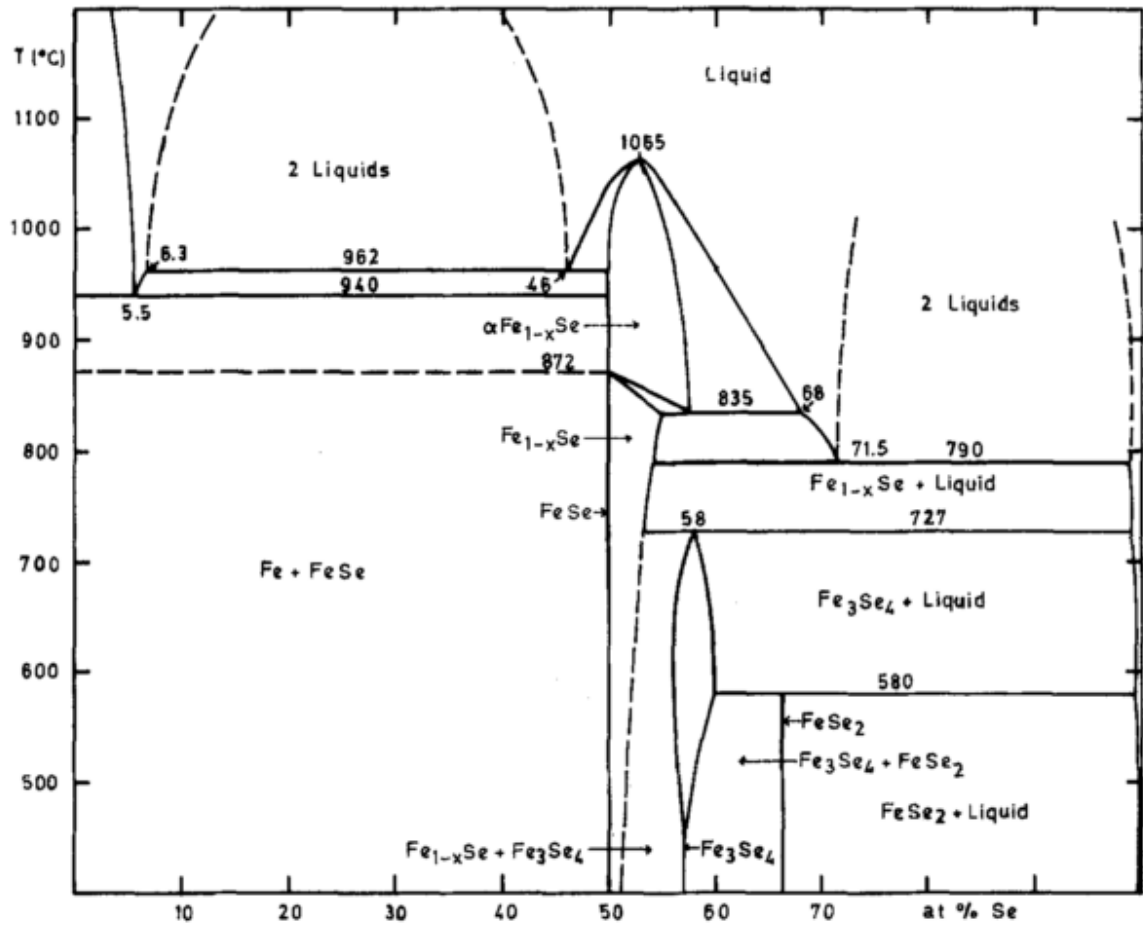
Figure1.2: Iron--Selenium phase diagram[31].

Mousumi Sen

Fe-Se system

Tetragonal phase α-FeSe with PbO-structure,

NiAs-type β-phase with a wide range of homogeneity showing a transformation from hexagonal to monoclinic symmetry

An FeSe$_2$ phase that has the orthorhombic marcasite structure

Superconductivity with transition temperature at ~8 K

Fe$_3$Se$_4$ and Fe$_7$Se$_8$ are ferrimagnets with T$_C$~ 315 K and 443 K

P- type semiconductor, E$_g$ ~ 1 eV

Figure1.3: Schematic shows three important phases from the binary Fe-Se phase diagram with different crystalline structure and physical properties.

Mousumi Sen

1.4: Why is Fe_3Se_4 unique?

Fe_3Se_4 is a historic material which has been studied for its magnetic properties since last 7 decades[47]. Since the early 1950s, it was known that the β-phase having NiAs-type structure shows ferrimagnetic properties[48].The structural studies of these phases done by Okazaki and Hirakawa in 1956 stated that the ferrimagnetism in these compounds is the result of ordered iron vacancies in the structure[49]. The X-ray diffraction patterns from the single crystals of Fe_3Se_4 and Fe_7Se_8showed strong spots corresponding to the NiAs-type structure along with some very weak spots which were designated to the superstructures due to the presence of Fe-vacancies. The vacancies are dispersed as widely as possible. The lattice parameters of the superstructure are twice as large as that of the fundamental structure along *a* and *b* axis and three times along *c*-axis for Fe_7Se_8 and two times for Fe_3Se_4[49]. Subsequent neutron diffraction experiment on Fe_3Se_4 in the year 1968 probed the magnetic unit cell, which was found to be same as structural unit cell. Moments in the *c*-plane are collinear pointing along *b*-axis and ferromagnetically aligned whereas, moments in the neighboring planes are antiferromagnetically aligned[50,51].

After decades, iron selenide compounds started gaining attention after the discovery of superconductivity in tetragonal PbO-phase $FeSe_{1-x}$[29,30]. Being non-toxic and having the simplest crystal structure among other Fe-based superconductors, iron chalcogenides gained popularity rapidly.

Then, the monoclinic phase of iron selenide (Fe_3Se_4) showed some very promising new properties, when reduced to nano-dimension[33,52].The reason Fe_3Se_4 is special is that it shows semi-hard magnetic properties at room temperature without the presence of rare-earth atoms or noble metal atoms at nano-dimensions. These properties are explored in details in coming sections.

Mousumi Sen

1.5. Structure of Fe_3Se_4

1.5.1. Crystal structure of Fe_3Se_4

The structures of metal chalcogenides can be broadly classified into two structural classes, nickel arsenide and cadmium iodide. These two structures are closely related and can be converted into one another. The arrangement of chalcogens are same in both the structures, but, one extra layer of metal atom inserted between the cadmium iodide layer structure will convert the structure to nickel arsenide. The filling of this van der Waals' region by additional metal atoms destroys the layered structure of the compound[53].
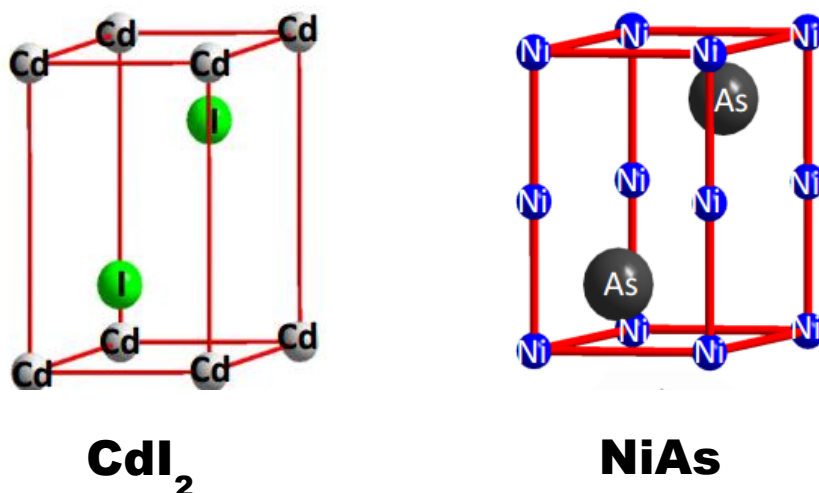
Figure 1.4: Arrangement of atoms in cadmium iodide and nickel arsenide structure.

If one fourth of metal atoms are removed from the closed pack structure of NiAs, the resulting structure is M_3X_4 type (M is metal ion and X is chalcogen) (figure 1.5). When the cations are removed from alternate metal layers in ordered manner, vacancies are confined to every second metal layer and are ordered, leading to monoclinic symmetry[54](Cr_3S_4 type structure).

Mousumi Sen

NiAs   Cr₃S₄
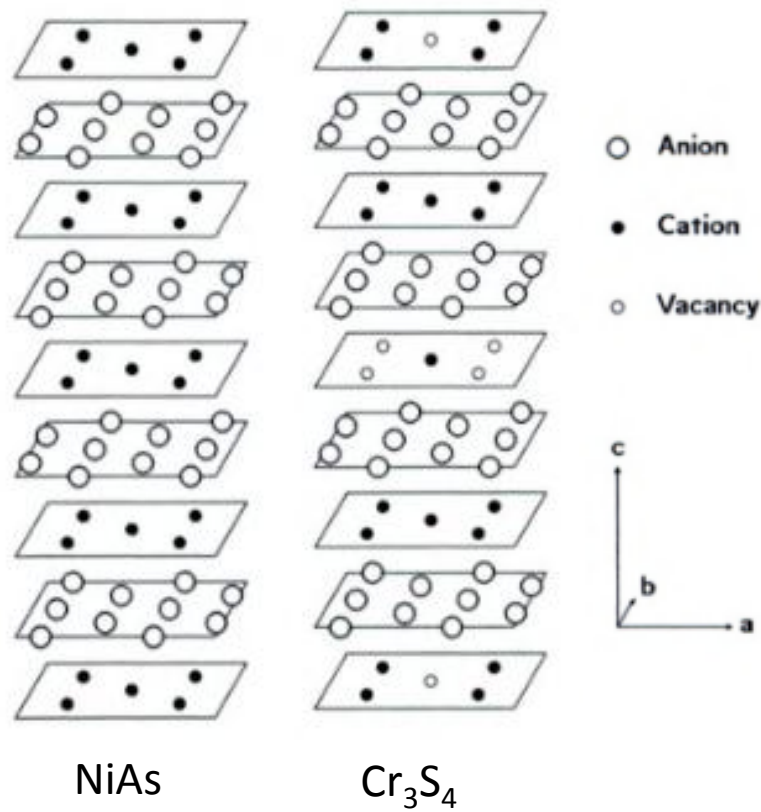
Figure 1.5: Idealized representation of close packed NiAs and Cr_3S_4 structures[54].

X-ray diffraction analysis was studied by Okazaki and Hirakawa[49] on the single crystal specimens of iron selenides. X-ray data were collected by Laue oscillation methods using Co K-radiation. Fe_3Se_4 has a monoclinic structure with Laue symmetry C_{2h}-2/m. The lattice parameters of the unit cell containing two chemical units, Fe_3Se_4, were found to be

A= 6.17, B= 3.53, C= 2c= 11.1 Å and β= 92.0°

Mousumi Sen

The rotation photographs around the *c*-axis showed the splitting of spots corresponding to the monoclinic deformation of the fundamental lattice. From the structure, Fe_3Se_4 is expected to cleave along $(\bar{1}01)$ planes. The unit cell of Fe_3Se_4 is shown[33,49] in figure 1.6.
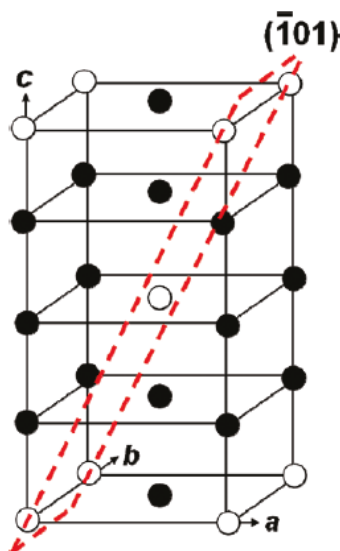
Figure 1.6: Schematic of the unit cell of Fe_3Se_4. Open and solid circles represent vacancies and Fe atoms. Se atoms are omitted for clarity. Ref [33,49]

Open and solid circles represent vacancies and Fe atoms. Se atoms are omitted for clarity. In a Fe_3Se_4 unit cell, the vacancies of Fe appear in every other Fe-layer, and the number of vacancies alternates between different layers. The lattice vacancies are aligned along the b-axis and adopt a body-centered structure in a unit cell. All these vacancies lie in the $(\bar{1}01)$ plane as shown in Figure 1.6. Due to the presence of vacancies, the surrounding environment of chalcogen atom (Se) becomes polar. To conserve the charge balance, the structure adopts a mixed oxidation state of the transition metal (Fe).

Mousumi Sen

1.5.2. Magnetic structure of Fe_3Se_4 by neutron diffraction

Neutron diffraction experiments[50] on bulk polycrystalline samples revealed that the chemical unit cell is very similar to that of the Cr_3X_4 (X= S, Se and Te), but, in Fe_3Se_4, no enlargement of the unit cell due to magnetic ordering takes place as in case of Cr_3X_4compounds. Two diffraction patterns are recorded at 81 K and 371 K (below and above Curie temperature)(figure 1.7). The only observed extra peaks were due to $\lambda/2$ peaks, so it was concluded that magnetic ordering does not result into enlargement of the unit cell. The magnetic moments are aligned ferromagnetically within each c-plane and antiferromagnetically aligned in neighboring planes. The direction of moment is in the c-place and probably along the face diagonal. Later investigations showed that the moments point along the b-axis[51]. Going from Fe_7Se_8 to Fe_3Se_4, the structural changes associated are very small which are pointed below.

- Slight monoclinic deformation.

- Number of vacancy and their distribution in the vacancy layers differ.

- Contraction of lattice along the c-axis. Fe-Fe distance in this direction reduces from 2.94 to 2.79 Å.

One formula unit of Fe_3Se_4 can be written as $Fe^{2+}Fe_2^{3+}LSe_4^{2+}$, where L denotes a vacancy. Figure 1.8 shows the alignment of magnetic moments in a unit cell.

Mousumi Sen
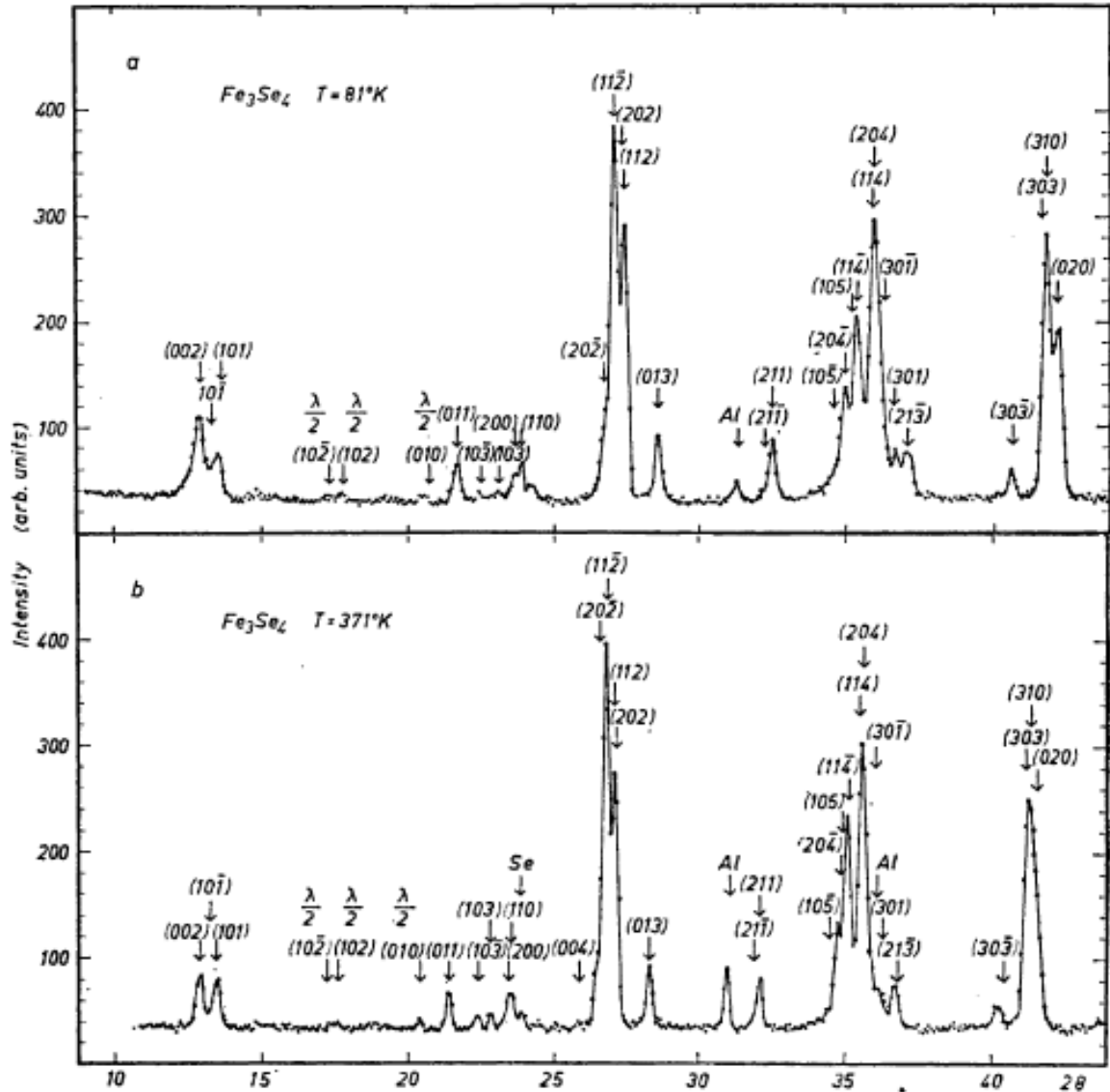
Figure 1.7: Neutron diffraction spectrum at temperatures81 K and 371K.[50]

The moment values derived from the neutron diffraction measurement are close to observed value[55] of 3.25 μ_B for Fe^{2+} and 1.94 μ_B for Fe^{3+}.
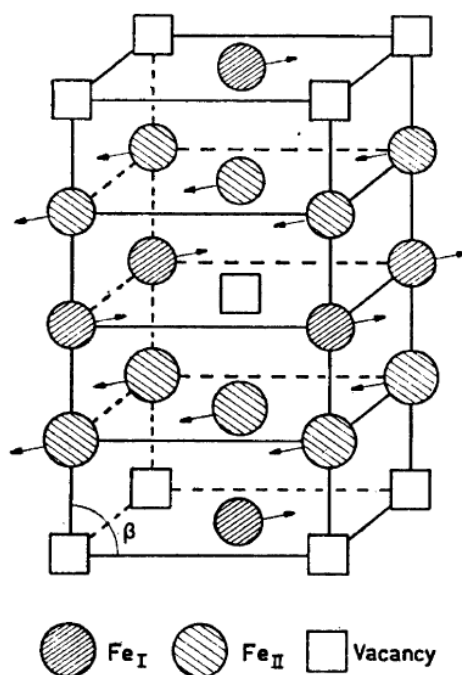
Figure 1.8: Unit cell of Fe_3Se_4 showing the orientation of magnetic moments.

1.6. Synthesis processes of Fe_3Se_4

1.6.1. Synthesis of single crystal of Fe_3Se_4

Single crystals of Fe_3Se_4were prepared by elemental synthesis at elevated temperatures in silica tubes[49,56]. The powdered mixture of electrolytic iron (reduced by hydrogen) and selenium (redistilled 99.997%) in proper proportion were sealed in an evacuated silica tube. The mixtures were heated to 1150°C and temperature was maintained for 70 hours and then cooled down to room temperature very gradually taking 5 days. The single crystal of Fe_3Se_4 displays metallic lustre.

Mousumi Sen

1.6.2. Synthesis of bulk polycrystalline Fe$_3$Se$_4$

Powder samples of bulk polycrystalline Fe$_3$Se$_4$ are produced from hydrogen reduced iron fillings obtained from 99.999% pure iron rods and spectrographically standardized selenium[50]. Accurately weighed quantity of reactants are sealed in a double walled quartz tube and fired at 1050 °C for 4 h and then kept at 800 °C for 3 days. Then the sample is cooled to room temperature and sample is crushed and again filled into evacuated tube and homogenized at 350 °C for a week.

1.6.3. Synthesis of nanoparticles of Fe$_3$Se$_4$

Synthesis by thermal-decomposition:

In this method, hexagonal and monoclinic phases of iron selenide nanocrystals are synthesized via an injection method in a three-neck flask under argon atmosphere[52]. Firstly, Fe-oleylamine complex is prepared by dissolving iron precursor in oleylamine (OLA) at elevated temperatures (200 °C) and then cooled down to room temperature. Similarly, Se-powder is also dissolved in OLA at 330 °C under argon gas. Then, the Fe-OLA complex is injected into Se-solution and the resulting mix is subjected to heating and aging. The hexagonal sheets of iron selenide nanoparticles can be seen in figure 1.9.

Mousumi Sen
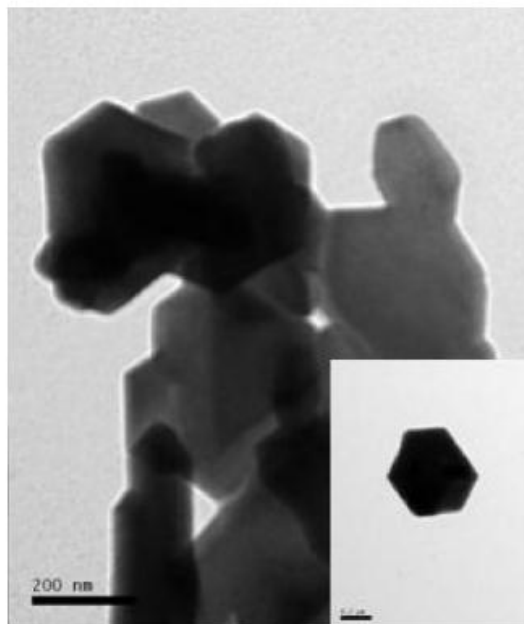
Figure 1.9: TEM image of Hexagonal-phase nanosheets of iron selenide prepared by thermal decomposition method. Inset: a single hexagonal nanosheet[52].

Synthesis by organic-solution-phase method

In the year 2011, Zhang *et al*[33] synthesized nanostructures of Fe_3Se_4 by a one-pot high-temperature organic-solution-phase method which became very popular for preparing Fe_3Se_4 nanoparticles in later years. In this method, all the precursors are mixed in an organic solvent in a four neck flask, and the heated under nitrogen flow.

As, Fe_3Se_4 is a naturally layered material having weak bonding in the plane ($\bar{1}01$), layered structures (nano-sheets or nano-platelet) tend to form in the initial stages of the reaction. By controlling the nucleation rate and different coordination ligands various different morphologies of Fe_3Se_4 nanostructures are obtained. Figure 1.10 displays different shapes of Fe_3Se_4 nanoparticles obtained by this method.

Mousumi Sen
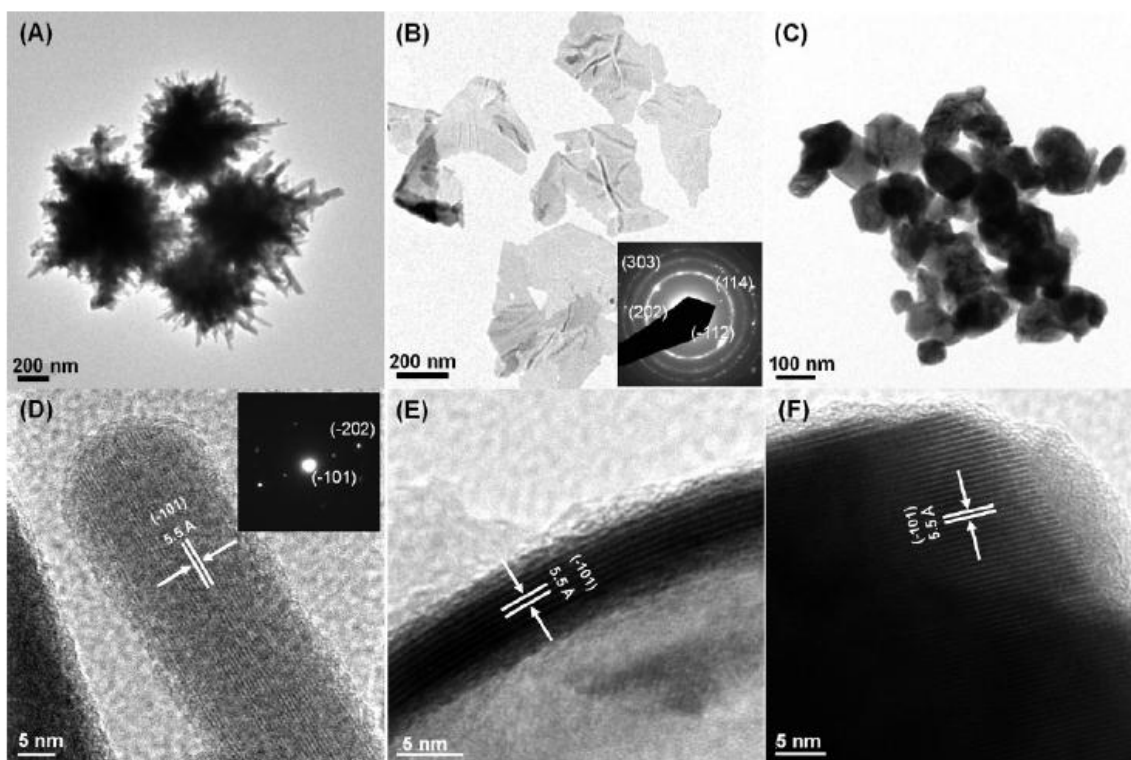
Figure1.10: Typical TEM images of (A) the as-synthesized Fe_3Se_4nanocacti with rod-like features growing on the surface, (B) several isolated Fe_3Se_4nanosheets, and (C) the as-synthesized Fe_3Se_4nanoplatelets.HRTEM images of (D) the rod-like features growing on the surface of Fe_3Se_4nanocacti, (E) the edge of a rolled-up Fe_3Se_4nanosheet revealing its thickness; and (F) the as-synthesized Fe_3Se_4nanoplatelets[33].

Synthesis by anodic aluminium oxide (AAO) porous membrane

Synthesis of one-dimensional nanowires of Fe_3Se_4 has been realized with the help of commercially available anodic aluminium oxide (AAO) templates. In the first step Fe nanowires are deposited in the template and in the second step the nanowires are selenized in presence of pure Se-powder at high temperature in an evacuated silica tube. Figure 1.11 shows the cross-sectional view of Fe_3Se_4 nanowires in the AAO template.
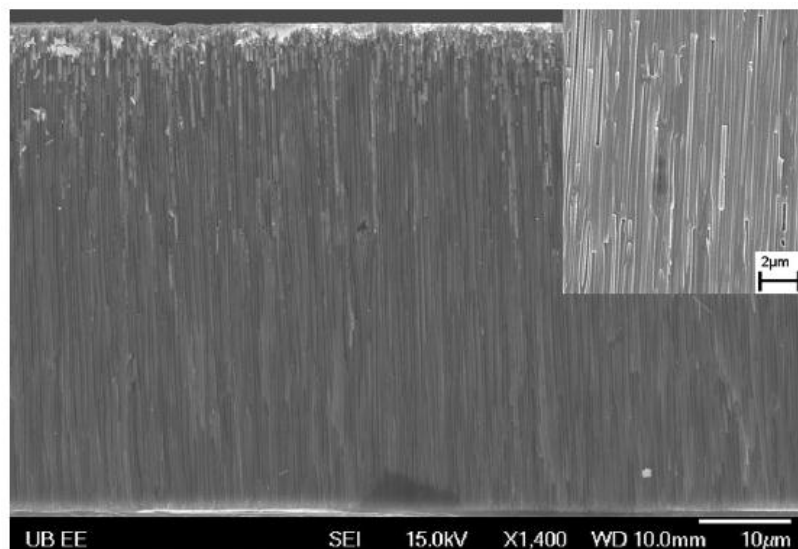
Figure 1.11: SEM image for the cross-sectional view of the Fe_3Se_4/AAO membranes. The inset exhibits a good filling of Fe_3Se_4 nanowires in the AAO membrane[57].

1.7. Magnetism in Fe_3Se_4

Before discussing the magnetism in Fe_3Se_4, it is necessary to gain understanding of some basic terms and phenomenon in magnetism.

1.7.1. Ferrimagnetism:

Ferrimagnetic substances exhibit significant spontaneous magnetism just like ferromagnetism. In 1948, L. Néel coined the term ferrimagnetism and gave theoretical understanding of ferrites (double oxides of iron and another metal), the most important ferrimagnetic materials[58]. In a ferrite crystal, the metal ions occupy two different crystallographic different positions (A-site and B-site). Néel assumed that the exchange interaction between ions at A and B-site is negative. Thus, the two sublattices are spontaneously magnetized in opposite directions. In ferrimagnets, the magnitude of

Mousumi Sen

magnetic moments in the two sub-lattices A and B are not equal. Therefore, the moments do not entirely cancel each other and a net spontaneous magnetization results (figure 1.12). Ferrimagnetic materials consist of magnetic domains and exhibit all the hallmarks of ferrimagnets, like Curie temperature, hysteresis, remanence etc.

However, the response of a ferrimagnet is quite different from a ferromagnet at a very high magnetic field[40]. Above a certain critical magnetic field, the spin orientation changes from antiparallel to a canted arrangement resulting in sudden increase in magnetization, known as spin flopping.
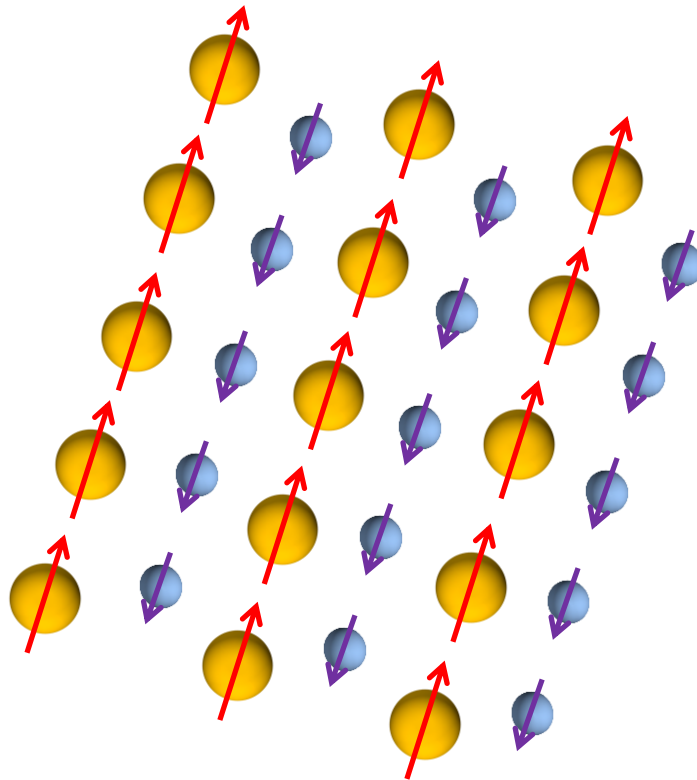
Figure1.12: In ferrimagnets, the magnetic structure is composed of two magnetic sublattices (yellow and blue). The magnetic moments (symbolized by length of the arrow here) of two sublattices are not equal and result in a net magnetic moment.

1.7.2. Magnetocrystalline anisotropy

Magnetocrystalline anisotropy is an intrinsic property of the crystal. A material is said to possess magnetocrystalline anisotropy if it has taken more energy to magnetize along one direction than others. The time reversal symmetry requires that a state with a certain magnetization distribution M(r) should have the same energy as the state with reversed magnetization along the same axis, $-M(r)$[59]. This tendency gives rise to anisotropic energy which can be written as follows (for materials exhibiting uniaxial anisotropy neglecting the higher order terms).

$$E_a = K_u \sin^2\theta$$

Where, K_u is the anisotropy constant and θ is the angle between the easy-axis and the magnetization vector (figure 1.13).
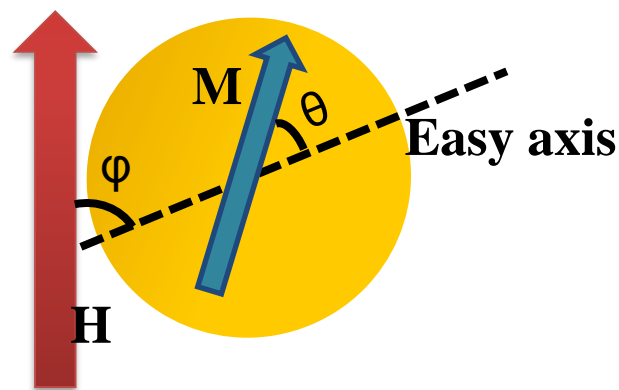
Figure 1.13: Directions of easy-axis, magnetization and external field in case of single domain particle with uniaxial anisotropy are shown for representative purpose.

Mousumi Sen

The strength of anisotropy in a material is determined by the magnitude of anisotropy constant. From the above expression it is clear that there are two local energy minima corresponding to $\theta = 0$ and π, separated by an energy barrier E_B[60].
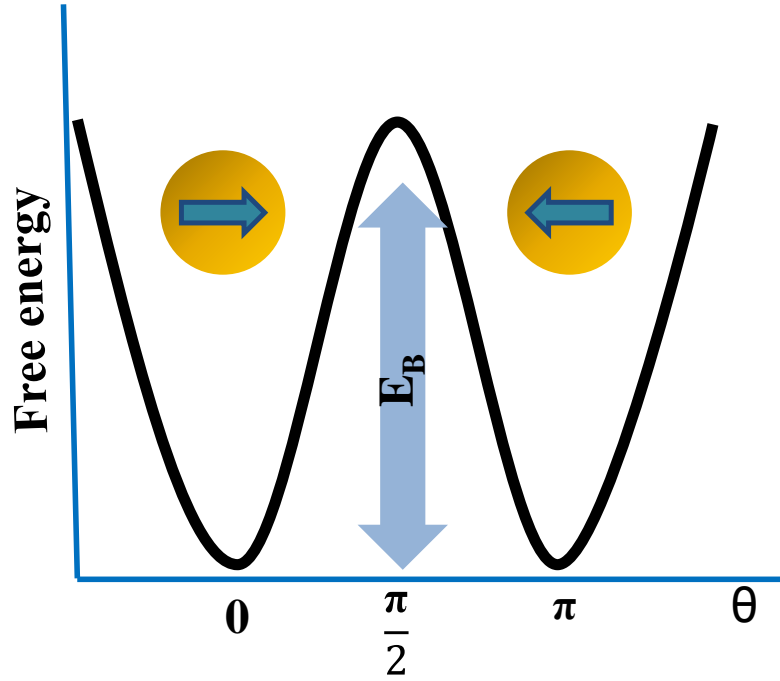
Figure 1.14: Schematic picture of the free energy of a single-domain particle with uniaxial anisotropy as a function of magnetization direction.

The physical origin of crystalline anisotropy lies in spin-orbit coupling[61]. The spin and the orbital motion of each electron are coupled. When an external field tries to reorient a spin the orbit of that electron also tries to orient, but, the orbit being strongly coupled to the lattice resists the orientation of spin. Anisotropy sets an upper limit on the coercivity of the materials as can be seen from the below expression.

$$H_c < \frac{2\,K_u}{\mu_0 M_s}$$

Mousumi Sen

1.7.3. Stoner-Wohlfarth model (SW model)

The Stoner–Wohlfarth model was developed by Edmund Clifton Stoner and Erich Peter Wohlfarth in 1948 for explaining the hysteresis in ferromagnets[62]. The particles were considered to be noninteracting single domain ellipsoidal particles with uniaxial anisotropy such that the magnetization (both magnitude and direction) doesn't vary inside the particle.

This model explains the coherent reversal of magnetization in single domain particles and the shape of the hysteresis loops were calculated for different angle between the easy-axis of the particle and applied magnetic field (φ in figure 1.13). When the external field is applied at an angle φ to the easy-axis, then the magnetization lies at an angle θ with the easy-axis. The free energy density of the system can be written as below[60].

$$E = K sin^2\theta - \mu_0 H M_S \cos(\emptyset - \theta)$$

Solving this equation by energy minimization it was found that the hysteresis loop is rectangular with coercivity $2K/M_S$ when the external field is either parallel ($\varphi=0$) or anti-parallel ($\varphi=180$) to the easy-axis. When the field is perpendicular to the easy-axis, then no hysteresis is found in the SW model.

1.7.4. Maximum energy product

Maximum energy product is the figure of merit for expressing the quality of a permanent magnet. It is defined as the maximum area of the rectangle under the B-H curve in the second quadrant of the hysteresis loop (see figure 1.15). It is a measure of the magnetic energy stored in the material. For the current permanent magnetic materials the energy product varies from few MGOe to up to 50 MGOe for rare earth based magnets[61].

Mousumi Sen
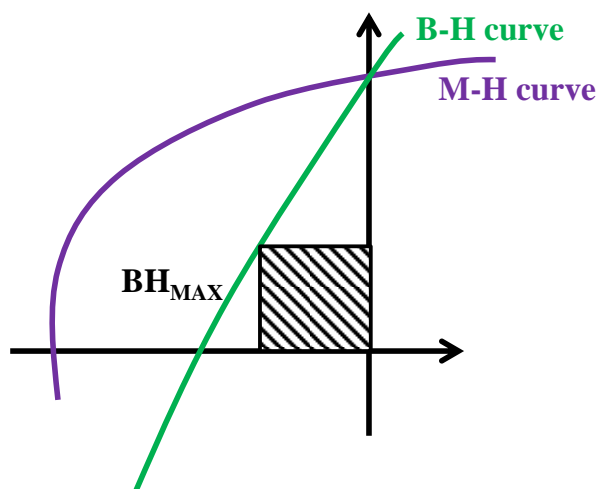
Figure 1.15: Calculation of maximum energy product is done on the second quadrant of the B-H hysteresis loop. The area of the shaded region gives the maximum energy product value for the material.

The single crystals of Fe_3Se_4 show that the easy-axis of magnetization in these samples is c-plane. The sample does not saturate even at 11000 Oe external magnetic field[56]. Fe_3Se_4 is a ferrimagnet similar to its sulphur counterpart Fe_3S_4[63] with Curie temperature ~ 315 K. Fe_3Se_4 does not show rotation of its easy-axis with temperature unlike Fe_7Se_8. Although this compound is known to be ferrimagnetic for more than half a century, the recent thrust originated after discovery of semi-hard magnetic properties at room temperature in Fe_3Se_4. The most unique property of Fe_3Se_4 is the giant coercivity it displays (~4 kOe at room temperature) upon reducing its size to nano-dimension[33]. It has a large uniaxial anisotropy constant ~ 10^7 erg/cm^3. The most alluring behavior of this compound is the appearance of giant coercivity (~ 40 KOe) at 10 K (figure 1.16). The coercivity increases almost 10 fold from its room temperature value and saturation magnetization also increases from (~ 5 emu/g) to (~ 15 emu/g). The hysteresis loop is almost squarish at low

Mousumi Sen

temperature. It is very rare for compounds without any rare earth metal ions or noble metal ions to have such large values anisotropy constants.
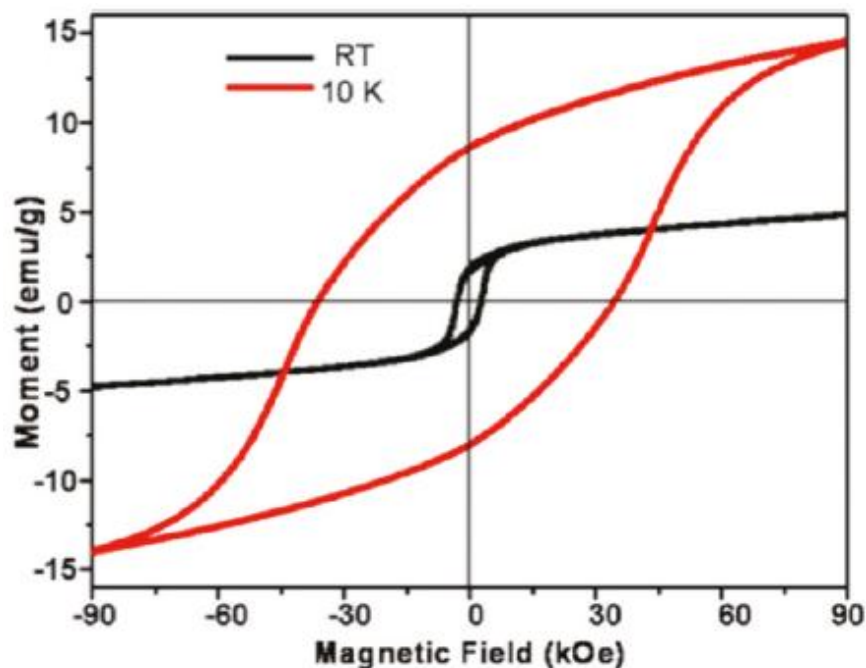
Figure 1.16: Hysteresis loops of (A) Fe_3Se_4nanocacti measured by the vibrating sample magnetometer option of a PPMS with a field of 90 kOe at 10 K (red curves) and at room temperature (black curves). The 10 K hysteresis loops were measured after zero-field cooling.[33]

1.7.5. Magnetic properties of Fe_3Se_4 nanoparticles

Gen *et al.* studied the coercivity and anisotropy in Fe_3Se_4 nanostructures in year 2011[64]. The origin of this giant coercivity at low temperature is probed both by experiments and first principles calculations. The large value of anisotropy constant (1.1×10^7 erg/cm^3) at 10 K arising from ordered cation vacancy is the reason for a large coercivity value. By

Mousumi Sen

aligning the powder sample in an external magnetic field the anisotropy constant (K_u) can be determined by extrapolating the hysteresis loops in easy and hard directions.

Anisotropy constant can also be estimated by law of approach to saturation from the hysteresis loop of the material by fitting the magnetization at high field values according to b equation given below[65]

$$M = M_S + A \left(coth \frac{\mu H}{K_B T} - \frac{K_B T}{\mu H} \right)$$

where M_s is the saturation magnetization and M is the total magnetization of an ultrafine particle. Also, experimental magnetic hysteresis loop of Fe_3Se_4 nanoparticles obtained at 10 K is in good agreement with the Stoner and Wohlfarth theoretical curve calculated for a noninteracting randomly oriented uniaxial single-domain particle system. In both the above mentioned work, it is found that anisotropy constant K_u is proportional to the cube of the saturation magnetization $_{Ms}$, which indicates the presence of uniaxial magnetocrystalline anisotropy in this compound.

The critical size for the single domain size of Fe_3Se_4 can be estimated by the below mentioned expression[58]

$$r_C \approx 9 \frac{(AK_u)^{1/2}}{\pi M_S{}^2}$$

where, A is the exchange stiffness constant. When calculated, the single domain size of Fe_3Se_4 comes to about 2000 nm[64]. Therefore, the nanoparticles discussed here in this thesis can be considered single domain particles. The mechanism of magnetization reversal is incoherent rotation of spins in this compound.

Mousumi Sen

1.7.6. Magnetoresistance (MR) in Fe$_3$Se$_4$

Magnetoresistance is a phenomenon where the electrical resistance of the material tends to change as a function of external applied magnetic field. The 1-dimentional nanowire arrays show positive magnetoresistance[57]. Below 100 K, the Fe$_3$Se$_4$ nanowires exhibit positive MR, which is highly field and temperature dependent. Above 100 K, MR becomes vanishingly small. The positive MR is found to be symmetric around the zero field (figure 1.17). The MR properties of the Fe$_3$Se$_4$ nanowire arrays are well explained by the effect of the magnetic field on the VRH (variable range hopping) conduction process
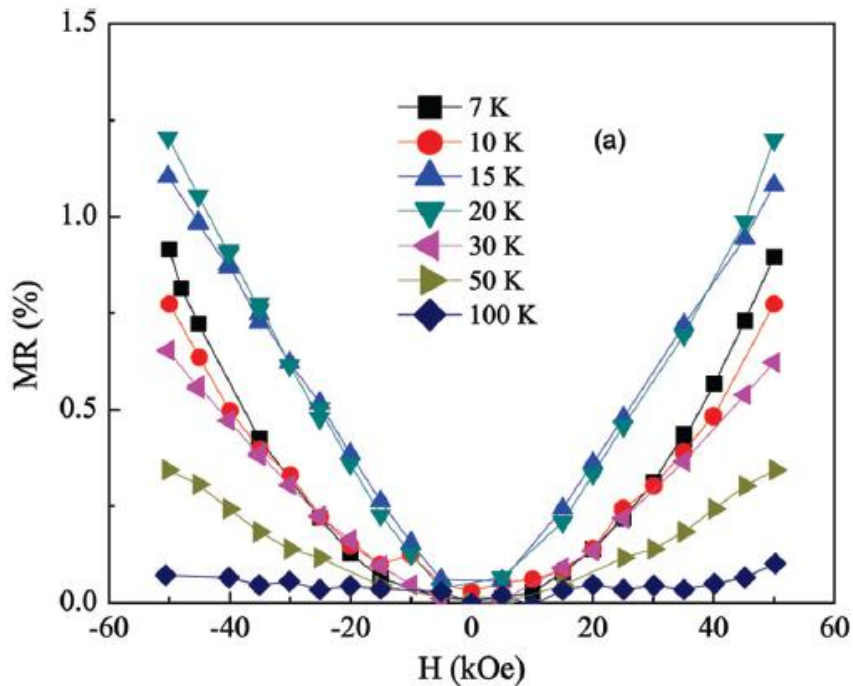
in this work.

Figure 1.17: Positive magnetoresistance of the Fe$_3$Se$_4$ nanowire arrays at different temperatures[57].

Mousumi Sen

1.7.7. Effect of doping metal site on magnetic properties of Fe_3Se_4

According to the phase diagram[66], the systems $Fe_{3-x}M_xSe_4$ can form solid solutions with structure Cr_3S_4 over a whole composition. In fact, replacing some of the Fe-atoms are by other metal atoms cast huge differences to the properties of this material. The efforts are mostly dedicated in the direction of improving the magnetic property of the material.

In single crystals, it was seen that substitution Ni and Co atoms in place of Fe, dilutes the ferrimagnetism of Fe_3Se_4 and the substituted atoms do not show localized moments[67,68].

Co-doped Fe_3Se_4 nanostructures $Co_xFe_{3-x}Se_4$, (with x ranging from 0 to 1) showed that the doped structures are also monoclinic. The saturation magnetization, coercivity and Curie temperature decrease with increasing Co concentration. The coercivity of the nanoparticles at 10 K is reduced to 37 kOe for x = 0.2 and further decreases to 9 kOe for x = 1[33]. The Curie temperature is also reduced to less than 200 K for x = 1 so the samples behave paramagnetically at room temperature.

However, when some Fe-atoms are replaced with Cr-atoms improvements over Curie temperature. For $FeCr_2Se_4$ samples the Curie temperature was reported 429 K. The Cr-substitution reportedly enhances the anisotropy constant and coercivity[69]. However, with increasing Cr concentration the saturation magnetization decreases monotonically. This can be contributed to weaker localized magnetic moments of Cr cations than Fe cations.

In the next chapter, two different approaches have been discussed for improving the magnetic properties of pure Fe_3Se_4.

Mousumi Sen

1.8: Study of electric properties in iron selenide

In the year 1973, the electric conductivity was studied in Fe_7Se_8, Fe_3Se_4 and $NiFe_2Se_4$ single crystals, results of which are presented below (figure 1.18). In Fe_3Se_4, up-to 330 K (the ferrimagnetic to paramagnetic transition temperature, T_c) the interatomic spacing is such that the cation-cation overlap takes place leading to formation of bands resulting in metallic conduction[70]. The study on single crystals shows that Fe_3Se_4 and Fe_7Se_8 has negative temperature coefficient of electric conductivity up to temperature 330 K. Above this temperature there is an increase in electric conductivity with increase in temperature (semiconductor type behavior). Below 330 K, the Fe-Fe interatomic spacing are such that, the cation-cation overlapping takes place leading to formation of bands which brings out metallic nature of conductivity in Fe_3Se_4.
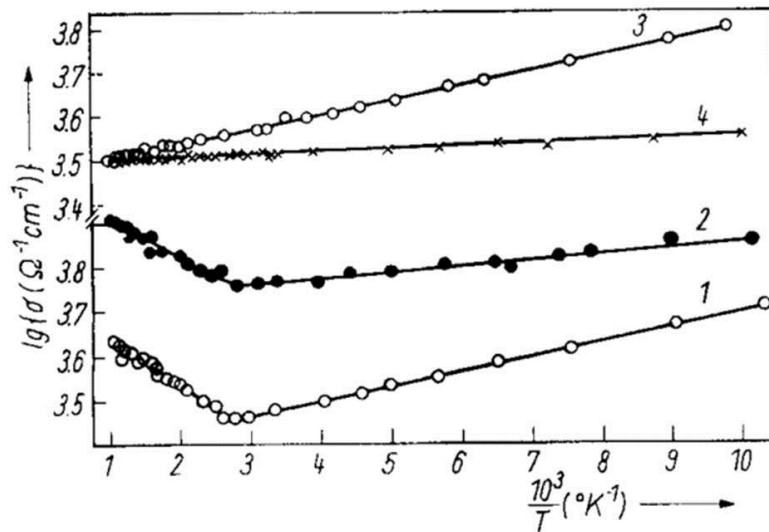
Figure 1.18: Temperature dependence of electric conductivity for 1) Fe_3Se_4 and 2) Fe_7Se_8 3) $NiFe_2Se_4$ ($\vec{E} \perp$ (ab)), 4) $NiFe_2Se_4$ ($\vec{E} \parallel$ (ab))

Mousumi Sen

Fe_3Se_4 can therefore also be called as semi-metal similar to its sulphur counterpart Fe_3S_4[71].A semi-metal is a material that has a very small overlap between bottom of the conduction band and top of the valence band at Fermi level ε_F. Therefore, semi-metals do not have band gap and negligible density of states at the Fermi level. At T_c, at least one electron is transferred to the conduction band[72]. The overlapping of cations disappears partially or completely and material exhibits semiconducting nature of conductivity (electrical conductivity increases with temperature).This may be due to thermal expansion of the material or the magnetic transformation. The electric property of the material depends hugely on the microstructure. We will discuss more about these properties in chapter 4.
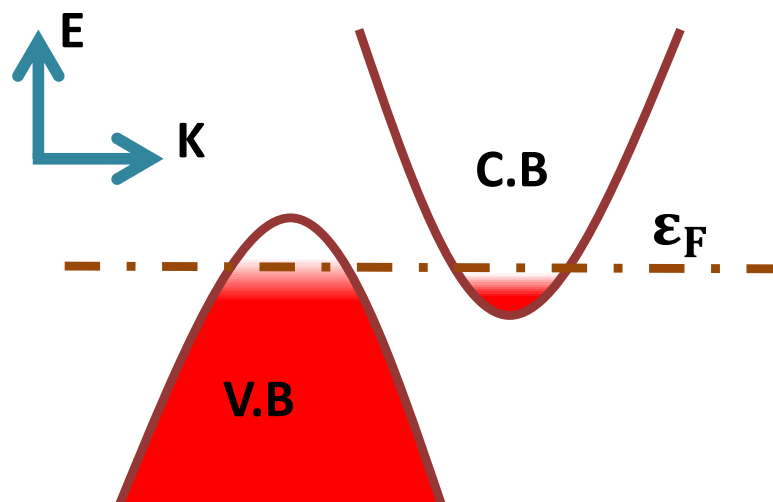
Figure 1.19: Schematic of energy band diagram of semi-metal.

Mousumi Sen

1.9: Study of thermal properties in iron selenide:

Heat capacity values of iron selenide phases were measured from temperature 3K to 350

K by Gronvold and Westrum in 1959 on polycrystalline powder samples prepared by

elemental synthesis at elevated temperature[73].
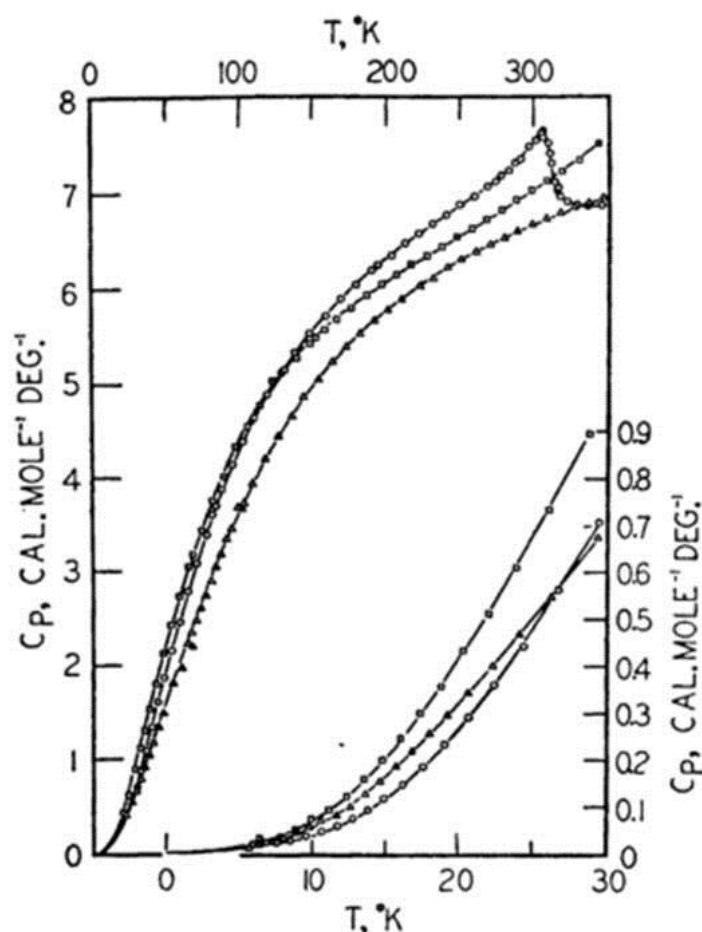
Figure 1.20: Heat capacities of iron selenides on a gram formula weight basis. Ref [66]

A λ-transition was observed around 307 K in the temperature dependent heat capacity

measurement of Fe_3Se_4. The increase in entropy associated with this transition is about 2

cal $mol^{-1}deg^{-1}$. The transition temperature coincides with the change from paramagnetic to

ferrimagnetic state in Fe_3Se_4. However, there are no reports of heat capacity of Fe_3Se_4 in

nano-dimensions. In chapter 3, the thermal properties of Fe_3Se_4 nanoparticles are

discussed in details.

Mousumi Sen

1.10: Scope of present investigation:

In this section, an introduction to various aspects of research done on iron selenide in this thesis is presented.
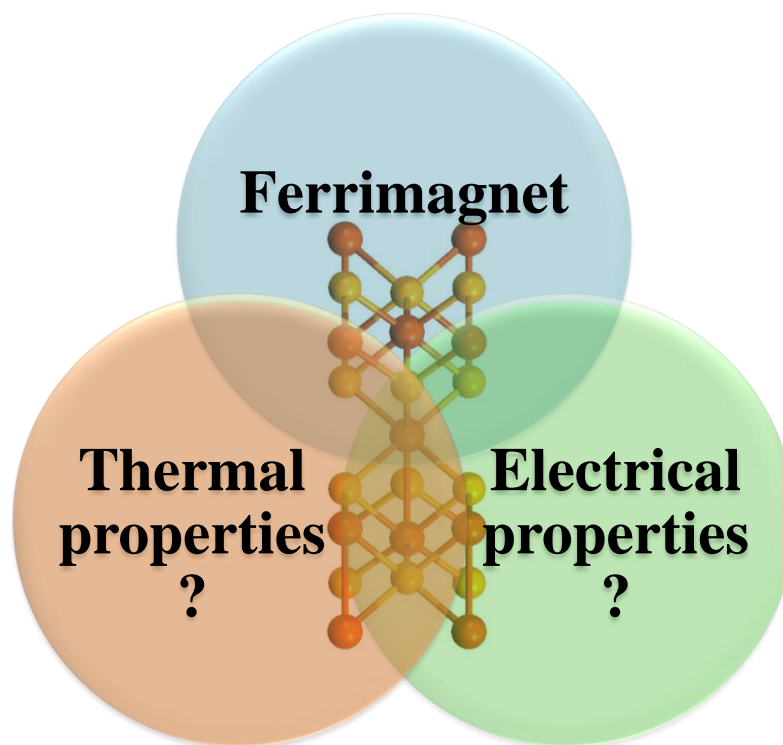
Figure 1.21: Scope of the present investigation, the magnetic, thermal, and electrical properties of Fe_3Se_4 and their interactions.

Due to the ever increasing price of rare earth materials, health hazards and environmental damage, the world was looking towards rare-earth free alternatives for permanent magnets applications. After the discovery of giant coercivity in the monoclinic iron selenide phase[33], Fe_3Se_4 nanoparticles caught the attention of researchers for its semi-hard magnetic properties. As discussed in the previous section, the research was focused primarily on improving the magnetic properties to achieve more permanent magnet like characteristics.

Mousumi Sen

Fe_3Se_4 holds copious potential for many applications in energy conversion and storage including high density data storage and permanent magnets. Serious efforts are required in order to improve the material property and designing of the composite materials. In order to use this material in real life applications, it is very important to study the physical properties of this material, for e.g. thermal properties and electric properties. These properties in Fe_3Se_4 are under-estimated and literature reports are rare. In this thesis, efforts are dedicated to understand the physical properties and their interplay in Fe_3Se_4, and how are they important for fundamental understanding and technical applications.

Thesis Outline:

In the first chapter, the transition metal chalcogenides are introduced and their applications in various fields are discussed. It is highlighted in the chapter as why Fe_3Se_4 is fundamentally and technologically an important compound to study. Brief literature review of $Fe_3Se_4$is given and scope of the thesis is discussed.

The second chapter consists of two main sections with the objective of improving the energy product by modification of Fe_3Se_4. In the first section, the effect of manganese ion doping on the magnetic properties are studied in detail. Various samples with different manganese concentration were prepared and the optimum doping concentration was found for which the energy product was maximum without changing the Curie temperature. In the second section, a nanocomposite was made from Fe_3Se_4 and Fe_3O_4 nanoparticles forming a hard: soft exchange spring magnet. A single-phase behavior is obtained in magnetism although two crystallographically different phases were present in the composite.

The third chapter deals with the change in magnetic entropy and specific heat capacity in Fe_3Se_4 nanoparticles were studied in a broad temperature (215-340 K) and magnetic field

range (0-60 k Oe). The isothermal magnetic entropy change (ΔS_M) is estimated by an indirect method from the isothermal magnetization curves measured in this temperature range. The ΔS_M was obtained - 46×10^{-2} J/kg.K at ~317 K when the field was changed from 0 to 60 kOe. The nature of this transition was analyzed by universal curve behavior. The temperature and magnetic field dependence of specific heat capacity was studied and analyzed to estimate the adiabatic temperature change (ΔTad).

In the fourth chapter, a very important discovery is discussed. For the first time, spontaneous and reversible polarization in Fe_3Se_4 is observed. Experimental evidences of the coexistence of magnetic and ferroelectric ordering and magneto-electric coupling at room temperature in Fe_3Se_4nanorods are discussed. We observed that the ferroelectric and magnetic Curie temperature coincide and shows a coupling manifested by an anomaly in the dielectric constant and Raman shift at T_c. We do not completely understand the origin of the ferroelectric ordering at this point however the simultaneous presence of magnetic and ferroelectric ordering at room temperature in Fe_3Se_4 along with hard magnetic properties will open new research areas for devices.

The conclusion of this thesis and scope of future works are discussed in fifth chapter.

Mousumi Sen

References:

(1) Gao, M.-R.; Xu, Y.-F.; Jiang, J.; Yu, S.-H. Nanostructured Metal Chalcogenides: Synthesis, Modification, and Applications in Energy Conversion and Storage Devices. *Chem. Soc. Rev.* **2013**, *42* (7), 2986.

(2) Gao, M.-R.; Jiang, J.; Yu, S.-H. Solution-Based Synthesis and Design of Late Transition Metal Chalcogenide Materials for Oxygen Reduction Reaction (ORR). *Small* **2012**, *8* (1), 13–27.

(3) Puthussery, J.; Seefeld, S.; Berry, N.; Gibbs, M.; Law, M. Colloidal Iron Pyrite (FeS 2) Nanocrystal Inks for Thin-Film Photovoltaics. *J. Am. Chem. Soc.* **2011**, *133* (4), 716–719.

(4) Lai, C.-H.; Huang, K.-W.; Cheng, J.-H.; Lee, C.-Y.; Hwang, B.-J.; Chen, L.-J. Direct Growth of High-Rate Capability and High Capacity Copper Sulfide Nanowire Array Cathodes for Lithium-Ion Batteries. *J. Mater. Chem.* **2010**, *20* (32), 6638.

(5) Zhu, L.; Richardson, B.; Tanumihardja, J.; Yu, Q. Controlling Morphology and Phase of Pyrite FeS2 Hierarchical Particles via the Combination of Structure-Direction and Chelating Agents. *Crystengcomm* **2012**, *14* (12), 4188–4195.

(6) Arachchige, I. U.; Brock, S. L. Sol-Gel Methods for the Assembly of Metal Chalcogenide Quantum Dots. *Acc. Chem. Res.* **2007**, *40* (9), 801–809.

(7) Shirasaki, Y.; Supran, G. J.; Bawendi, M. G.; Bulović, V. Emergence of Colloidal Quantum-Dot Light-Emitting Technologies. *Nat. Photonics* **2013**, *7* (12), 933–933.

(8) Kershaw, S. V; Susha, A. S.; Rogach, A. L. Narrow Bandgap Colloidal Metal Chalcogenide Quantum Dots: Synthetic Methods, Heterostructures, Assemblies, Electronic and Infrared Optical Properties. *Chem. Soc. Rev.* **2013**, *42* (7), 3033–3087.

(9) Lai, C.-H.; Huang, K.-W.; Cheng, J.-H.; Lee, C.-Y.; Lee, W.-F.; Huang, C.-T.; Hwang, B.-J.; Chen, L.-J. Oriented Growth of Large-Scale Nickel Sulfide Nanowire Arrays via a General Solution Route for Lithium-Ion Battery Cathode Applications. *J. Mater. Chem.* **2009**, *19* (39), 7277.

Mousumi Sen

(10) Gao, M.-R.; Gao, Q.; Jiang, J.; Cui, C.-H.; Yao, W.-T.; Yu, S.-H. A Methanol-Tolerant Pt/CoSe2 Nanobelt Cathode Catalyst for Direct Methanol Fuel Cells. *Angew. Chemie Int. Ed.* **2011**, *50* (21), 4905–4908.

(11) Gao, M.-R.; Liu, S.; Jiang, J.; Cui, C.-H.; Yao, W.-T.; Yu, S.-H. In Situ Controllable Synthesis of Magnetite nanocrystals/CoSe2 Hybrid Nanobelts and Their Enhanced Catalytic Performance. *J. Mater. Chem.* **2010**, *20* (42), 9355.

(12) Chhowalla, M.; Shin, H. S.; Eda, G.; Li, L.-J.; Loh, K. P.; Zhang, H. The Chemistry of Two-Dimensional Layered Transition Metal Dichalcogenide Nanosheets. *Nat. Chem.* **2013**, *5* (4), 263–275.

(13) Heine, T. Transition Metal Chalcogenides: Ultrathin Inorganic Materials with Tunable Electronic Properties. *Acc. Chem. Res.* **2015**, *48* (1), 65–72.

(14) Vogel, E. M.; Robinson, J. a. Two-Dimensional Layered Transition-Metal Dichalcogenides for Versatile Properties and Applications. *MRS Bull.* **2015**, *40* (7), 558–563.

(15) Yuan, H.; Liu, Z.; Xu, G.; Zhou, B.; Wu, S.; Dumcenco, D.; Yan, K.; Zhang, Y.; Mo, S.-K.; Dudin, P.; et al. Evolution of the Valley Position in Bulk Transition-Metal Chalcogenides and Their Monolayer Limit. *Nano Lett.* **2016**, *16* (8), 4738–4745.

(16) Yeh, P.; Jin, W.; Zaki, N.; Zhang, D.; Liou, J. T.; Sadowski, J. T.; Al-Mahboob, A.; Dadap, J. I.; Herman, I. P.; Sutter, P.; et al. Layer-Dependent Electronic Structure of an Atomically Heavy Two-Dimensional Dichalcogenide. *Phys. Rev. B* **2015**, *91* (4), 41407.

(17) Ross, J. S.; Wu, S.; Yu, H.; Ghimire, N. J.; Jones, A. M.; Aivazian, G.; Yan, J.; Mandrus, D. G.; Xiao, D.; Yao, W.; et al. Electrical Control of Neutral and Charged Excitons in a Monolayer Semiconductor. *Nat. Commun.* **2013**, *4*, 1474.

(18) Feng, J.; Sun, X.; Wu, C.; Peng, L.; Lin, C.; Hu, S.; Yang, J. Metallic Few-Layered VS 2 Ultrathin Nanosheets : High Two-Dimensional Conductivity for In-Plane Supercapacitors. **2011**, 17832–17838.

(19) Chang, K.; Chen, W. In Situ Synthesis of MoS2/graphene Nanosheet Composites

Mousumi Sen

with Extraordinarily High Electrochemical Performance for Lithium Ion Batteries. *Chem. Commun. (Camb).* **2011**, *47* (14), 4252–4254.

(20) Liufu, S.-C.; Chen, L.-D.; Yao, Q.; Wang, C.-F. Assembly of One-Dimensional Nanorods into Bi2S3 Films with Enhanced Thermoelectric Transport Properties. *Appl. Phys. Lett.* **2007**, *90* (11), 112106.

(21) Kadel, K.; Kumari, L.; Li, W. Z.; Huang, J. Y.; Provencio, P. P. Synthesis and Thermoelectric Properties of Bi2Se3 Nanostructures. *Nanoscale Res. Lett.* **2010**, 1–7.

(22) Mehta, R. J.; Karthik, C.; Jiang, W.; Singh, B.; Shi, Y.; Siegel, R. W.; Borca-Tasciuc, T.; Ramanath, G. High Electrical Conductivity Antimony Selenide Nanocrystals and Assemblies. *Nano Lett.* **2010**, *10* (11), 4417–4422.

(23) Malakooti, R.; Cademartiri, L.; Migliori, A.; Ozin, G. a. Ultrathin Sb 2 S 3 Nanowires and Nanoplatelets. *J. Mater. Chem.* **2008**, *18* (1), 66–69.

(24) Dresselhaus, M. S.; Chen, G.; Tang, M. Y.; Yang, R. G.; Lee, H.; Wang, D. Z.; Ren, Z. F.; Fleurial, J.-P.; Gogna, P. New Directions for Low-Dimensional Thermoelectric Materials. *Adv. Mater.* **2007**, *19* (8), 1043–1053.

(25) Minnich, a J.; Dresselhaus, M. S.; Ren, Z. F.; Chen, G. Bulk Nanostructured Thermoelectric Materials: Current Research and Future Prospects. *Energy Environ. Sci.* **2009**, *2* (5), 466.

(26) Xia, Y.; Qian, D.; Hsieh, D.; Wray, L.; Pal, A.; Lin, H.; Bansil, A.; Grauer, D.; Hor, Y. S.; Cava, R. J.; et al. Observation of a Large-Gap Topological-Insulator Class with a Single Dirac Cone on the Surface. *Nat. Phys.* **2009**, *5* (6), 18.

(27) Zhang, J.; Peng, Z.; Soni, A.; Zhao, Y.; Xiong, Y.; Peng, B.; Wang, J.; Dresselhaus, M. S.; Xiong, Q. Raman Spectroscopy of Few-Quintuple Layer Topological Insulator Bi 2 Se 3 Nanoplatelets. *Nano Lett.* **2011**, *11* (6), 2407–2414.

(28) Cha, J. J.; Williams, J. R.; Kong, D.; Meister, S.; Peng, H.; Bestwick, A. J.; Gallagher, P.; Goldhaber-Gordon, D.; Cui, Y. Magnetic Doping and Kondo Effect in Bi 2 Se 3 Nanoribbons. *Nano Lett.* **2010**, *10* (3), 1076–1081.

Mousumi Sen

(29)   Hsu, F.-C.; Luo, J.-Y.; Yeh, K.-W.; Chen, T.-K.; Huang, T.-W.; Wu, P. M.; Lee, Y.-C.; Huang, Y.-L.; Chu, Y.-Y.; Yan, D.-C.; et al. Superconductivity in the PbO-Type Structure -FeSe. *Proc. Natl. Acad. Sci.* **2008**, *105* (38), 14262–14264.

(30)   Mizuguchi, Y.; Tomioka, F.; Tsuda, S.; Yamaguchi, T.; Takano, Y. Superconductivity at 27 K in Tetragonal FeSe under High Pressure. *Appl. Phys. Lett.* **2008**, *93* (15), 152505.

(31)   Schuster, W.; Mikler, H.; Komarek, K. L. Transition Metal-Chalcogen Systems, VII.: The Iron-Selenium Phase Diagram. *Monatshefte fur Chemie* **1979**, *110* (5), 1153–1170.

(32)   Xu, J.; Jang, K.; Lee, J.; Kim, H. J.; Jeong, J.; Park, J. G.; Son, S. U. Phase-Selective Growth of Assembled FeSe2 Nanorods from Organometallic Polymers and Their Surface Magnetism. *Cryst. Growth Des.* **2011**, *11* (7), 2707–2710.

(33)   Zhang, H.; Long, G.; Li, D.; Sabirianov, R.; Zeng, H. Fe 3 Se 4 Nanostructures with Giant Coercivity Synthesized by Solution Chemistry. *Chem. Mater.* **2011**, *23* (16), 3769–3774.

(34)   Dong, S.; Liu, J.-M. M.; Dagotto, E. BaFe2Se3: A High TC Magnetic Multiferroic with Large Ferrielectric Polarization. *Phys. Rev. Lett.* **2014**, *113* (18), 187204.

(35)   Hemberger, J.; Lunkenheimer, P.; Fichtl, R.; Weber, S.; Tsurkan, V.; Loidl, A. Multiferroic Behavior in. *Phys. B Condens. Matter* **2006**, *378–380*, 363–366.

(36)   Hemberger, J.; Lunkenheimer, P.; Fichtl, R.; Krug von Nidda, H. -a.; Tsurkan, V.; Loidl, A. Relaxor Ferroelectricity and Colossal Magnetocapacitive Coupling in Ferromagnetic CdCr2S4. *Nature* **2005**, *434* (7031), 364–367.

(37)   Li, Z.; Hu, Y.; Howard, K. A.; Jiang, T.; Fan, X.; Miao, Z.; Sun, Y.; Besenbacher, F.; Yu, M. Multifunctional Bismuth Selenide Nanocomposites for Antitumor Thermo-Chemotherapy and Imaging. *ACS Nano* **2016**, *10* (1), 984–997.

(38)   Yang, K.; Yang, G.; Chen, L.; Cheng, L.; Wang, L.; Ge, C.; Liu, Z. FeS Nanoplates as a Multifunctional Nano-Theranostic for Magnetic Resonance Imaging Guided Photothermal Therapy. *Biomaterials* **2015**, *38*, 1–9.

Mousumi Sen

(39)   Song, X.-R.; Wang, X.; Yu, S.-X.; Cao, J.; Li, S.-H.; Li, J.; Liu, G.; Yang, H.-H.; Chen, X. Co 9 Se 8 Nanoplates as a New Theranostic Platform for Photoacoustic/Magnetic Resonance Dual-Modal-Imaging-Guided Chemo-Photothermal Combination Therapy. *Adv. Mater.* **2015**, *27* (21), 3285–3291.

(40)   CHIKAZUMI, S. *Physics of Ferromagnetism*; Oxford University Press, 1996.

(41)   Beal, J. H. L.; Prabakar, S.; Gaston, N.; The, G. B.; Etchegoin, P. G.; Williams, G.; Tilley, R. D. Synthesis and Comparison of the Magnetic Properties of Iron Sulfide Spinel and Iron Oxide Spinel Nanocrystals. *Chem. Mater.* **2011**, *23* (10), 2514–2517.

(42)   Svendsen, S. R.; Åkesson, G.; Krogh-Moe, J.; Songstad, J.; Pilotti, Å. Decomposition Pressures and Standard Enthalpy of Formation for the Iron Selenides FeSe, Fe7Se8, Fe3Se4 and FeSe2. *Acta Chem. Scand.* **1972**, *26*, 3757–3774.

(43)   Yuan, B.; Luan, W.; Tu, S. One-Step Synthesis of Cubic FeS2 and Flower-like FeSe2 Particles by a Solvothermal Reduction Process. *Dalt. Trans.* **2012**, *41* (3), 772.

(44)   Qin, Z.; Yang, B. C.; Zhang, S. R.; Li, K.; Yan, S. Q.; Lv, X. W.; Li, Z. J. Flower-like Pyrite FeSe2 Nanoparticles with Enhanced Optical Properties by Hot-Injection. *Vacuum* **2015**, *111*, 157–159.

(45)   Wei, C.; Bai, Y.; Deng, A.; Bao, Y. Universal Synthesis of Air Stable, Phase Pure, Controllable FeSe 2 Nanocrystals. *Nanotechnology* **2016**, *27* (16), 165702.

(46)   Li, J.; Jin, Z.; Liu, T.; Wang, J.; Zheng, X.; Lai, J. Chemical Synthesis of MSe 2 (M = Ni, Fe) Particles by Triethylene Glycol Solution Process. *CrystEngComm* **2014**, *16* (30), 6819.

(47)   Hirone, T.; Maeda, S.; Tsuya, N. On the Ferrimagnetism of Iron Selenides. *J. Phys. Soc. Japan* **1954**, *9* (4), 496–499.

(48)   Hirone, T.; Chiba, S. The Magnetic Properties of FeSe X with the NiAs Structure. *J. Phys. Soc. Japan* **1956**, *11* (6), 666–670.

Mousumi Sen

(49)   Okazaki, A.; Hirakawa, K. Structural Study of Iron Selenides FeSe X . I Ordered Arrangement of Defects of Fe Atoms. *J. Phys. Soc. Japan* **1956**, *11* (9), 930–936.

(50)   Andresen, A. F.; Vestersjø, E.; Haaland, A.; Gronowitz, S.; Christiansen, H.; Rosén, U. A Neutron Diffraction Investigation of Fe3Se4. *Acta Chem. Scand.* **1968**, *22*, 827–835.

(51)   Andresen, a. F.; van Laar, B.; Kvamme, E.; Ohlson, R.; Shimizu, A. The Magnetic Structure of Fe3Se4. *Acta Chem. Scand.* **1970**, *24*, 2435–2439.

(52)   Lin, C.-R. L. C.-R.; Siao, Y.-J. S. Y.-J.; Lu, S.-Z. L. S.-Z.; Gau, C. G. C. Magnetic Properties of Iron Selenide Nanocrystals Synthesized <newline/>by the Thermal Decomposition. *IEEE Trans. Magn.* **2009**, *45* (10), 4275–4278.

(53)   Francis, L. *Crystallography and Crystal Chemistry of Materials with Layered Structures*; D.Reidel Publishing company: Holland, 2012.

(54)   Wold, A.; Kirby, D. *Solid State Chemistry: Synthesis, Structure, and Properties of Selected Oxides and Sulfides*; Chapman and Hall: New York, 1993.

(55)   BABOT, D.; BÉRODIAS, G.; LAMBERT-ANDRON, B. STRUCTURES MAGNÉTIQUES DE MFe 2 Se 4 AVEC M = Ti, V, Cr, Fe, Co, Ni. *Le J. Phys. Colloq.* **1971**, *32* (C1), C1-985-C1-986.

(56)   Hirakawa, K. The Magnetic Properties of Iron Selenide Single Crystals. *J. Phys. Soc. Japan* **1957**, *12* (8), 929–938.

(57)   Li, D.; Jiang, J. J.; Liu, W.; Zhang, Z. D. Positive Magnetoresistance in Fe3Se4 Nanowires. *J. Appl. Phys.* **2011**, *109* (7), 07C705.

(58)   Cullity, B. D.; Graham, C. D.; Cullity B. D.; Graham, C. D. *Introduction to Magnetic Materials*, 2nd ed.; John Wiley & Sons, Inc., Hoboken, New Jersey: Hoboken, NJ, USA, 2008; Vol. 53.

(59)   Coey, J. M. D. *Magnetism and Magnetic Materials*; Cambridge University Press: Cambridge, 2010.

(60)   Bedanta, S.; Kleemann, W. Supermagnetism. *J. Phys. D. Appl. Phys.* **2009**, *42* (1), 13001.

Mousumi Sen

(61) Cullity B. D.; Graham, C. D. *Introduction to Magnetic Materials*, 2nd ed.; John Wiley & Sons, Inc., Hoboken, New Jersey, 2009.

(62) Stoner, E. C.; Wohlfarth, E. P. A Mechanism of Magnetic Hysteresis in Heterogeneous Alloys. *Philos. Trans. R. Soc. A Math. Phys. Eng. Sci.* **1948**, *240* (826), 599–642.

(63) Coey, J. M. D.; Spender, M. R.; Morrish, A. H. The Magnetic Structure of the Spinel Fe3S4. *Solid State Commun.* **1970**, *8* (20), 1605–1608.

(64) Long, G.; Zhang, H.; Li, D.; Sabirianov, R.; Zhang, Z.; Zeng, H. Magnetic Anisotropy and Coercivity of Fe3Se4 Nanostructures. *Appl. Phys. Lett.* **2011**, *99* (20), 202103.

(65) Wang, J.; Duan, H.; Lin, X.; Aguilar, V.; Mosqueda, A.; Zhao, G. Temperature Dependence of Magnetic Anisotropy Constant in Iron Chalcogenide Fe3Se4: Excellent Agreement with Theories. *J. Appl. Phys.* **2012**, *112* (10), 103905.

(66) Hayashi, A.; Imada, K.; Inoue, K.; Ueda, Y.; Kosuge, K. Phase Diagram of $(M[x]M_1-[x])_3$ Se_4 $(0 \leqq X \leqq l)$ (M, M' = 3d-Transition Metal). *Bull. Inst. Chem. Res. Kyoto Univ.* **1986**, *64* (4), 186–206.

(67) Kojima, K.; Murase, S.; Sato, K.; Adachi, K. Magnetic Properties of (Fe 1- X M X) 3 Se 4 :M=Ni and Co. *J. Phys. Soc. Japan* **1970**, *29* (6), 1642–1642.

(68) Kojima, K.; Matsui, M.; Sato, K.; Adachi, K. Magnetic Properties of (Fe 1- X Cr X) 3 Se 4. *J. Phys. Soc. Japan* **1970**, *29* (6), 1643–1644.

(69) Li, S.; Li, D.; Liu, W.; Zhang, Z. High Curie Temperature and Coercivity Performance of Fe 3−x Cr X Se 4 Nanostructures. *Nanoscale* **2015**, *7* (12), 5395–5402.

(70) Akhmedov, N. R.; Yalilov, N. Z.; Abdinov, D. S. Electrical Properties of Fe7Se8, Fe3Se4, and NiFe2Se4 Single Crystals. *Phys. Status Solidi* **1973**, *20* (1), K29–K31.

(71) Spender, M. R.; Coey, J. M. D.; Morrish, A. H. The Magnetic Properties and Mössbauer Spectra of Synthetic Samples of Fe 3 S 4 . *Can. J. Phys.* **1972**, *50* (19), 2313–2326.

Mousumi Sen

(72)   REGNARD, J. R.; HOCQUENGHEM, J. C. ÉTUDE PAR EFFET MÖSSBAUER DU COMPOSÉ SEMI-MÉTALLIQUE A ORDRE LACUNAIRE Fe 3 Se 4. *Le J. Phys. Colloq.* **1971**, *32* (C1), C1-268-C1-270.

(73)   Grønvold, F.; Westrum, Jr., E. F.; Stenhagen, E.; Andersson, G.; Stenhagen, E.; Palmstierna, H. Low Temperature Heat Capacities and Thermodynamic Properties of the Iron Selenides Fe1.04Se, Fe7Se8 and Fe3Se4 from 5 to 350 Degrees K. *Acta Chem. Scand.* **1959**, *13*, 241–248.

Mousumi Sen

Chapter 2:

Synthesis and magnetic properties of un-doped and modified Fe$_3$Se$_4$ nanoparticles

Mousumi Sen

The Fe_3Se_4 possesses a large coercivity at room temperature. At lower temperature, a coercivity value up to 40 kOe has been achieved. However, due to relatively lower saturation magnetization value, the energy-product of this material is not suitable for its use as rare-earth-free hard-magnetic material. For the manganese-doped iron-selenide nanostructures, the magnetization value increased from 4.84 to7.54 emu/g, without any change in the Curie temperature and crystalline structure; which is important for its hard magnetic applications. More than 130% increase in the energy-product value is obtained. We also synthesized the nanocomposite of hard/soft magnet—Fe_3Se_4/Fe_3O_4 (exchange spring-magnet) in an effort to increase the energy-product of Fe_3Se_4. With precise control over the interface and proper tuning of the size of hard and soft-phases, clean single-phase behavior in the magnetization is obtained in spite of having two different crystallographic phases present in the sample. Bottom-up assemblage using pre-synthesized nanoparticles gives us precise control over the dimension of the hard and the soft-phase. The Fe_3Se_4:Fe_3O_4 nanocomposite behaves as exchange spring magnet and with inclusion of 10% soft-phase the energy-product increased by 115 %.

2.1: Introduction

Permanent magnets form the basis of enormous number of devices in the modern life. The large market of permanent magnet comprise of wind-turbines, loudspeakers, small rotors, positioning devices in computers, printers, televisions, telephones and some moving parts of automobiles like starters, wipers, fan-motors, window-regulators etc.[1]With the recent thrust on green energy generation, the market demand for hard-magnet is experiencing a many-fold increase. Till now, the conventional rare-earth (RE) hard-magnets have dominated the market and Fe-Nd-B is the most efficient class of permanent magnets known with an energy-product value varying from 20 MGOe to more than 50 MGOe[1–3]. Due to the ever increasing applications of permanent magnets, the demand for Fe-Nd-B magnet has led to heavy mining of RE-minerals. Additionally, the mining of these minerals can be associated with radioactive hazards and can be very expensive. $Nd_2Fe_{14}B$ seems to be an ideal hard-magnetic material. The chances of replacing it with a rare-earth-free material while maintaining the similar energy-product is currently thin, however, for several applications, it is possible to replace them with new RE-free permanent magnetic material which are relatively cheaper and environment friendly to produce.

There is a renewed interest in the development of some novel rare-earth-free magnetic materials. Although, the chances of getting a very high energy-product without using a rare earth ion are very small, still, this upcoming field is receiving a wide attention both in the scientific and industrial community as the raw materials are non-toxic and inexpensive in nature. Many efforts were dedicated to develop a RE-free material[4–6]. Among the RE-free materials, the room temperature ferromagnetic phase of intermetallic compound MnBi is a promising candidate which shows high anisotropy constant (22 Merg/cc at 490 K) and a high coercivity value (up to 23 kOe in thin films), however, low melting

temperature of Bi and high vapour pressure of Mn hinder its processing[7].Among other iron based compounds, FePt is an ideal compound but the cost and availability of platinum makes it unsuitable for mass application and this family of compounds (Co-Cr-Pt alloys)are used successfully in the memory storage applications commercially.

As discussed in the previous chapter, Fe_3Se_4 has started gaining attention lately for displaying some amazing hard-magnetic properties at nano-dimension. The importance of this compound lies in its large uniaxial magnetocrystalline anisotropy.Fe_3Se_4may evolve as a potential option for rare-earth free, environment friendly and cheap permanent magnet.A coercivity value as large as 40 kOe has been achieved at 10 K in Fe_3Se_4 nanostructures by Zhang *et al*[8]. In case of anisotropic nanostructures the anisotropy of the system can be further enhanced. Despite possessing such a unique property, the energy-product of this compound is low because of its low saturation magnetization. At room temperature, typical reported magnetization value at a field of 9 T is ~5emu/g[8],however, smaller values of magnetization, such as 2.2 emu/g [9]forFe_3Se_4 nanostructures are also reported.

The most imperative figure of merit for the hard-magnets is the maximum energy-product $(BH)_{max}$. The energy-product is the maximum amount of magnetic energy stored in the magnet[1]. The theoretical maximum of $(BH)_{max}$ is given by the following equation[2]

$$BH_{max} = \frac{1}{4}\mu_0 M_s^2 \dots\dots\dots\dots\dots\dots\dots\dots\dots\dots\dots(1)$$

where μ_0 is permeability of free space, M_s is the saturation magnetization. As evident from the expression, saturation magnetization (M_s) plays a very important role in deciding energy-product, increasing the M_s value is very crucial for its application as hard-magnetic materials.

As discussed earlier, Fe_3Se_4 is a ferrimagnet at room temperature and the ferrimagnetism arises due to the ordered iron vacancy on the alternate layers of iron[8,10,11].

We have taken two different approaches in an attempt to increase the energy-product of this material. In the first approach, some of the Fe sites were doped with manganese ion. Substitution of some Fe with Mn ions was found to have favorable influence on the net ferrimagnetic moment of the system. We reported a significant increase in saturation magnetization of Fe_3Se_4 nanostructures by doping Mn ions in Fe site, $Fe_{3-x}Mn_xSe_4$ (x = 0.01 to 0.2).

In the second part of this work, the energy-product of Fe_3Se_4 was improved by forming a hybrid material with a soft magnet thereby forming a hard/soft exchange spring magnet. In hybrid materials, the control over surfaces, interfaces, lattice-disorder, doping and imperfections are the keys to achieve novel and enhanced physical, chemical, and biological properties. The control over the interfacial properties has demonstrated its importance in technologies related to semiconductor devices, sensors, magnetic media storage, ferro/piezoelectrics devices etc. in form of superlattices, composites, hybrid materials, and core-shell nanostructures[12-15].

The exchange spring-magnets are a combination of magnetically hard and soft materials, which are designed to provide a large energy barrier to the demagnetization, and larger energy-product while maintaining low volume-fraction of the hard-phase. This is important for the industry to make smaller and efficient permanent magnets for the applications in hybrid cars, wind-turbine engines, memory storage etc[16-19]. In these interfacial materials, the magnetically hard-phase is responsible to induce a large magnetocrystalline anisotropy and a large coercivity whereas the soft-phase increases the saturation magnetization value. The introduction of strong exchange coupling at the

Mousumi Sen

interface of these two materials leads to the formation of spring-magnets, which helps to increase the energy-product of material while reducing the rare earth content and thus reducing the cost of permanent magnets. In an exchange spring magnet, at the interface of both the materials, the spins of the soft-phase are pinned in the direction of hard-phase while at the core of the soft-phase, the spins are free to orient with the external field. The interfacial physics results in the large enhancement in the effective magnetization at the expense of relatively small decrease in the effective coercivity of the hard-phase[16,17,20].

The design and fabrication of exchange spring magnets require a careful selection of hard and soft-phases, a precise control over the structure of both phases, as well as, a strong interfacial exchange coupling. It turns out that interfacial mixing and inter-diffusion between phases at the grain boundaries helps to improve the energy-product of exchange spring magnets rather than a clean interface without interfacial mixing[21]. Therefore, the design of the interface between both the phases becomes challenging and technologically important.

As we mentioned earlier, due to the crucial role of interface in exchange spring magnets, the dimensions of the soft-phase play an important role in the extent of exchange-coupling [16,22]. Typically, the grain-size of the soft-phase should be comparable with the width of the domain-wall of the hard-phase[20]. This condition imposes significant challenges in fabricating these two-phase magnets. Traditionally, some of the known rare-earth and hexa-ferrite type hard-magnets have shown improved properties after interfacial coupling with transition metal based soft magnets by various approaches such as self-assembly[18,23], melt-spinning[24], mechanical-milling [25] and dc- magnetron sputtering[21,26]. It was shown in Sm-Co/Fe bilayer system that the inter-diffusion at the interface through thermal processing resulted in the enhanced nucleation field and energy-product.[21,25]The barium hexa-ferrite and magnetite nanocomposite, prepared by solution method, showed a

13 % increase in the energy-product after sintering at high temperature [21]. However, as we discussed earlier, the exchange spring behavior is extremely sensitive to the interfacial properties and the enhancement was observed only for a particular combination of hard and soft-phases and under a suitable heat treatment [19,21,24].

In this work, we report the fabrication of an interfacial, hybrid, nanocomposite system based on a combination of inexpensive and environment friendly $Fe_3Se_4:Fe_3O_4$ synthesized via a simple solution based method. The Fe_3O_4 nanoparticles, with average size around 5 nm, are chosen as the soft magnetic phase to fabricate the exchange spring nanomagnets as the dimension of these particles are comparable to the domain wall width of hard magnets which is crucial for effective exchange spring coupling as discussed before. Magnetite (Fe_3O_4) nanoparticles are well researched for their various properties such as Verwey metal to insulator transition in ~ 8 nm oleic-acid coated particles[27,28], spin-dependent electron scattering and magnetoresistance and collective spin behavior and spin relaxation studies in their 2-dimensional arrays[29]. Similar to the iron selenide, Fe_3O_4 is also a ferrimagnet. However, unlike iron selenide, it crystalizes in reverse spinel phase and is a soft magnet. The bulk magnetization of Fe_3O_4 is ~ 92 emu/g anisotropy constant ~ 1.35×10^5 erg/cm^3 [30] while for Fe_3Se_4 the and anisotropy constant is around two orders of magnitude larger ~ 1.2×10^7 erg/cm^3 [9]. The Curie temperature of Fe_3O_4 is much larger ~ 858 K than that of Fe_3Se_4 ~ 317 K.

In this chapter, both the above approaches to increase the energy-product are explained.

Section 2.2: Increasing the energy-product of Fe_3Se_4 by Fe-site doping

2.2.1.Experimental section

Materials. Iron(III) 2,4-pentanedionate [$Fe(acac)_3$] (>97%), manganese(III) 2,4-pentanedionate [$Mn(acac)_3$] (technical grade), Se (powder, 99.999%) and oleylamine(80-90%) were purchased from Sigma-Aldrich and were used without any further purification.

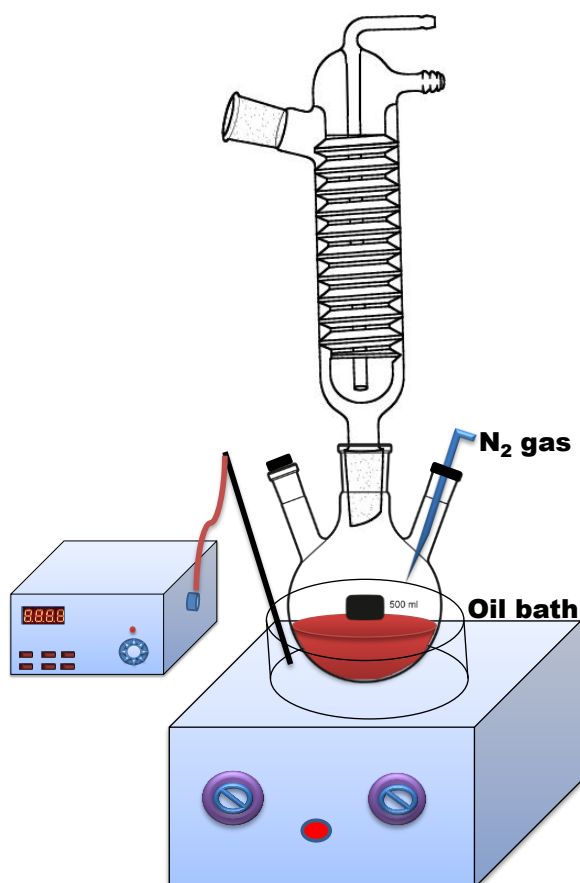**Synthesis of Fe_3Se_4 nanoparticles:**

Figure 2.2: Schematic of the synthesis process of Fe_3Se_4 nanoparticles by high temperature organic solution phase method in triple-neck flask under nitrogen atmosphere.

Mousumi Sen

The synthesis was done by a high temperature organic solution phase method as reported elsewhere[8]. Briefly, 0.53 g (1.5 mmol) of Fe(acac)$_3$ and 0.158 g (2 mmol) of Se powder were added to 15 ml of oleylamine in a 100 ml three-neck flask under N$_2$ atmosphere. The mixture was heated to 120 °C and kept for 1 h (see figure 2.2). Then, temperature was increased to 200 °C and kept for 1 h. Finally, the solution temperature was raised to 300 °C and kept for 1 h. After 1 h, the heat source was removed and solution was allowed to cool down naturally to room temperature. The Fe$_3$Se$_4$ nanoparticles were precipitated by the addition of 20 ml of 2-propanol. The precipitate was then centrifuged and washed with solution containing hexane and 2-propanol in 3:2 ratio.

Synthesis of Mn-doped Fe$_3$Se$_4$ nanoparticles:

[Fe(acac)$_3$] and [Mn(acac)$_3$] were mixed in a certain ratio (total 1.5 mmol) to synthesise Mn-doped iron selenide nanoparticles (Fe$_{3-x}$Mn$_x$Se$_4$)with x = 0.01, 0.02, 0.03, 0.04, 0.05, 0.07, 0.1, 0.2.

2.2.2 Characterization methods:

Powder X-ray diffraction (XRD) patterns were collected using PANalytical X'PERT PRO instrument using iron-filtered Cu - Kα radiation (λ = 1.5406 Å) in the 2θ range of 20 – 70º with a step size of 0.02°. The size and morphology of the prepared particles were obtained by using FEI Tecnai F30 high resolution transmission electron microscope (HRTEM) equipped with a super-twin lens (s-twin) operated at 300 keV accelerating voltage with Schottky field emitter source with maximum beam current (> 100 nA)and small energy spread (0.8 eV or less).The point to point resolution of the microscope is 0.20 nm with a spherical aberration of 1.2 mm and chromatic aberration of 1.4 mm with 70 μm objective aperture size. The powders obtained were dispersed in

hexane and then drop-casted on carbon-coated copper TEM grids with 200 mesh and loaded to a single tilt sample holder.

Raman spectra were recorded on a HR-800 Raman spectrophotometer (JobinYvon-Horiba, France) using monochromatic radiation emitted by a He–Ne laser (633 nm), operating at 20 mW and with accuracy in the range between 450 nm and 850 nm $\pm$ 1 cm^{-1}, equipped with thermoelectrically cooled (with Peltier junctions), multi-channel, spectroscopic grade CCD detector(1024$\times$256 pixels of 26 microns) with dark current lower than 0.002 electrons pixel^{-1} s^{-1}. An objective of 50 X LD magnification was used both to focus and collect the signal from the powder sample dispersed on glass slide.

Static magnetic property measurements of Fe_3Se_4 nanoparticles were performed using a Physical Property Measurement System (PPMS) from Quantum Design Inc., San Diego, California equipped with a 9 Tesla superconducting magnet. We performed dc-magnetization *vs.* temperature (M–T) and magnetic field *vs.* magnetization hysteresis (M–H) measurements using a vibrating sample magnetometer (VSM) attachment. For DC magnetic measurements, the samples were precisely weighed and packed inside a plastic sample holder which fits into a brass sample holder provided by Quantum Design Inc. with negligible contribution in overall magnetic signal. We collected M – H loops at a rate of 50Oe/s in a field sweep from - 85 to 85kOe at the vibrating frequency of 40 Hz. The M - T measurements were also carried out in temperature range from 3 – 350 K at 100 Oe. The cooling and heating rates were kept constant at 2 K/min for all the measurements. Firstly, at 350K, the desired field was applied and the system was cooled down to 3 K and data were recorded while heating the sample from 3 to 350 K. The curve obtained was designated as field cooled (FC) cooling and field cooled heating respectively. For zero field cooled (ZFC) measurements, the sample was first cooled from 350 to 3 K in zero magnetic field and data was collected in heating mode once the field was applied at 3 K.

2.2.3: Results and discussion

2.2.3.1. X-ray diffraction:

The crystal structure of Fe_3Se_4 was characterized from the powder X-ray diffraction patterns. The XRD peaks of the pure Fe_3Se_4 nanostructures are in good agreement with bulk Fe_3Se_4 (JCPDS card no. 657252), which has monoclinic structure with a space group I2/m (12) and unit cell lattice parameters $a = 12.73$, $b = 3.493$, $c = 6.159$Å (Fig 2.3 top panel). The strongest line in the pattern corresponds to (111) plane. No significant changes in the peak positions were observed in the XRD patterns of Mn- doped samples compared with undoped Fe_3Se_4 (Fig. 2.3 bottom panel). Some peak broadening was observed for the (311) and ($\bar{6}$02) doublet peak with increasing doping concentration. The peak broadening might be due to the increase in lattice-strain after doping with Mn.

Moreover, the X-ray form factor for Fe and Mn is 15.6 and 14.9 respectively and ionic-radii for Fe^{3+} and Mn^{3+} is 55, 65 pm respectively. Therefore, it is difficult to interpret intensity profile from Fe and Mn using lab source X-ray diffractometer. For the highly doped samples (x = 0.1 and 0.2), the intensity of ($\bar{1}$12) and ($\bar{6}$02) peaks decrease slightly compared to other lightly doped samples. The reason for this decrease of intensity of ($\bar{1}$12) and ($\bar{6}$02) peaks is not clear to us yet.
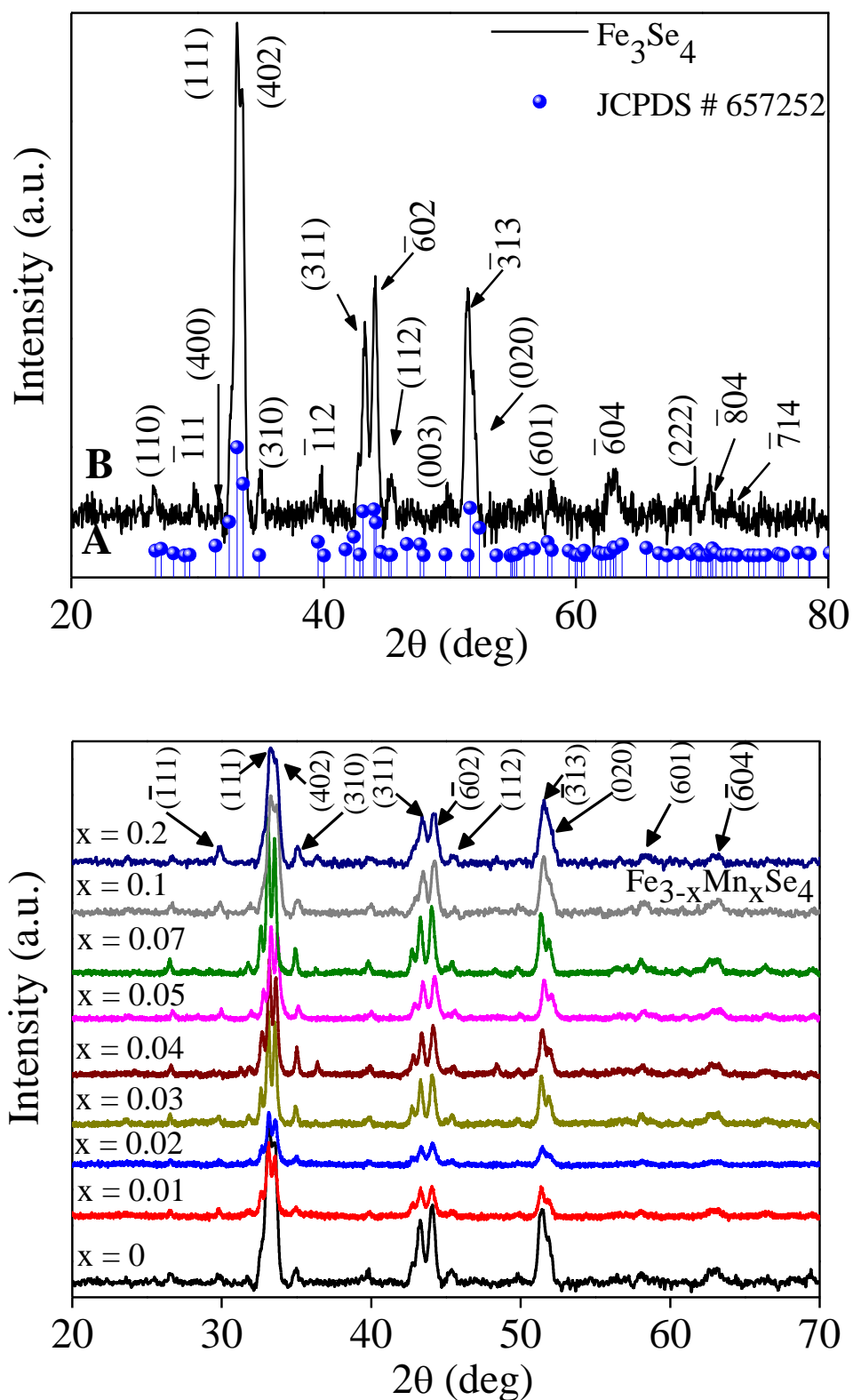
Figure 2.3: Powder XRD patterns of $Fe_{3-x}Mn_xSe_4$ (x = 0 - 0.2) nanorods. In the top panel the XRD pattern of Fe_3Se_4 nanoparticles is plotted with JCPDS # 657252.

2.2.3.2. Electron microscopy- imaging and diffraction study

The HRTEM study of the Fe_3Se_4 nanostructures and Mn-doped nanostructures shows that the rod-shaped nanostructures are highly aggregated for all the samples (Fig 2.4.1 and 2.4.2) due to their ferrimagnetic nature at room temperature. Moreover, the image quality for magnetic particles is also affected due to the strong Lorentz interaction of electrons with oriented spins inside the particles. The diameter of the nanorods is in the range of 30-50 nm. From high resolution images (see Figure 2.4.3), the lattice fringes with inter-planar distances $d_{111} = 0.27$ nm are clearly visible (which is slightly larger than the point resolution of our microscope in Scherzer defocus condition and atoms are visible as dark spots). No significant changes in the morphology, size, and inter-planar distance of rods are observed after Mn-doping. The selected area electron diffraction (SAED) pattern (fig 2.4.4) which is due to random orientation of large collection of such particles contributing from selected area by SAED aperture in back focal plane of electron microscope. From the energy dispersive spectra (EDS) of as-synthesized Fe_3Se_4 nanostructures, the K_α emission gives the ratio of atomic % of iron and selenium to be 0.75).

Figure 2.4.1: High-resolution transmission electron microscope images (a)for Fe_3Se_4 and (b-h) for $Fe_{3-x}Mn_xSe_4$ (x = 0.01, 0.02, 0.03, 0.04, 0.05, 0.07, and 0.1) samples at 200 nm scale.
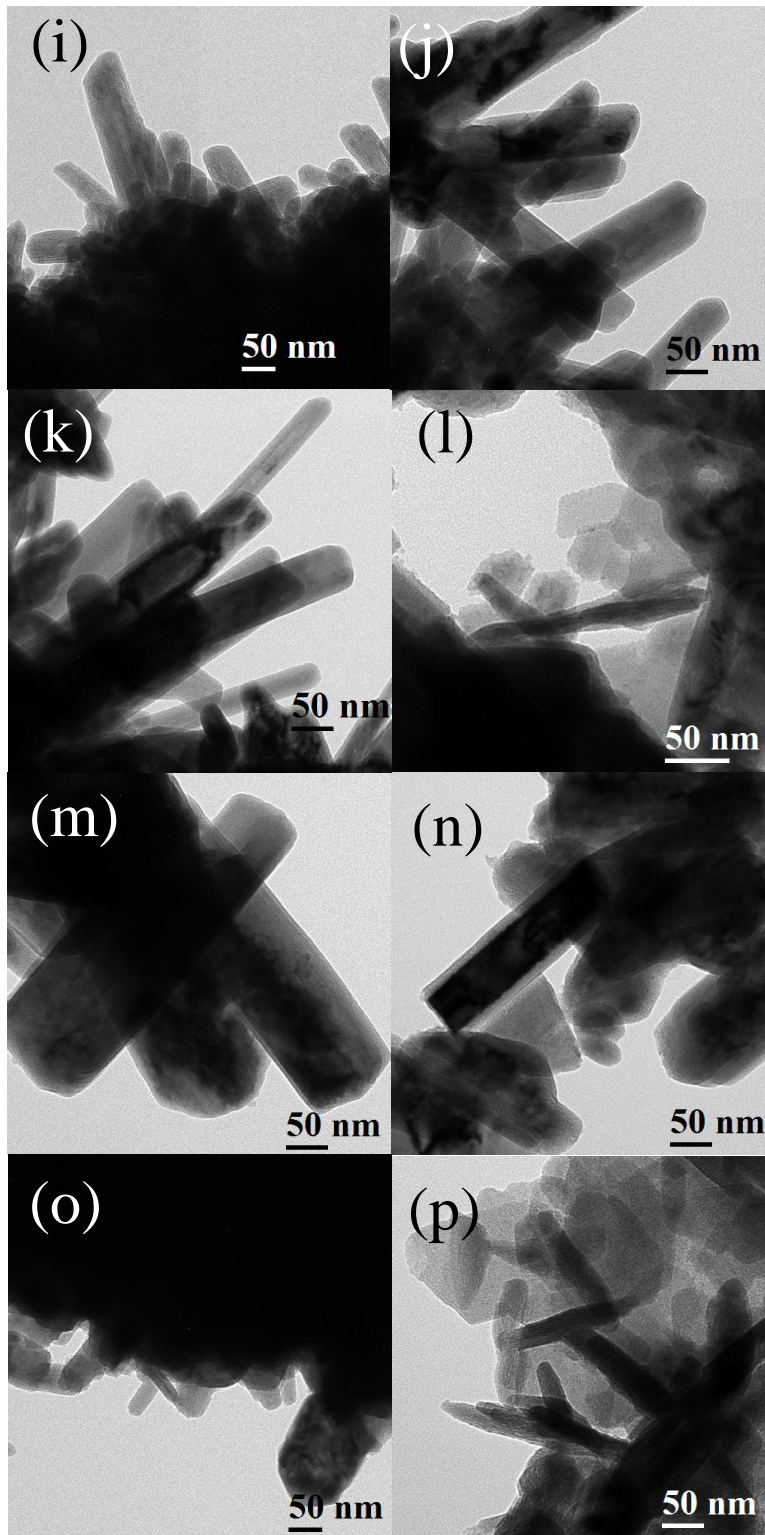
Figure 2.4.2: High resolution transmission electron microscope images (i-p) for $Fe_{3-x}Mn_xSe_4$ (x = 0.01, 0.02, 0.03, 0.04, 0.05, 0.07, and 0.1) samples at 50 nm scale.

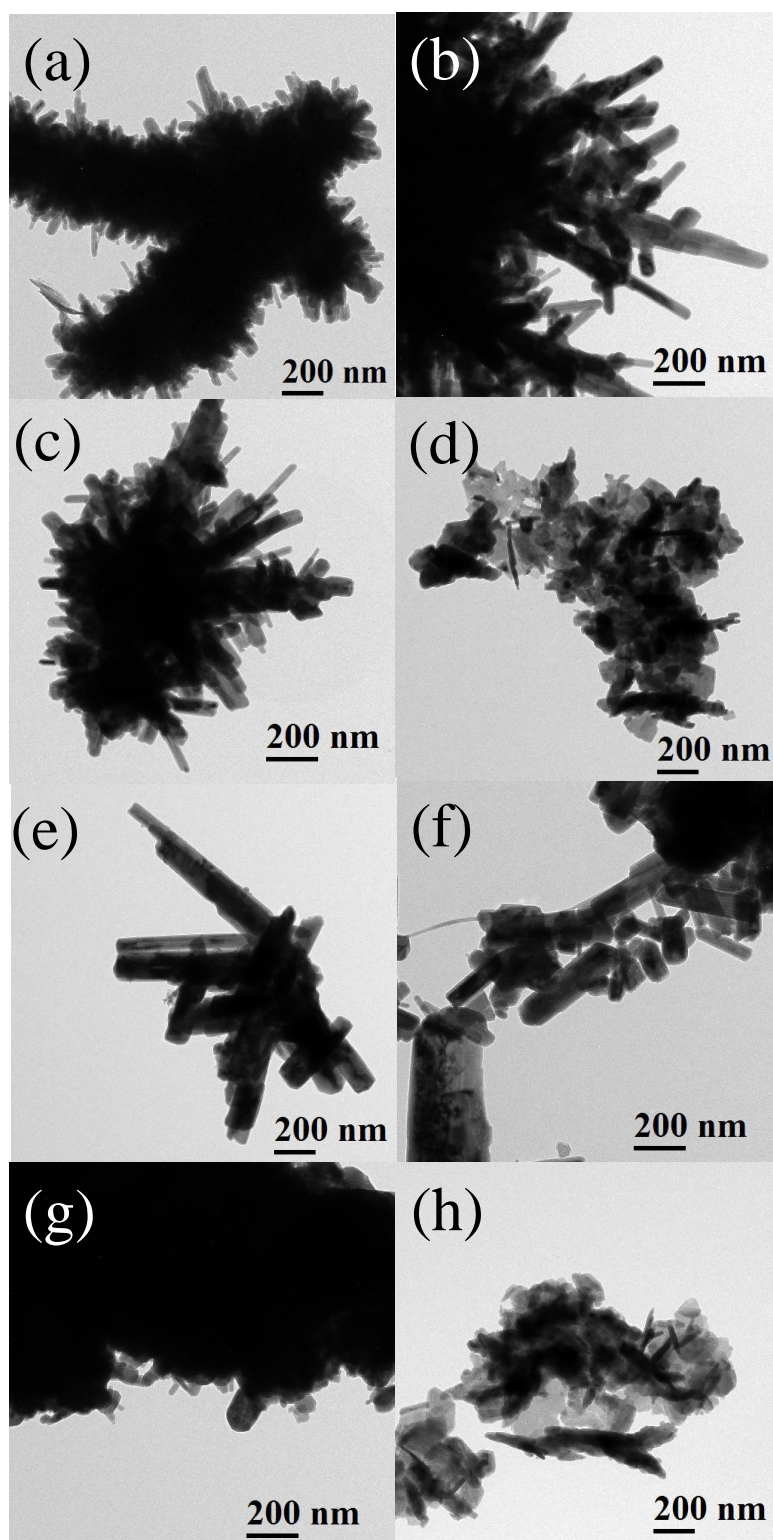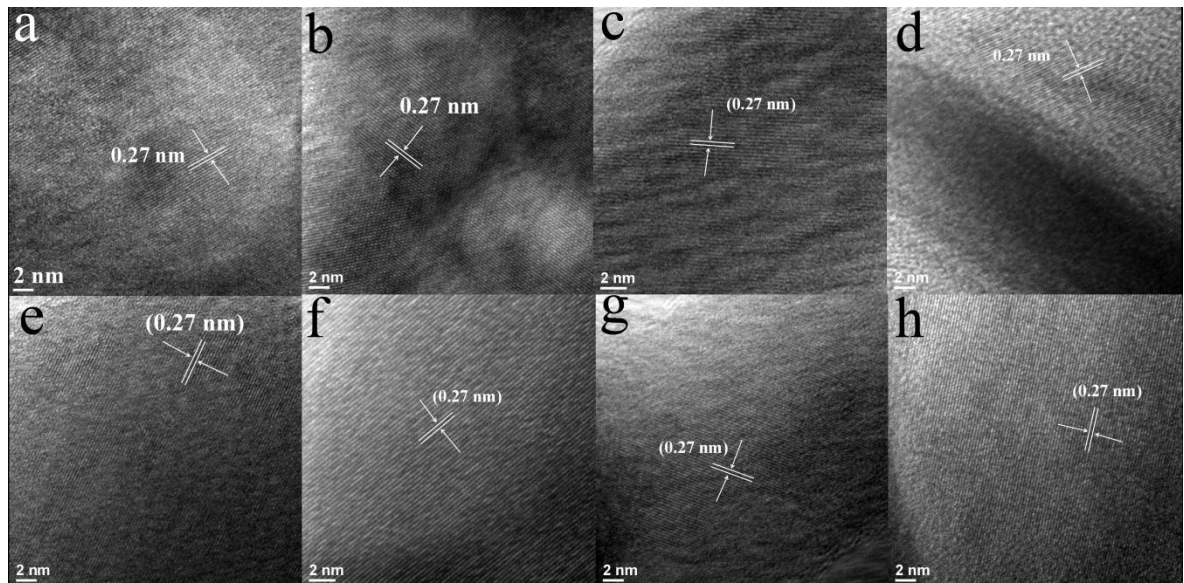**Figure 2.4.3:** High-resolution transmission electron microscope images (a-h) for $Fe_{3-x}Mn_xSe_4$ (x = 0, 0.01, 0.02, 0.03, 0.04, 0.05, 0.07, and 0.1) samples respectively.
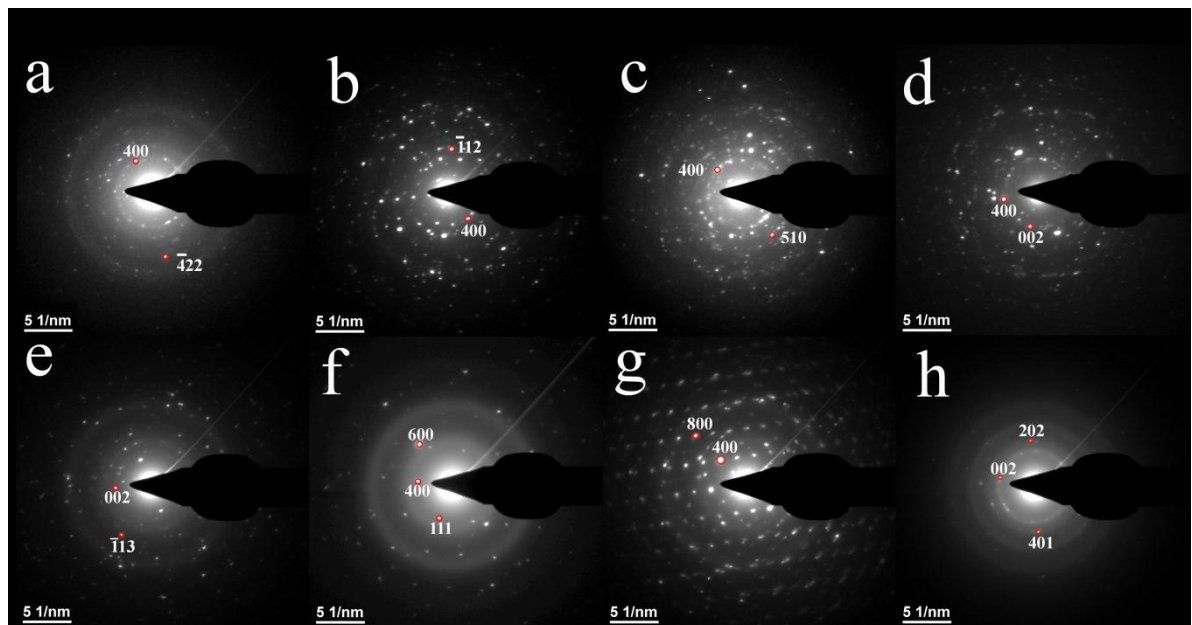
Figure 2.4.4: Selected area electron diffraction pattern (a-h) for $Fe_{3-x}Mn_xSe_4$ (x = 0, 0.01, 0.02, 0.03, 0.04, 0.05, 0.07, 0.1) samples respectively.

2.2.3.3 Raman study

Raman scattering is an excellent tool to study the lattice-strain and bond-disorder. We observed that the Raman spectra of all samples (doped and undoped) are similar with little shift in peak position and change in full-width at half-maximum (FWHM). We believe that this is the first investigation of Raman spectra of Fe_3Se_4 and therefore due to the absence of any previous report on Raman spectra ofFe_3Se_4 in the literature, we compared our results with β-Mg_2SiO_4 which crystallizes in the same*I2/m* space-groupsymmetry[31,32]. The peaks at ~ 228 and 411 cm^{-1} in Fe_3Se_4 spectra can be assigned to Fe-Se vibration modes[33,34] (Fig. 2.5). It was found that both the Raman peaks shift to lower cm^{-1} as the Mn-doping concentration increases and shows a dip at x= 0.05 and then again shifts to higher cm^{-1}. From this observation, it can be concluded that for the increase in the doping till x= 0.05,the lattice strain decreases and for higher doping the lattice strain increases. The FWHM also shows the same doping concentration (x= 0.05) as peak and higher doping concentration samples shows almost similar values of FWHM (figure 2.6). The increase in FWHM can be due to increase in disorder in lattice.
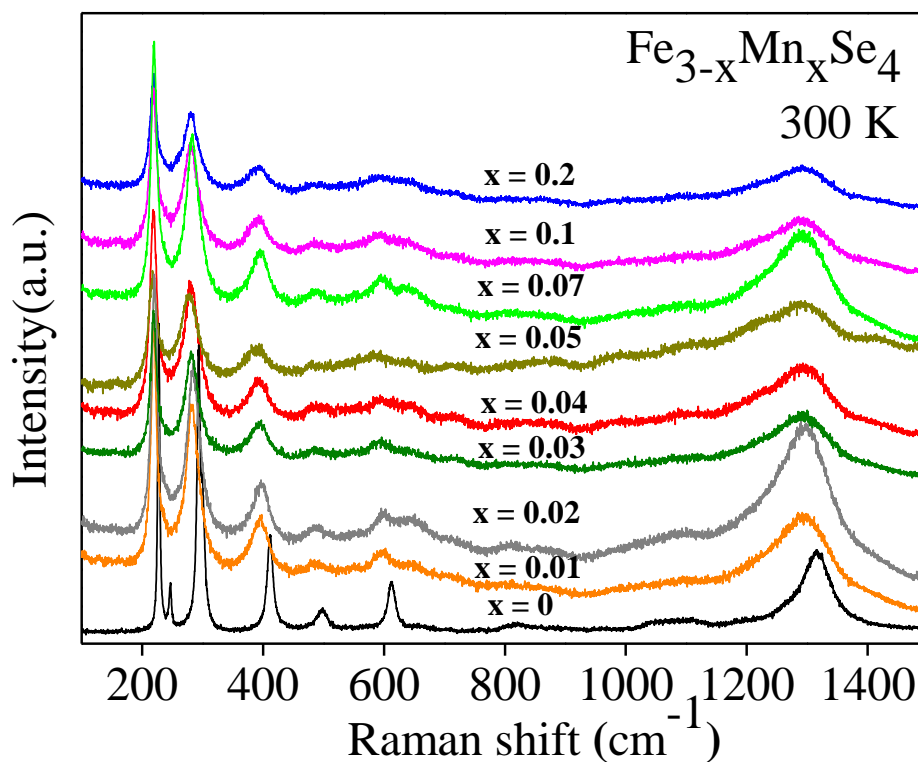
Figure 2.5: Raman shift of $Fe_{3-x}Mn_xSe_4$ (x = 0 - 0.2) nanorods plotted from 100-1500 cm⁻

Mousumi Sen
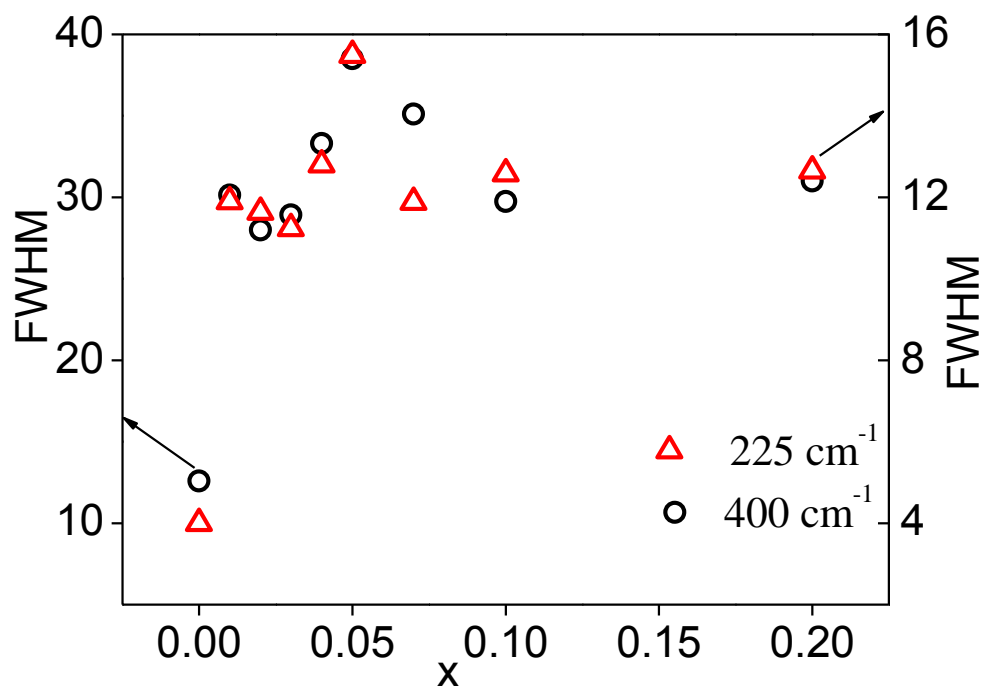
Figure 2.6: Variation of the FWHM of Raman modes of 225 cm^{-1} and 400 cm^{-1} in the Raman spectra with doping concentration x.

2.2.3.4. Magnetic studies

The temperature dependent magnetization is measured in 100 Oe field. From the M-T curve, Curie temperature of iron selenide nanoparticles is found to be 323 K where a peak in the ZFC magnetization curve is observed (Fig. 2.7 A).According to earlier reports of doping with transition metals [8], the Curie temperature and the saturation magnetization decreased with increased concentration of Co ion doping and the samples become paramagnetic at room temperature. Coercivity at room temperature was reduced to zero with cobalt ion doping. From the zoom view of the M-T curve (Fig. 2.7 B), it is clear that the Curie temperature does not change with Mn ion doping.

Mousumi Sen

Mousumi Sen
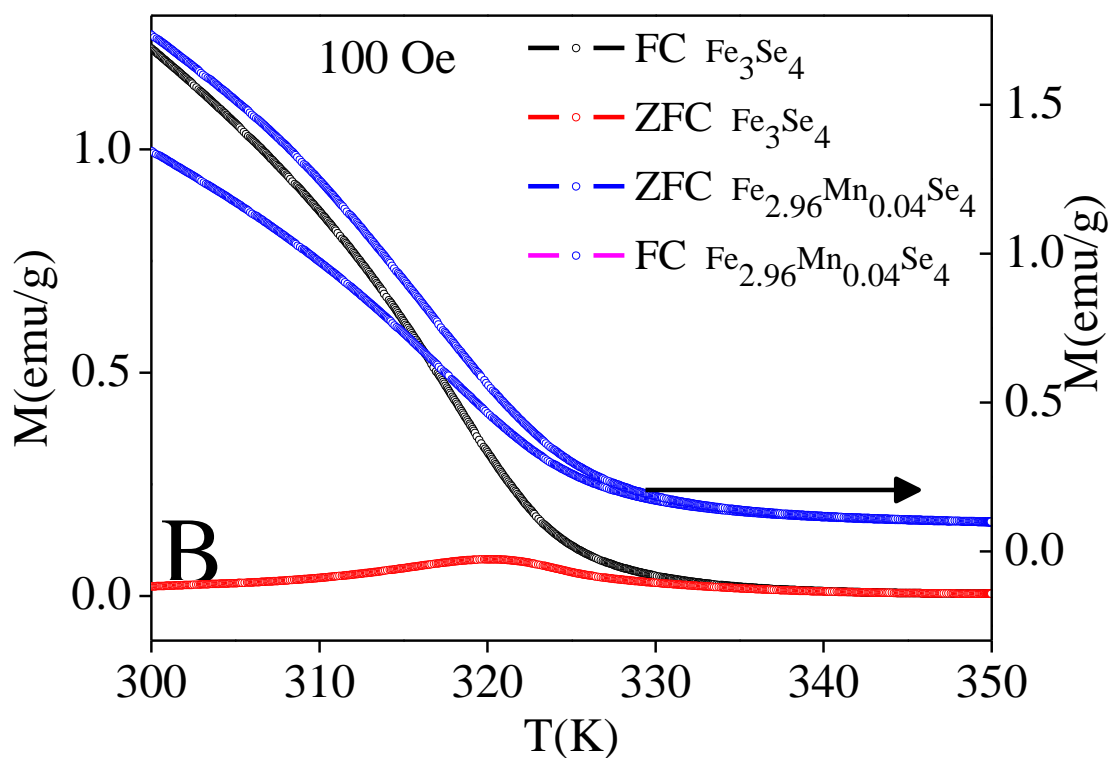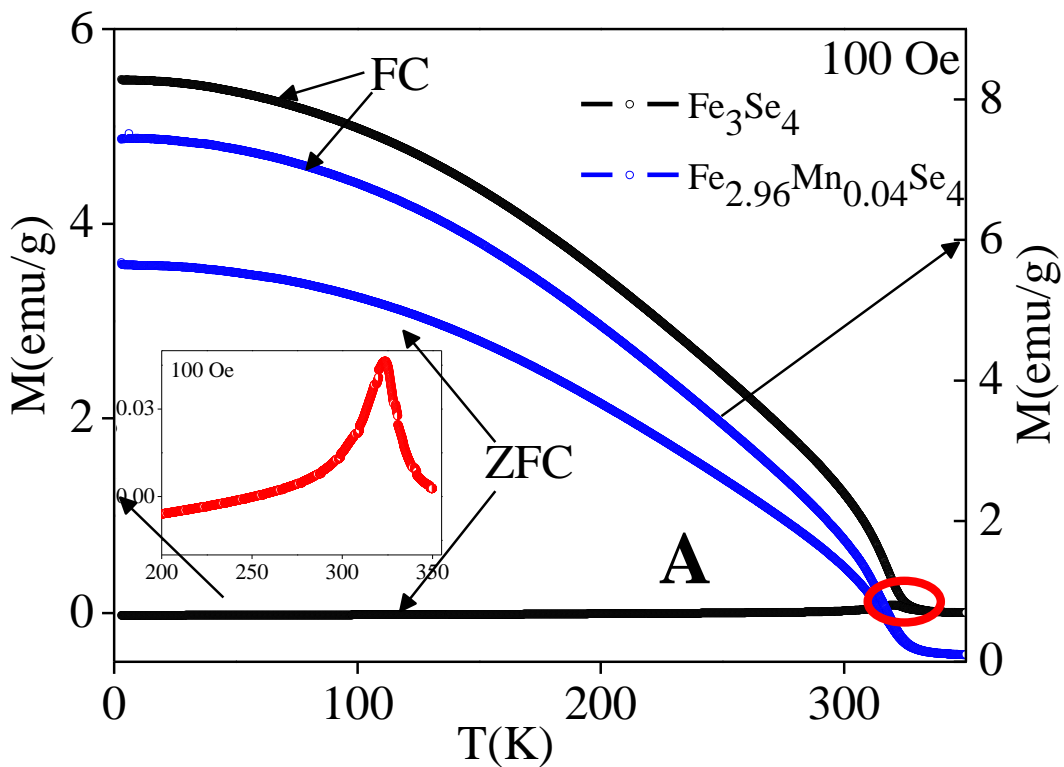
Figure 2.7(A): A comparison of magnetization versus temperature curves (in ZFC and FC modes) for undoped and doped (x = 0.04) Fe_3Se_4 nanorods. The inset shows the zoomed view of the encircled region of ZFC curve. **(B):** A zoomed view of the M-T curve around the transition temperature to show that the Curie temperature does not change with doping.

All the doped and undoped samples show hard-magnetic properties(Fig. 2.8).The room temperature coercivity (H_c) of Fe_3Se_4 is found to be 2.74 kOe. This coercivity value is comparable to the RE-based nanoparticles of $SmCo_5$(H_c= 2- 8 kOe) and $Nd_2Fe_{12}B$ (H_c=1.2- 4 kOe) [35–38].
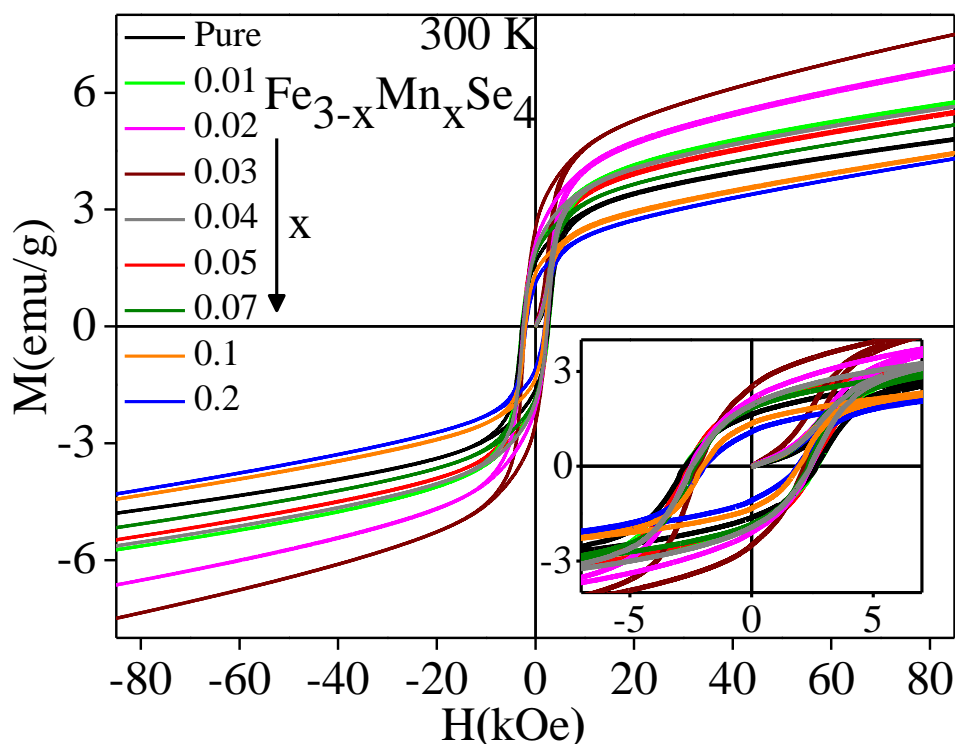
Figure 2.8: A comparison of M-H curves for $Fe_{3-x}Mn_xSe_4$(x= 0, 0.01, 0.02, 0.03, 0.04, 0.05, 0.07, 0.1, and 0.2) nanorods at 300 K.

Mousumi Sen

Inset of Fig 2.8 shows a zoom view of hysteresis curves clearly depicting the coercive and remanence field for samples with varying doping concentration. At lower temperature a colossal increase in coercivity is observed and H_c value reaches up to ~27.08 kOe at 10 K (Fig. 2.9) which is in good agreement with the earlier reports[8,9,39]. M-H data shows no saturation of magnetization even at the field value of 8.5 T (Fig. 2.8).This may be due to a superparamagnetic contribution in the magnetization which may come from some ultrafine particles[9], also, any 'ferri'-magnetic system requires higher field to align all the spin and the particles may have uncompensated spin and spin disorder at the surface of nanorods. For $Fe_3Se_4$the magnetization at 8.5 T is 4.8 emu/gat 300 K, which increases to 14.18 emu/g at 10 K (Fig. 2.9).The saturation magnetization is determined from the M versus 1/H plot at high field range (above 6 T).As we increase the Mn doping concentration slowly from x = 0.01 to 0.03, the magnetization value (M_s) increases from 5.76 emu/g to 7.5 emu/g, the remanence magnetization (M_r) also shows an increase in this range. Beyond x = 0.03, (for x = 0.04, 0.05, 0.07) the M_s values decrease with increase in doping concentration. As the Mn doping is further increased (x = 0.1, 0.2), the saturation magnetization shows a significant decrease and drops even below Fe_3Se_4 sample (Table 2.1).A similar phenomenon of decrease in saturation magnetization at higher doping concentration is also observed when monoclinic zirconia is doped with manganese ions [40]. The reason for this decrease in saturation magnetization with higher Mn ion concentration may be attributed to the antiferromagnetic coupling between manganese ions at higher doping concentration [23].

For Fe_3Se_4 the M_r/M_s value was found to be 0.336, for heavily doped sample (x= 0.2) this ratio drops to 0.247 (Fig. 2.10). The coercivity experiences a very small decrease with manganese doping for low doping concentration. But for x = 0.1 and 0.2, the

coercivity reduces significantly (Table 2.1). The reason for increase in saturation magnetization initially with manganese ion doping may be due to the net contribution of Mn ions to the ferrimagnetic moment. At 10 K, the coercivity of Fe_3Se_4 increases to 29.5 kOe, which is 10 folds greater than the value at 300 K. The M-H loop becomes close to square at 10 K and the M_r/M_s ratio increases to 0.587.
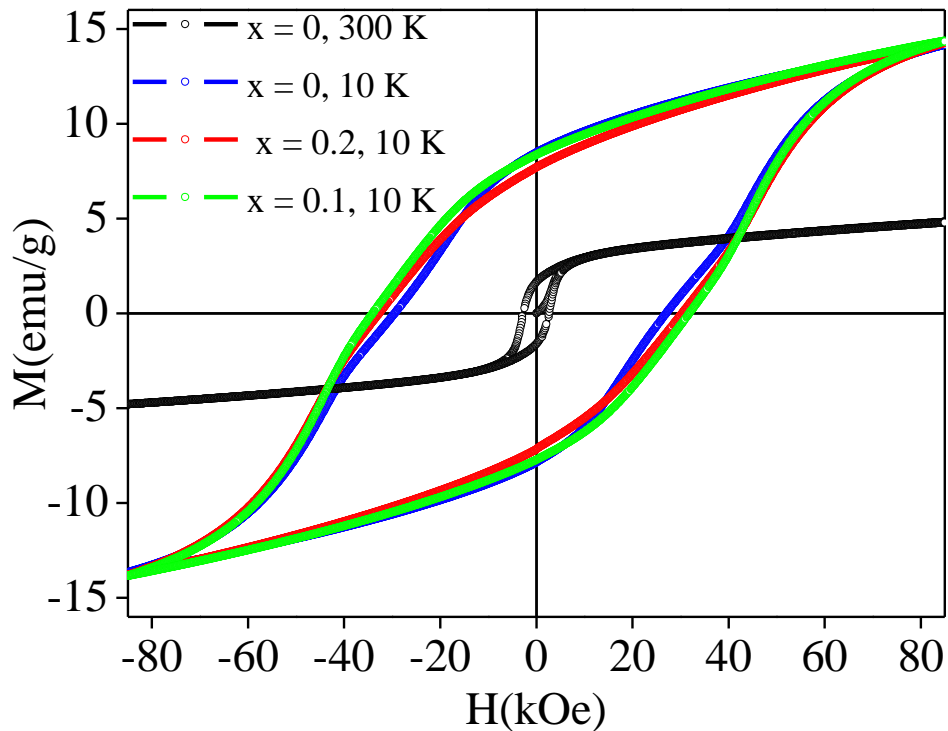
Figure 2.9: A comparison of M-H curves for $Fe_{3-x}Mn_xSe_4$ (0, 0.1, and 0.2) nanorods at 10 K and 300 K.

The upper limit to coercivity is determined by the anisotropy field of the material, as a general trend coercivity of the material reaches near 25% of the anisotropy field. We have determined the anisotropy field by the extrapolating the magnetization graph in easy and hard axis direction [41,42]. The anisotropy constant (K) at 300 K was calculated from the

saturation magnetization (M_s) and anisotropy field (H_a) according to the following equation.

$$K = \frac{1}{2} M_s H_a$$
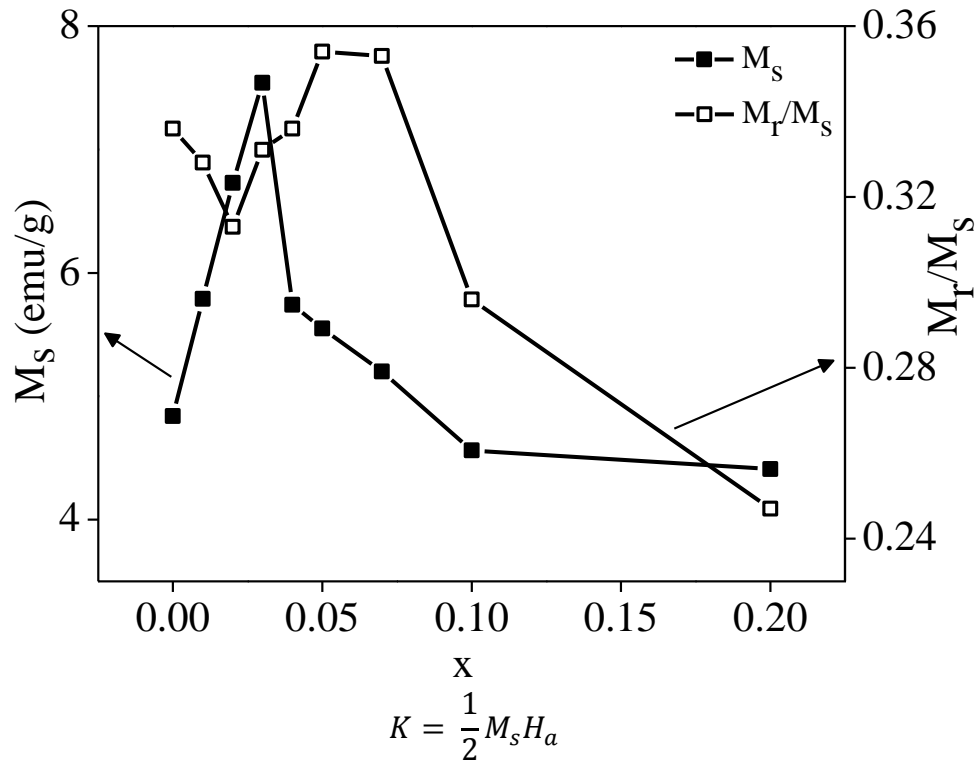
At 300 K, the K for Fe_3Se_4 is 1.12×10^5 erg/cc. The K value was determined for all the 9 samples and is tabulated under Table 1. As observed earlier[8], K value for Fe_3Se_4 is an order of magnitude higher than Fe_3O_4.

Figure 2.10: Variation of M_s and M_r/M_s ratio with doping concentration (x) for $Fe_{3-x}Mn_xSe_4$ nanorods.

The energy-product of all the samples was calculated from the 3rd quadrant of the B-H hysteresis loop at 300 K. The 3rd quadrant of the B-H loop for pure Fe_3Se_4 nanostructures is shown in figure2.11. The area under the shaded portion represents the energy-product of the sample. For Fe_3Se_4 the energy-product is found to be 4.38 kGOe,

which increases to 10.22 kGOe for $Fe_{2.97}Mn_{0.03}Se_4$. The practical energy-product that we can get from a permanent magnet depends strongly on its processing. The alignment of easy-axes in a particular direction can greatly enhance the M_r/M_s ratio and help in increasing the energy-product. Compacting the magnetic nanoparticles with high packing densities is very crucial for development of permanent magnets. This enhancement of energy-product by more than 130% is a vital step in developing new rare earth free alternative to permanent magnets.
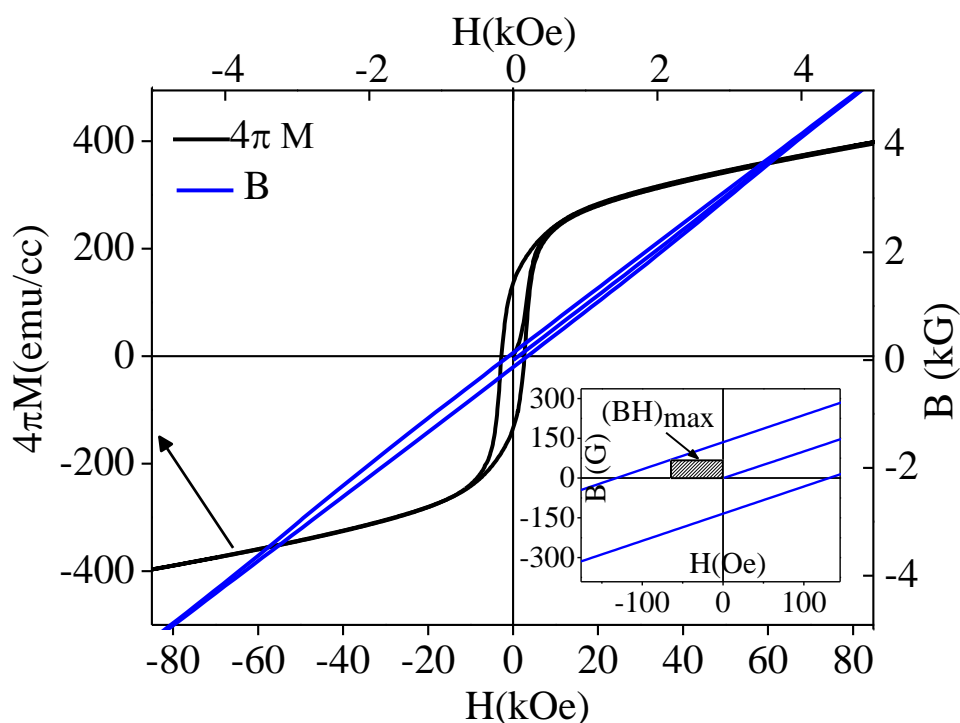
Figure 2.11: M-H plot and B-H plot for Fe_3Se_4nanocrystals at 300 K (inset: Calculation of maximum energy-product from the B-H hysteresis loop of Fe_3Se_4 at 300 K).

Table 2.1: Summary of magnetization parameters calculated for $Fe_{3-x}Mn_xSe_4$ nanorods at 300 K.

S. No.	Sample $Fe_{3-x}Mn_xSe_4$	H_C (kOe)	Ms(emu/ g)	M_r (emu/g)	M_r/M_s	H_a (kOe)	K (erg/cc)	BH_{Max} (kGOe)
1	X = 0	2.74	4.84	1.63	0.336	7.053	1.12×10^5	4.377
2	X = 0.01	2.76	5.79	1.9	0.328	7.376	1.4×10^5	5.858
3	X = 0.02	2.47	6.73	2.11	0.313	6.028	1.33×10^5	7.352
4	X = 0.03	2.17	7.54	2.5	0.331	5.169	1.38×10^5	10.22
5	X = 0.04	2.4	5.74	1.93	0.336	6.054	1.14×10^5	6.139
6	X = 0.05	2.65	5.55	1.97	0.354	6.427	1.17×10^5	6.457
7	X = 0.07	2.3	5.20	1.84	0.353	5.497	0.94×10^5	5.575
8	X = 0.1	1.99	4.56	1.35	0.296	5.154	0.82×10^5	3.08
9	X = 0.2	1.94	4.41	1.09	0.247	5.211	0.75×10^5	1.953

Mousumi Sen

Section 2.3: Increasing the energy-product of Fe$_3$Se$_4$ nanoparticles by forming hybrid with soft magnet.

Iron selenide and magnetite nanoparticles are synthesized by a high temperature hot-colloidal method under inert atmosphere as described elsewhere [8,43] .

2.3.1. Experimental section:

Synthesis of Fe$_3$Se$_4$ nanoparticles: Fe$_3$Se$_4$ nanoparticles were synthesized as discussed in section **2.2.1.**

Synthesis of Fe$_3$O$_4$ nanoparticles: Iron(III)acetylacetonate (2 mmol), 1,2-hexadecanediol (10 mmol), oleic acid (6 mmol), oleylamine (6mmol), and phenyl ether (20 mL) were mixed and stirred under a flow of nitrogen. The temperature was increased up to 200 °C and was kept at that temperature for 30 min and then, heated to reflux (265 °C) under nitrogen gas for another 30 min. The black mixture was then cooled to room temperature. With the addition of ethanol (40 mL) to the mixture, a black material was precipitated. The black product obtained was dissolved in hexane in the presence of oleic acid (~0.05 mL) and oleylamine (~0.05 mL). To remove excess oleic acid and oleyl amine the precipitate was washed in ethanol and then dispersed in hexane.
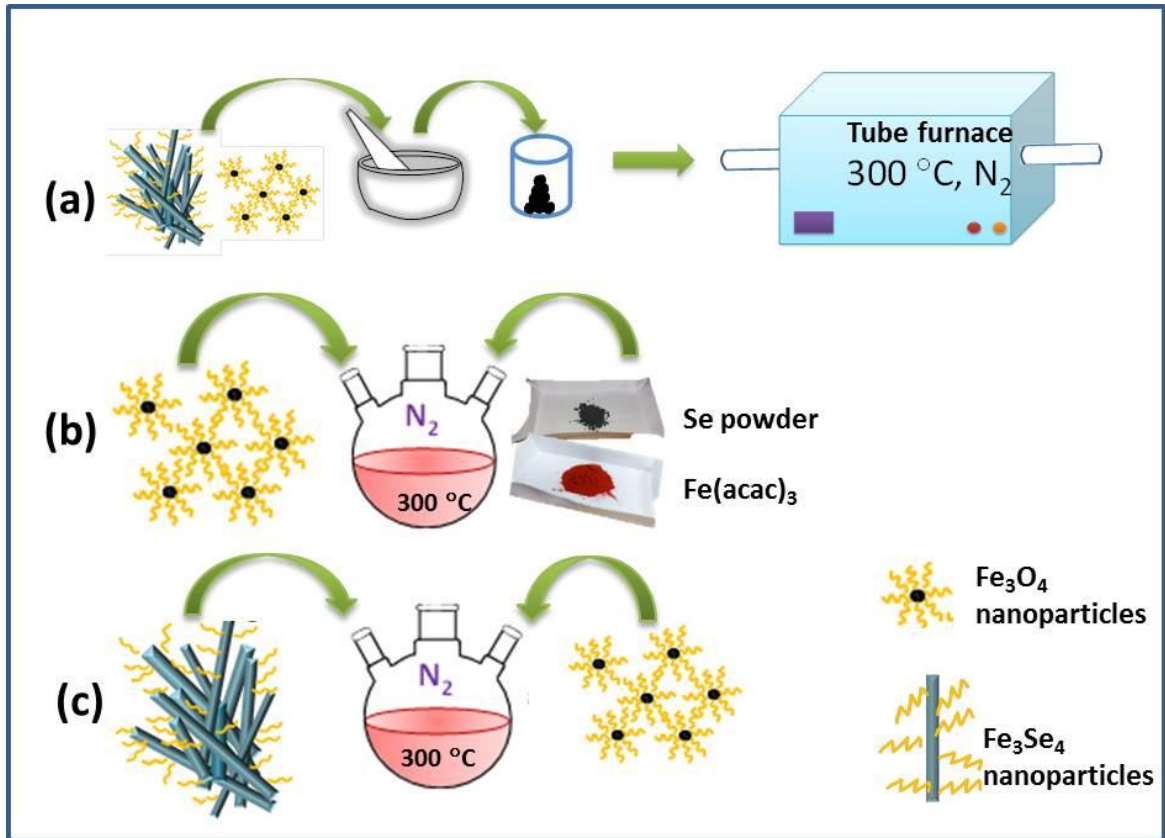
Figure 2.12: Schematic for the development of exchange spring magnet Fe_3O_4:Fe_3Se_4 nanocomposites through three different routes— (a), (b) and (c). The detailed procedures are mentioned in the text.

Synthesis of the Fe₃Se₄:Fe₃O₄ nanocomposite: We have taken three different approaches for developing the hard: soft nanocomposites as discussed below (see figure 2.12).

(a) Here, the pre-synthesized hard and soft nanoparticles are ground together in powder form in mortar and pestle and then subjected to heating in tube furnace under inert atmosphere at 300 °C for one hour**.**

(b)Measured amount of Fe_3O_4 nanoparticles were taken in a round bottom flask in 15 ml oleylamine and sonicated for 10 minutes so that they are well dispersed in the solvent. Then Fe_3Se_4nanorods were synthesized as mentioned in section 2.1using this oleylamine containing Fe_3O_4 nanoparticles.

(c) In this approach, nanocomposites are prepared by a high temperature solution method. Hard and soft-phase nanoparticles are synthesized according to section 2.1 and 2.2. The measured amount of powder form of these nanoparticles are added to 15 mL oleyl-amine and refluxed under nitrogen atmosphere at 300 °C for 1 h. Thereafter, after cooling naturally to room temperature, the samples were washed with 2-propanol and n-hexane (in 3:2 ratio) and were dried. The obtained powder was used for all further characterization. No further sintering of the samples was done. Three samples were made with different Fe_3O_4 weight % of 3.3, 5, and 10 and were named as F3.3, F5, and F10 respectively. It is known that the formation of a capping layer by capping agents is a dynamic process in the solution, where the molecules adsorbed at the surface of the nanoparticles are in dynamic equilibrium with the molecules in the solution. During refluxing, nanoparticles of both the phases come in close proximity to each other and oleyl-amine molecules form an overall coating on these nanocomposite particles (see the schematic shown in Fig. 2.12).

Nanocomposites made only by approach (c) shows good reversible magnetization behavior and behave as a single phase in magnetic hysteresis measurements as can be seen later in the paper. So, samples F3.3, F5, and F10 are used for all the further experiments reported here.

2.3.2: Results and discussion:

2.3.2.1: Structural characterization by powder X-ray diffraction:

Figure 2.13 shows the powder X-ray diffraction patterns of the exchange-coupled Fe_3Se_4:Fe_3O_4nanocomposites with three different ratios of soft and hard-phases. As can been seen from the figure, the characteristic peaks of both the hard-phase Fe_3Se_4 (JCPDS # 652315) and the soft-phase Fe_3O_4 (JCPDS # 790416) are present. No additional peaks (within the resolution of the XRD technique) due to any impurities or any secondary phase are observed.
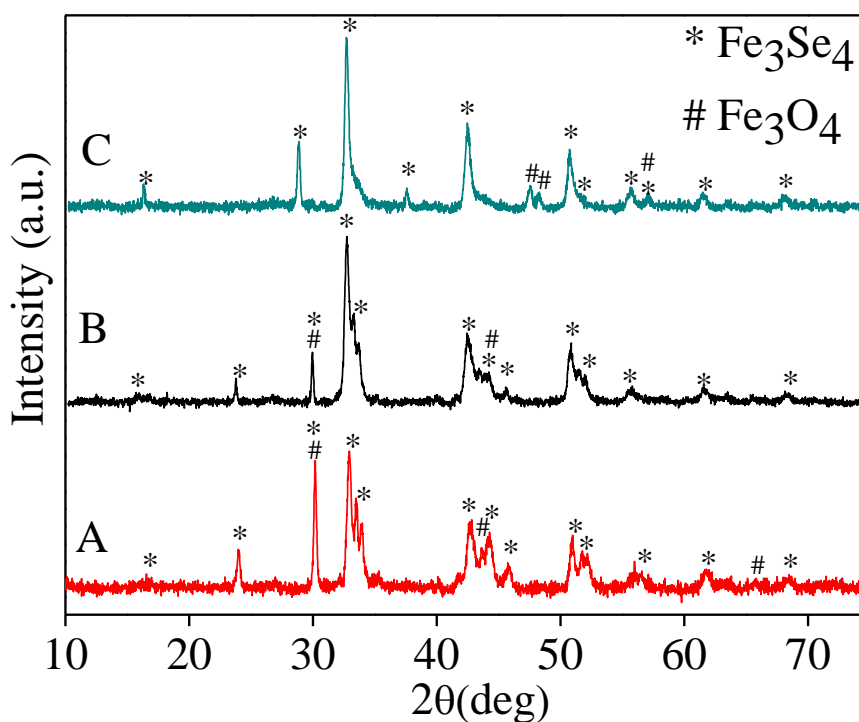
Figure 2.13: A comparison of X-ray diffraction patterns of as-prepared Fe_3O_4:Fe_3Se_4nanocomposites with varying weight proportions- A) F3, b) F5, and C) F10 respectively. The peaks corresponding to Fe_3O_4 (JCPDS 790416) are marked as (#) and Fe_3Se_4 (JCPDS 652315) are marked as (*). For the sake of brevity, we have not shown the 'assigned Miller indices' of the peaks.

2.3.2.2: Electron microscopy study:

The transmission electron micrographs of Fe_3O_4 nanoparticles (Figure 2.14) synthesized by the hot-colloidal method shows that particles are quasi-spherical and nearly monodispersed with particle diameter between 5-6 nm. Moreover, the image quality for magnetic particles is also affected due to the strong Lorentz interaction of electrons with the spins inside the particles. The diameter of the nanorods is in the range of 30-50 nm. Figure 2.15 shows the HRTEM image of the nanocomposite sample F5, the lattice fringes of Fe_3Se_4nanorods with inter-planar distance $d_{002} = 0.56$ nm is clearly visible.

Mousumi Sen
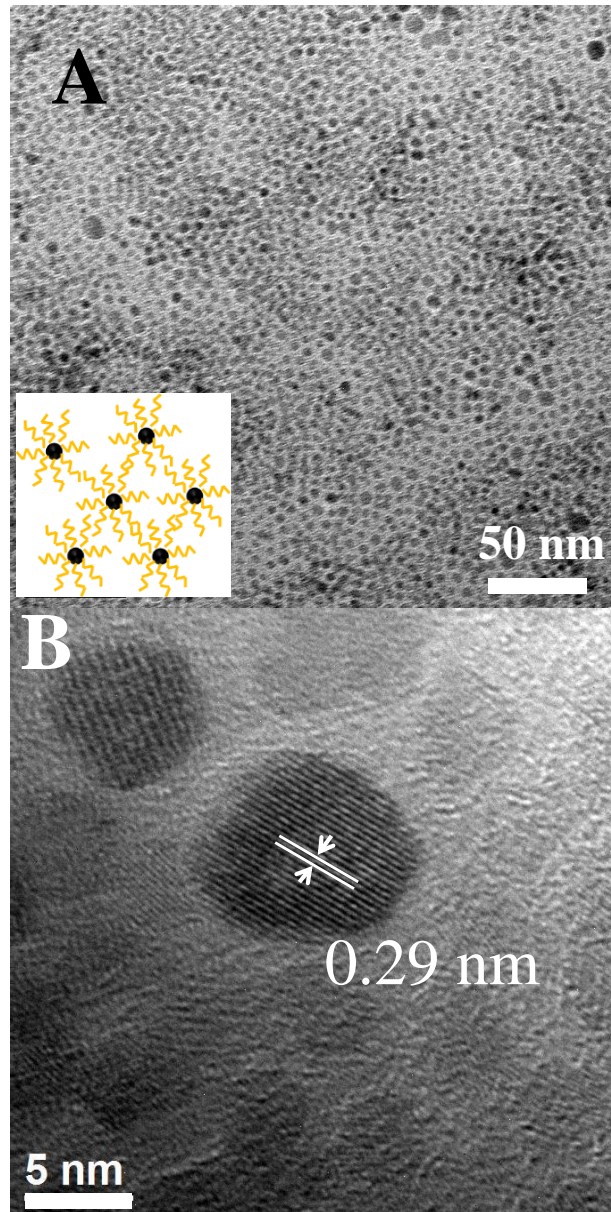
Figure 2.14: High-resolution transmission electron images of surfactant-capped Fe_3O_4 nanoparticles synthesized by the hot colloidal synthesis route. The lower panel shows lattice-fringes with d-spacing of 0.29 nm corresponding to 220 plane of Fe_3O_4.

The HRTEM image in the bottom panel lacks clarity due to distortion of electrons from the strong magnetic field of Fe_3Se_4nanorods.When a part of the nanocomposite was seen with greater magnification, small Fe_3O_4 nanoparticles were seen (red circles in figure 5D) on the surface of Fe_3Se_4nanorods.
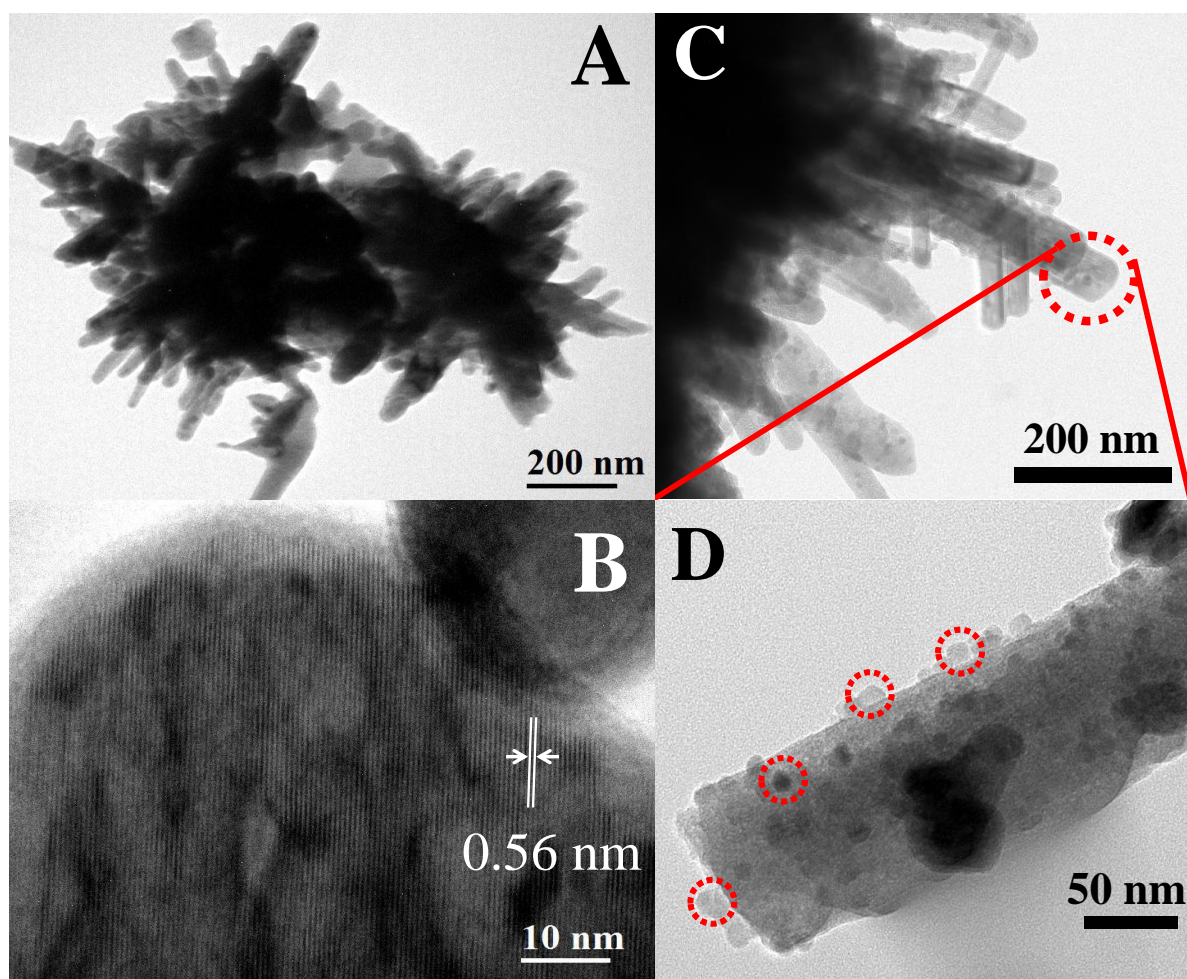
Figure 2.15: Representative high-resolution transmission electron micrographs of sample F5 (With 5% weight fraction of soft-phase in the Fe_3O_4:Fe_3Se_4 composite). (A)Shows highly aggregated Fe_3O_4:Fe_3Se_4 nanocomposite. (B) Shows the lattice-fringes with d-spacing of 0.56 nm corresponding to 002 plane of Fe_3Se_4. HRTEM image in the bottom

panel lacks clarity due to distortion of electrons from the magnetic field of Fe_3Se_4nanorods. (C) A high magnification image of the nanocomposite, the encircled area is zoomed in (D) where small Fe_3O_4 particles (red circles) can be seen on the surface of Fe_3Se_4 rods.

In Figure 2.16, scanning electron micrographs of the Fe_3Se_4: Fe_3O_4nanocomposites with 3.3% (A) 5% (B) and 10% (C) weight percentage of Fe_3O_4 are shown. All the samples show agglomeration. Nanocacti like morphology is observed with spikes growing out of the surface radially pointing in outward direction as observed in earlier studies[11]. The relative molar ratio of Fe, Se, and O in the nanocomposites was examined by energy dispersive spectrum (EDS) elemental analysis in a large scale of 200 μm. The top panel of Figure 2.17 shows the area of the sample where the scanning was done. The columns A, B and C show the distribution of elements Fe (blue), O (red) and Se (green) in sample F3.3, F5, and F10 respectively. The bottom panel shows the overlay for all the elements in the same scan area. The uniform distribution of all the elements throughout the scanning area shows that the composition of the nanocomposite is homogeneous throughout the sample.
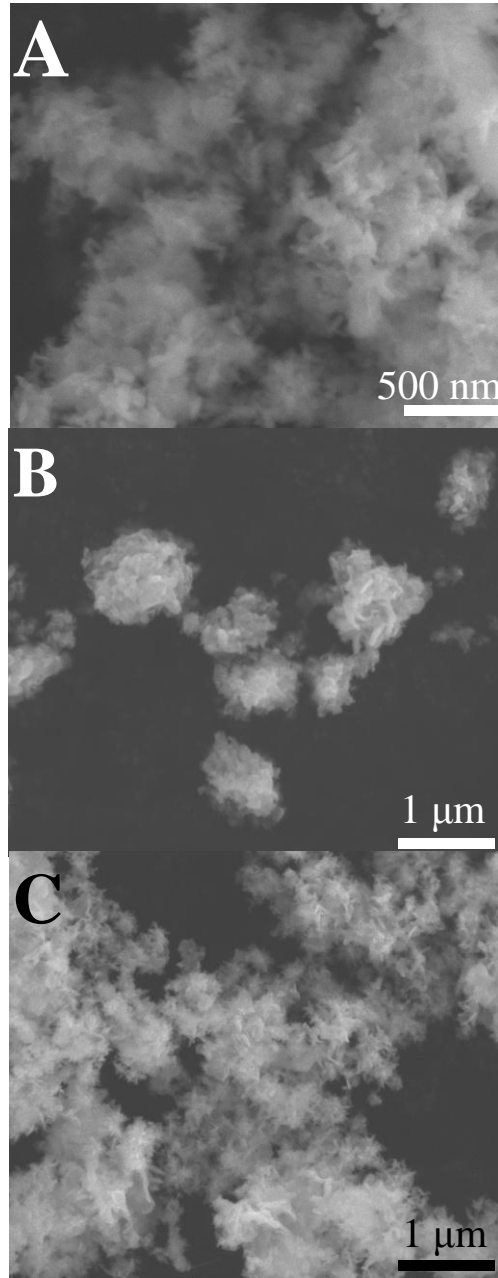
Figure 2.16: Scanning electron micrographs with (A) 3.3%, (B) 5%, and(C)10% weight fraction of Fe_3O_4 in Fe_3O_4:Fe_3Se_4nanocomposites.All the samples show agglomeration and nanocacti-like morphology with spikes at the surface, which point radially outwards.

Mousumi Sen
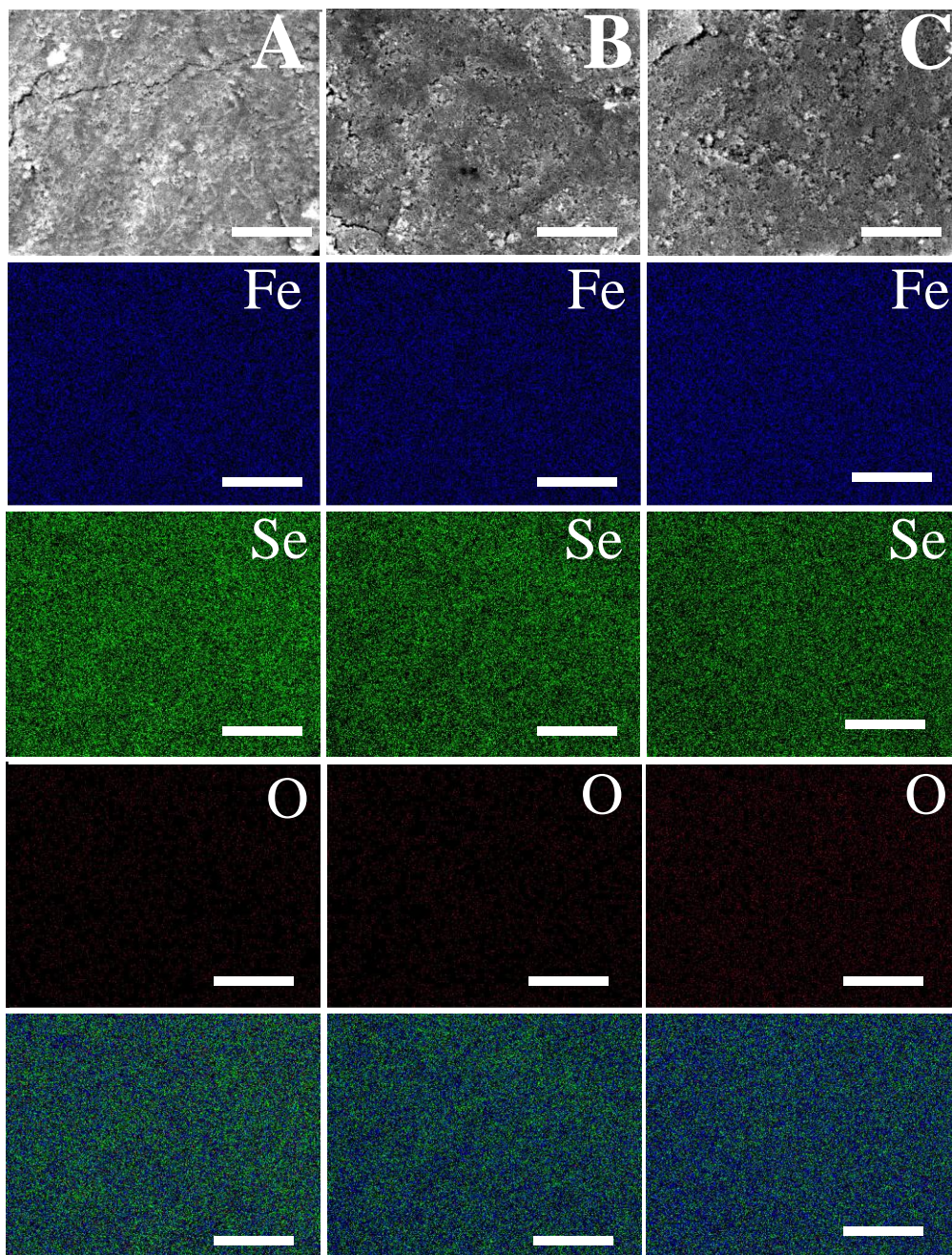
Figure 2.17: The images in columns A, B, and C represent the results corresponding to the samples F3.3, F5, F10 respectively. The images in topmost row show scanning electron micrographs (secondary electrons) of $Fe_3O_4:Fe_3Se_4$nanocomposites.. From second to fourth rows show the energy dispersive x-ray mapping for different elements from the area shown in the top row. From the elemental spectra analysis of the selected

region in all three samples, we can see that the distribution of Fe (Blue), Se (Green), and O (Red) is uniform throughout the samples. The bottom row shows the overlapped mapping of all the above elements. The scale bar for all the images in this figure is 200 μm.

2.3.2.3: Magnetic characterization

As discussed in the earlier sections, Fe_3Se_4 is ferrimagnetic at room temperature with Curie temperature ~317 K and it shows hard-magnetic properties [11]. After coupling Fe_3Se_4 with Fe_3O_4 under proper conditions, these systems behave as an exchange coupled magnet.
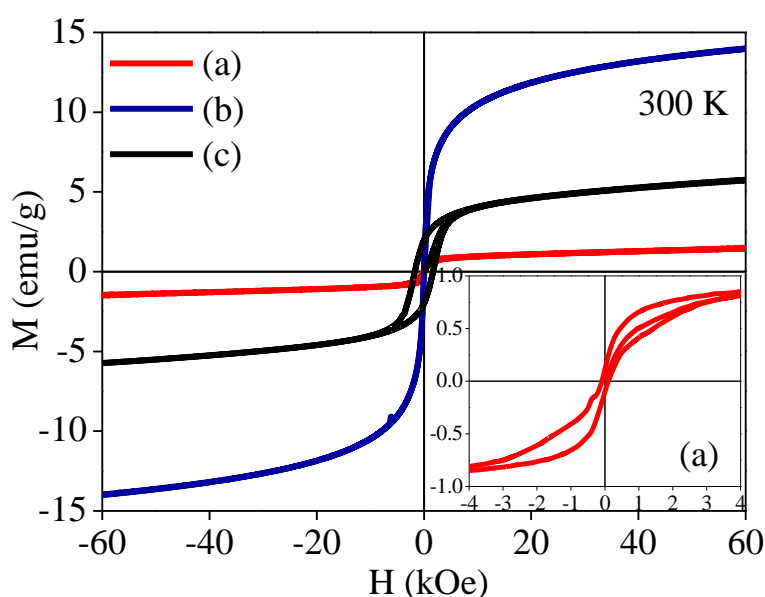
Figure 2.18: The comparison between room temperature (300 K) hysteresis loop of three Fe_3Se_4:Fe_3O_4nanocomposites (Fe_3O_4 is 5% by weight) prepared by three different methods (experimental section) showing the effect on the exchange interaction of the

Mousumi Sen

interfacial coupling of hard and soft magnetic nanoparticles. (a) pre-synthesized hard and soft nanoparticles are ground together in powder form and then subjected to heating in tube furnace at inert atmosphere at 300 °C. (b) Fe_3Se_4nanorods were synthesized in presence of Fe_3O_4 nanoparticles. (c) Both the hard and soft nanoparticles were taken and refluxed in organic solvent at 300 °C under inert atmosphere. The comparison clearly shows that the processing method greatly influence the interfacial physics.

In Figure 2.18, the hysteresis loop for Fe_3Se_4:Fe_3O_4 (Fe_3O_4 is 5% by weight) nanocomposites prepared by three different approaches (as described in the experimental section) are compared. All nanocomposite samples, prepared by three different approaches show ferrimagnetic character at room temperature. When we ground and heat the hard and soft-phase in powder form in tube furnace (approach "a"), the coercivity of the nanocomposite completely disappears and the M-H loop becomes more like superparamagnetic nanoparticles or soft magnet.

In approach "b" (Fe_3Se_4nanorods were synthesized in presence of pre-synthesized Fe_3O_4 nanoparticles), a step-like behavior was observed in the hysteresis curve (see inset of figure 2.18). In addition, the magnetization of the nanocomposite decreased significantly and near the origin the loop got pinched, *i.e.* the coercivity was sacrificed. Therefore both the above approaches did not produce desired results for an exchange spring magnet.

When the nanocomposites were prepared via approach "c" (both the hard and soft nanoparticles were taken and refluxed in organic solvent at 300 °C under inert atmosphere for one hour), all the samples show a single-phase behavior in magnetization hysteresis data even though the X-ray diffraction studies have shown the presence of two different crystallographic phases in the composites. No step like behaviors were observed in the

data and hysteresis loops change smoothly with the applied field exhibiting a good single-phase behavior of the nanocomposite (Figure 2.18). This indicates very good interfacial exchange coupling between the hard and soft-phases. It should be noted here that poor exchange coupling leads to observation of step-like features[19,23]. The capping of a nanoparticle by organic molecules in solution is a dynamic process and the organic molecules in the solution are in dynamic equilibrium with the capped molecules attached with the nanoparticle surface. When, the pre-synthesized nanoparticles were refluxed under nitrogen atmosphere at high temperature (300°C) in oleylamine the Fe_3Se_4 and Fe_3O_4 nanoparticles comes in close vicinity of each other's and the dynamic surface coating allows the small Fe_3O_4 nanoparticles to get attached to Fe_3Se_4 nanorods.

In top panel of Figure 2.19, the comparison between the magnetization versus magnetic field (M-H) curves at 300 K for five samples are shown including the as-synthesized Fe_3Se_4 nd Fe_3O_4 nanoparticles and Fe_3Se_4:Fe_3O_4 nanocomposites with three different ratios of soft and hard-phases. The magnetization curves do not saturate even at 8.5 T for any of the samples, which is primarily due to the ferrimagnetic properties, and the surface spins structures. The saturation magnetization was calculated by plotting M versus 1/H in high field region (above 60 kOe) and extrapolating the curve to y-axis to get M_s. The M_s value increases from 4.5 emu/g to 6.9 emu/g as the weight fraction of soft-phase is increased from zero to 10 % in the nanocomposite. Pure Fe_3Se_4 shows the highest value of coercivity (~2.27 kOe); which matches well with the previous reports[8,9,11]. To study the behavior at low temperature, the hysteresis data for all the samples were collected at 10 K. In contrast to the 300 K data the behaviors of these nanocomposites changes entirely (Figure 2.19 bottom panel). At 10 K, the Fe_3O_4 nanoparticle spins are blocked and therefore, smooth spring like behavior is not observed in the nanocomposites. When the direction of external field changes, the

change in the spins of soft-phase which are blocked gives step like features in the hysteresis loop.
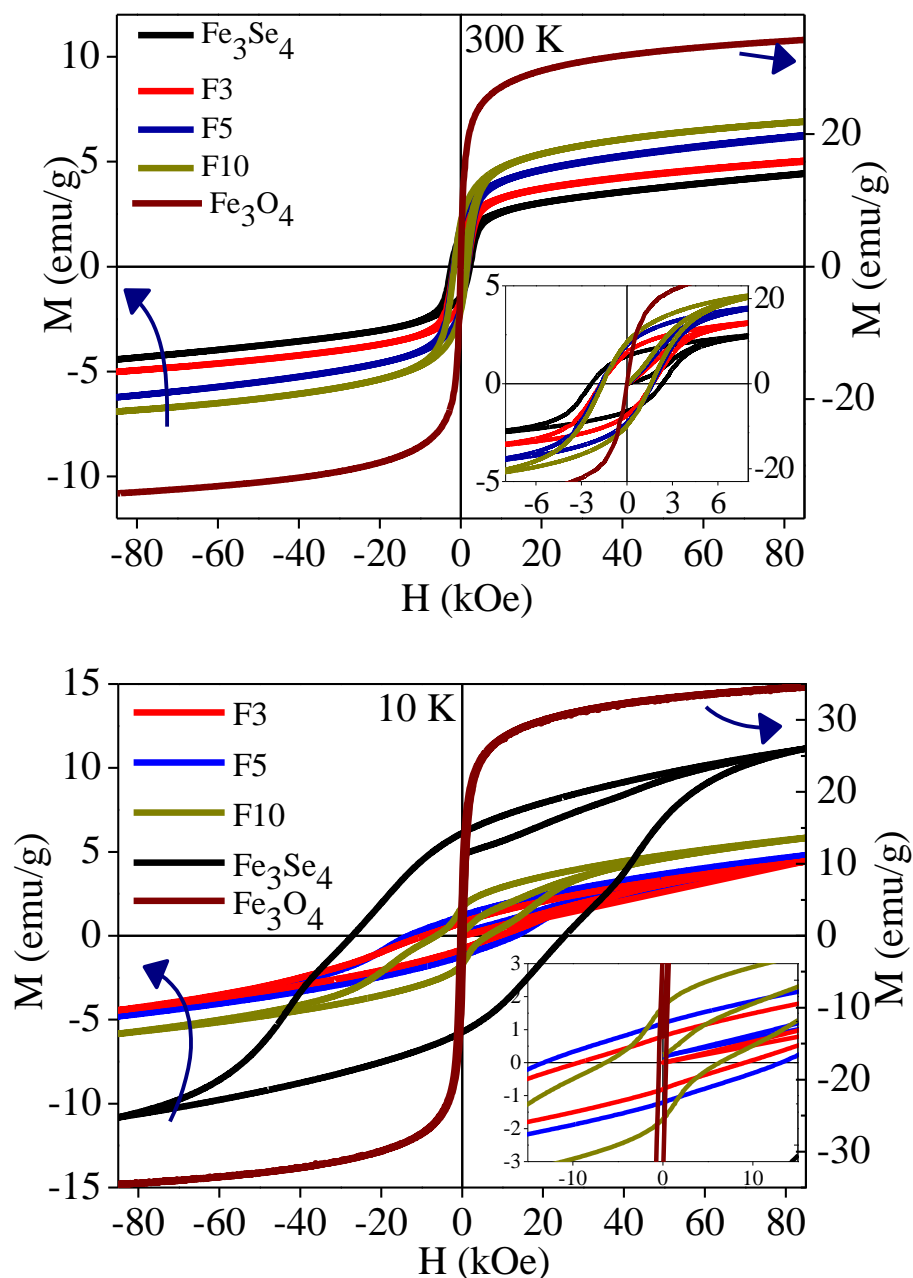
Figure 2.19: Comparison of M-H hysteresis loops recorded at 300 K for the samples F3.3 (3.3 % Fe_3O_4), F5 (5 % Fe_3O_4), F10 (10 % Fe_3O_4), as-synthesized Fe_3Se_4 nanorods and Fe_3O_4 nanoparticles. Saturation magnetization is found to increase monotonically as a function of increase in the weight fraction of soft-phase (Fe_3O_4 nanoparticles) in the

nanocomposites. The coercivity, on the other hand, shows a decrease with an increase in the weight fraction of the soft-phase (from F3.3 to F10).

In Figure 2.20, we have plotted the change in energy-product (BH_{max}), remanence magnetization (M_r), coercivity (H_c), and saturation magnetization (M_s) as a function of increasing weight % of Fe_3O_4 nanoparticles in Fe_3Se_4:Fe_3O_4nanocomposites. It is seen from Figure 9 and 10, that upon increasing the content of the soft magnetic phase, the saturation magnetization increases as expected as the M_s of Fe_3O_4 is much larger than Fe_3Se_4. In contrast, the coercivity value decreases with an increase in soft-phase content due to exchange spring coupling. The reason for this decrease in coercivity can be understood as follows. In an exchange spring system the 'soft-phase spins' at the interface are pinned to the hard-phase due to strong exchange interaction. As a function of distance from the interface, the chain of spins acts like a spring due to the gradual decrease in the interaction with distance. When the direction of the external magnetic field reverses, the soft-phase initiates the switching of the hard-phase, so the effective coercivity is realized at a lower value. It is noticeable that this solution based method adopted by us to design Fe_3Se_4:Fe_3O_4nanocomposites exchange spring magnet from the pre-synthesized nanoparticles proves out to be very efficient as with the inclusion of just 10 % soft-phase into the system enhances the energy-product by 116 % without showing a two-phase behavior as evident from the M-H loops (absence of step-like behavior). The magnetic properties of the hard-phase, soft-phase and nanocomposites are summed up in Table 2.2.
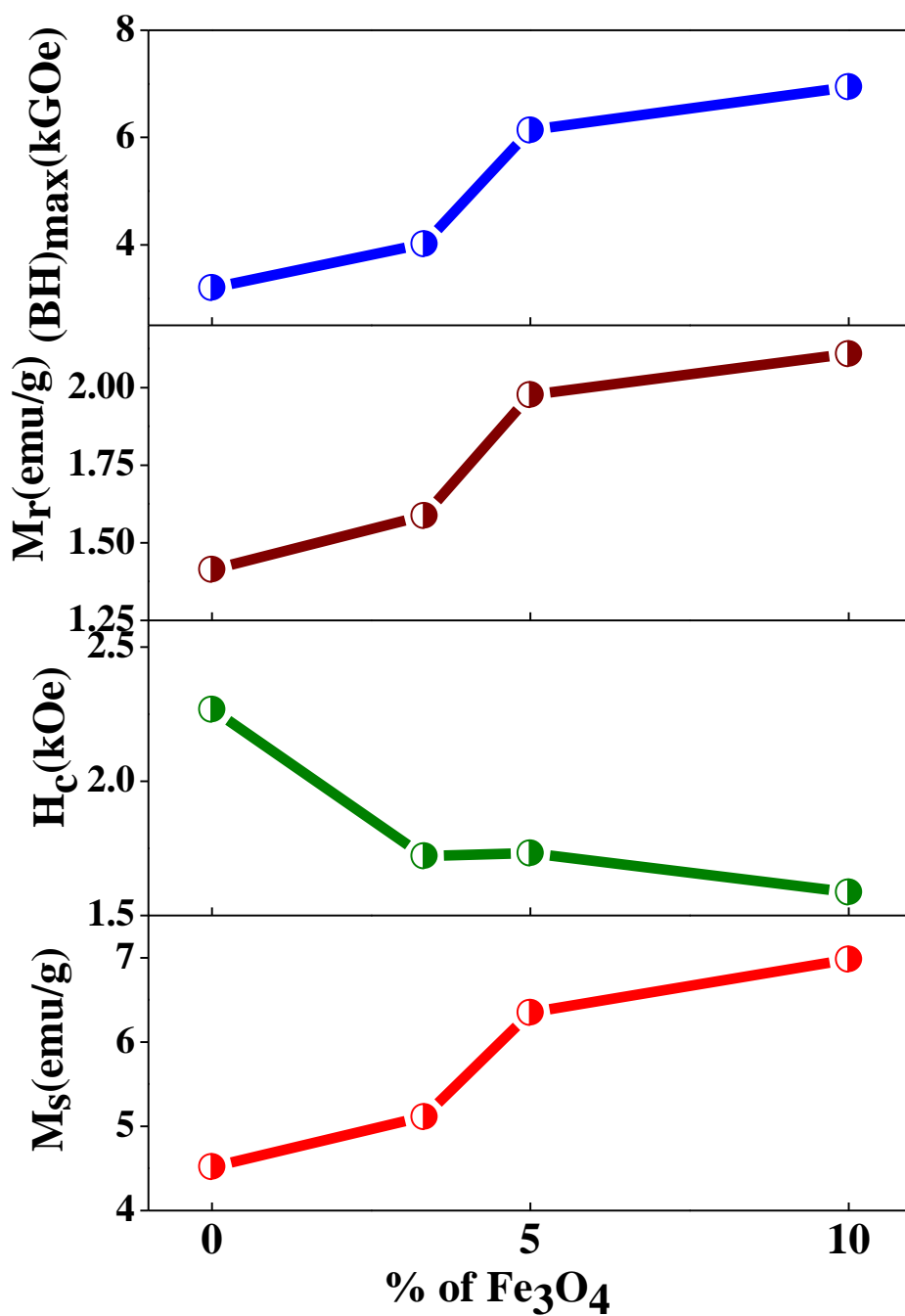
Figure 2.20: The graphs in various panels show changes in the calculated values of various magnetization parameters (at 300 K) of Fe_3O_4:Fe_3Se_4nanocomposites with varying weight fraction (x-axis) of soft-phase (Fe_3O_4 nanoparticles). The energy-product,

Mousumi Sen

remanent magnetization, and saturation magnetization values show an enhancement with an increase in the weight fraction of soft-phase in the composite whereas, the coercivity values show a reduction.

A comparison of zero field cooled (ZFC) and field cooled (FC) magnetization curves of nanocomposites with varying amount of at Fe_3O_4 fraction recorded at an external applied field of 100 Oe is shown in Figure 2.21. The Curie temperature of Fe_3Se_4 is around 317 K and the transition around 110 K can be attributed to blocking temperature (T_B) of Fe_3O_4 nanoparticles. No significant change in the Curie temperature of the nanocomposite is seen.
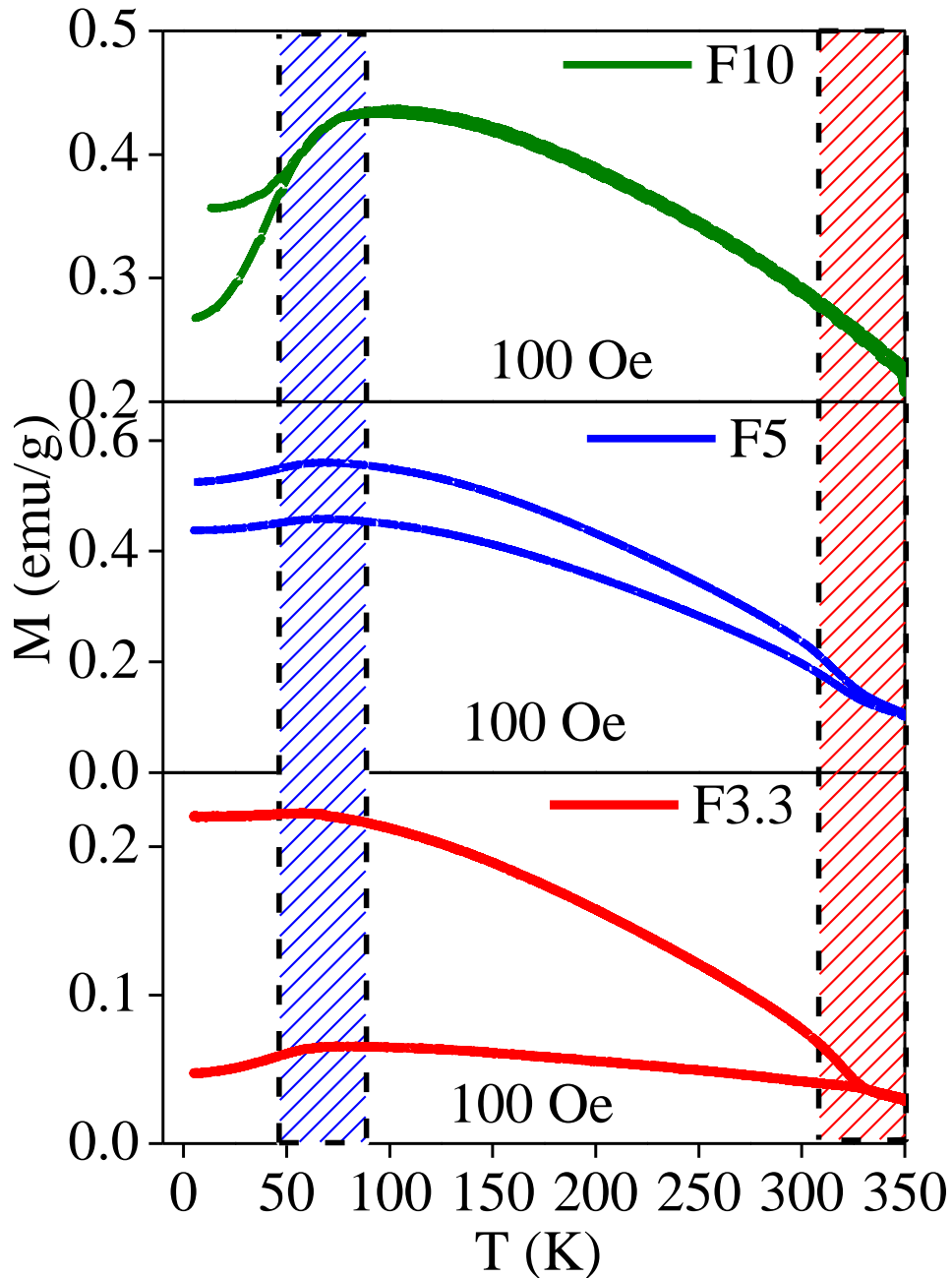
Figure 2.21: A comparison of ZFC- FC magnetization curves of Fe_3O_4:Fe_3Se_4 nanocomposite containing 5 % weight fraction of the soft-phase at an external applied field of 100 Oe. The Curie temperature of Fe_3Se_4 is around 323 K (seen by the bifurcation of ZFC-FC curves followed by a peak in ZFC magnetization) and the transition around 110 K can be attributed to blocking temperature of Fe_3O_4 nanoparticles.

AC magnetic susceptibility measurements of the soft-phase (Fe_3O_4) nanoparticles are done with small excitation amplitude 10 Oe from frequency 500 Hz to 9999 Hz (Figure 2.22). The data for both real and complex part of magnetization exhibit the expected behavior of superparamagnetic systems where the maxima shift marginally towards higher temperature with higher frequencies48. This also confirms the blocking nature of transitions of the soft-phase Fe_3O_4.
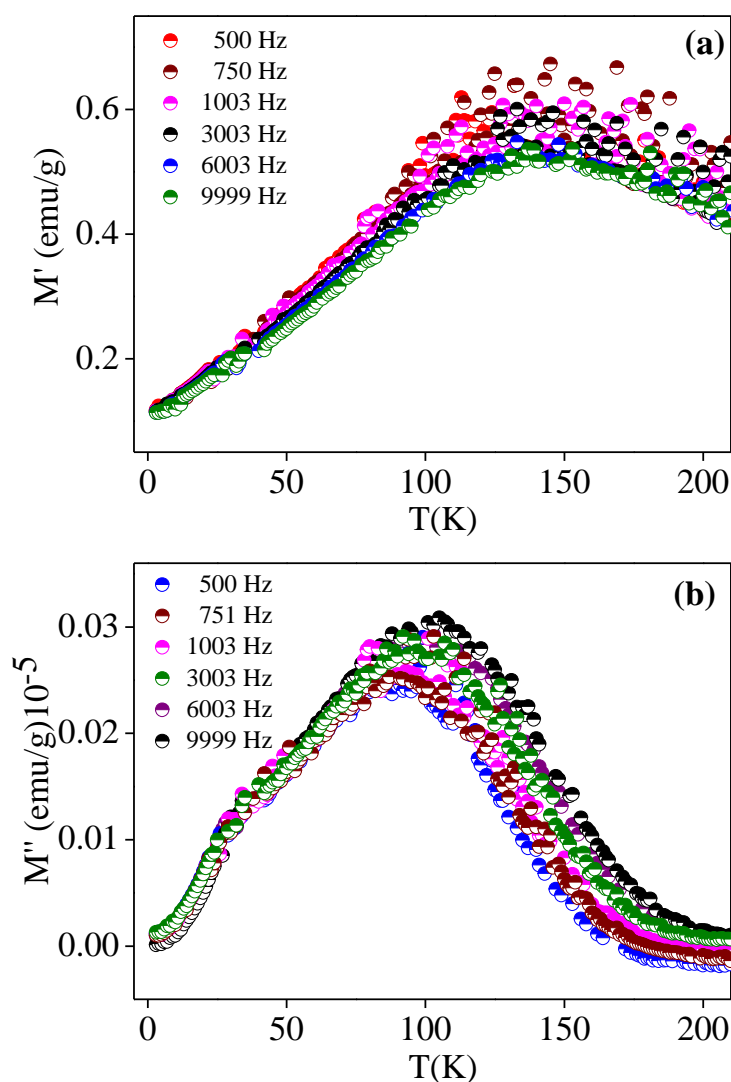
Figure 2.22: AC magnetic susceptibility measurements of the soft-phase (Fe_3O_4) nanoparticles are done with small excitation amplitude 10 Oe from frequency 500 Hz to 9999 Hz.

Mousumi Sen

Table2.2: Variations in the magnetic properties measured at 300 K as a function of change in the weight fraction of soft-phase in the Fe_3O_4-Fe_3Se_4 nanocomposites.

Sample (Weight fraction of Fe_3O_4 nanoparticles in Fe_3O_4-Fe_3Se_4 nanocomposite)	Coercivity (H_C) (kOe)	Saturation magnetization (M_S) (emu/g)	Remanence magnetization M_r (emu/g)	Energy-product (kGOe)
0 %	2.26	4.5	1.4	3.2
3.3 %	1.72	5.1	1.5	4.02
5 %	1.73	6.3	1.9	6.14
10 %	1.58	6.9	2.1	6.94
Fe_3O_4	0	35	0	--

Mousumi Sen

Section 2.4: Conclusion

Manganese doped iron selenide nanostructures in an attempt to increase the energy-product of the sample. The magnetization value increased from 4.84 to 7.54 emu/g, without any change in the Curie temperature; which is important for its application in hard-magnet. We could obtain more than 130% increase in the energy-product value in manganese doped iron selenide nanostructures. The reason for the decrease in coercivity and saturation magnetization in highly doped samples is not clear and is subject of further study with the help of neutron diffraction studies etc.

An exchange spring magnet based on Fe_3Se_4:Fe_3O_4 nanocomposite is demonstrated. . Bottom-up assemblage using pre-synthesized nanoparticles gives us precise control over the dimension of the hard and the soft-phase. This solution phase method provides flexibility in deciding the required dimension for the constituent hard and soft-phases, and represents a possible solution for dropping or eliminating the expensive rare earth elements that are often crucial in the development of permanent magnetic materials. The magnetic properties were studied with the amount of soft-phase present in the composite and the magnetic parameters were found to be enhanced monotonically with increased volume of soft-phase in the nanocomposite. The precise control over the interface and proper tuning of the hard and soft-phases is subject to more vigorous research in this area.

Mousumi Sen

References:

(1)   Cullity, B. D.; Graham, C. D. *Introduction to Magnetic Materials*; John Wiley & Sons, Inc.: Hoboken, NJ, USA, 2008; Vol. 53.

(2)   Coey, J. M. D. Hard Magnetic Materials: A Perspective. *IEEE Trans. Magn.* **2011**, *47* (12), 4671–4681.

(3)   Kirchmayr, H. R. Permanent Magnets and Hard Magnetic Materials. *J. Phys. D. Appl. Phys.* **1996**, *29* (11), 2763–2778.

(4)   Kurmoo, M.; Kepert, C. J. Hard Magnets Based on Transition Metal Complexes with the Dicyanamide Anion, {N(CN)2}-,. *New J. Chem.* **1998**, *22* (12), 1515–1524.

(5)   Gutfleisch, O.; Lyubina, J.; Müller, K.-H.; Schultz, L. FePt Hard Magnets. *Adv. Eng. Mater.* **2005**, *7* (4), 208–212.

(6)   Kramer, M. J.; McCallum, R. W.; Anderson, I. A.; Constantinides, S. Prospects for Non-Rare Earth Permanent Magnets for Traction Motors and Generators. *JOM* **2012**, *64* (7), 752–763.

(7)   Kharel, P.; Shah, V. R.; Li, X. Z.; Zhang, W. Y.; Skomski, R.; Shield, J. E.; Sellmyer, D. J. Structural and Magnetic Properties of Pr-Alloyed MnBi Nanostructures. *J. Phys. D. Appl. Phys.* **2013**, *46* (9), 95003.

(8)   Zhang, H.; Long, G.; Li, D.; Sabirianov, R.; Zeng, H. Fe 3 Se 4 Nanostructures with Giant Coercivity Synthesized by Solution Chemistry. *Chem. Mater.* **2011**, *23* (16), 3769–3774.

(9)   Long, G.; Zhang, H.; Li, D.; Sabirianov, R.; Zhang, Z.; Zeng, H. Magnetic Anisotropy and Coercivity of Fe3Se4 Nanostructures. *Appl. Phys. Lett.* **2011**, *99* (20), 202103.

(10)   Andresen, a. F.; van Laar, B.; Kvamme, E.; Ohlson, R.; Shimizu, A. The Magnetic Structure of Fe3Se4. *Acta Chem. Scand.* **1970**, *24*, 2435–2439.

(11)   Sen Bishwas, M.; Das, R.; Poddar, P. Large Increase in the Energy Product of Fe3Se4 by Fe-Site Doping. *J. Phys. Chem. C* **2014**, *118* (8), 4016–4022.

(12)   Poddar, P.; Srikanth, H.; Morrison, S. A.; Carpenter, E. E. Inter-Particle Interactions and Magnetism in Manganese–zinc Ferrite Nanoparticles. *J. Magn. Magn. Mater.* **2005**, *288*, 443–451.

(13)   Poddar, P.; Srinath, S.; Gass, J.; Prasad, B. L. V.; Srikanth, H. Magnetic Transition and Large Magnetocaloric Effect Associated with Surface Spin Disorder in Co and

CocoreAgshell Nanoparticles. *J. Phys. Chem. C* **2007**, *111* (38), 14060–14066.

(14)   Gass, J.; Poddar, P.; Almand, J.; Srinath, S.; Srikanth, H. Superparamagnetic Polymer Nanocomposites with Uniform Fe3O 4 Nanoparticle Dispersions. *Adv. Funct. Mater.* **2006**, *16* (1), 71–75.

(15)   Srinath, S.; Poddar, P.; Das, R.; Sidhaye, D.; Prasad, B. L. V.; Gass, J.; Srikanth, H. Large Magnetocaloric Effect, Moment, and Coercivity Enhancement after Coating Ni Nanoparticles with Ag. *ChemPhysChem* **2014**, *15* (8), 1619–1623.

(16)   Kneller, E. F.; Hawig, R. The Exchange-Spring Magnet: A New Material Principle for Permanent Magnets. *IEEE Trans. Magn.* **1991**, *27* (4), 3588–3560.

(17)   Jiang, J. S.; Fullerton, E. E.; Grimsditch, M.; Sowers, C. H.; Bader, S. D. Exchange-Spring Behavior in Epitaxial Hard/Soft Magnetic Bilayers. *7th Jt. MMM-Intermag Conf. Abstr. (Cat. No.98CH36275)* **1998**, *58* (18), 193–200.

(18)   Li, J.; Wang, Z. L.; Zeng, H.; Sun, S.; Liu, J. P. Interface Structures in FePt/Fe3Pt Hard-Soft Exchange-Coupled Magnetic Nanocomposites. *Appl. Phys. Lett.* **2003**, *82* (21), 3743–3745.

(19)   Roy, D.; Kumar, P. S. A. Enhancement of (BH)max in a Hard-Soft-Ferrite Nanocomposite Using Exchange Spring Mechanism. *J. Appl. Phys.* **2009**, *106* (7), 1–5.

(20)   Skomski, R.; Coey, J. M. D. Giant Energy Product in Nanostructured Two-Phase Magnets. *Phys. Rev. B* **1993**, *48* (21), 15812–15816.

(21)   Jiang, J. S.; Pearson, J. E.; Liu, Z. Y.; Kabius, B.; Trasobares, S.; Miller, D. J.; Bader, S. D.; Lee, D. R.; Haskel, D.; Srajer, G.; et al. A New Approach for Improving Exchange-Spring Magnets. *J. Appl. Phys.* **2005**, *97* (10), 1–4.

(22)   Soares, J. M.; Galdino, V. B.; Conceição, O. L. a; Morales, M. a.; De Araújo, J. H.; MacHado, F. L. a. Critical Dimension for Magnetic Exchange-Spring Coupled Core/shell CoFe 2O 4 / CoFe 2 Nanoparticles. *J. Magn. Magn. Mater.* **2013**, *326*, 81–84.

(23)   Zeng, H.; Li, J.; Liu, J. P.; Wang, Z. L.; Sun, S. Exchange-Coupled Nanocomposite Magnets by Nanoparticle Self-Assembly. *Nature* **2002**, *420* (6914), 395–398.

(24)   Chen, Q.; Ma, B. M.; Lu, B.; Huang, M. Q.; Laughlin, D. E. A Study on the Exchange Coupling of NdFeB-Type Nanocomposites Using Henkel Plots. *J. Appl. Phys.* **1999**, *85* (8, Part 2B), 5917–5919.

(25)   Zhang, Y.; Kramer, M. J.; Rong, C.; Liu, J. P. Microstructure and Intergranular Diffusion in Exchange-Coupled Sm-Co/Fe Nanocomposites. *Appl. Phys. Lett.*

2010, *97* (3).

(26)   Davies, J. E.; Hellwig, O.; Fullerton, E. E.; Jiang, J. S.; Bader, S. D.; Zimányi, G. T.; Liu, K. Anisotropy Dependence of Irreversible Switching in Fe/SmCo and FeNi/FePt Exchange Spring Magnet Films. *Appl. Phys. Lett.* **2005**, *86* (26), 1–3.

(27)   Poddar, P.; Fried, T.; Markovich, G. First-Order Metal-Insulator Transition and Spin-Polarized Tunneling in Fe3O4 Nanocrystals. *Phys. Rev. B* **2002**, *65* (17), 3–6.

(28)   Poddar, P.; Fried, T.; Markovich, G.; Sharoni, A.; Katz, D.; Wizansky, T.; Millo, O. Manifestation of the Verwey Transition in the Tunneling Spectra of Magnetite Nanocrystals. *Europhys. Lett.* **2003**, *64* (1), 98–103.

(29)   Poddar, P.; Telem-Shafir, T.; Fried, T.; Markovich, G. Dipolar Interactions in Two- and Three-Dimensional Magnetic Nanoparticle Arrays. *Phys. Rev. B* **2002**, *66* (6), 1–4.

(30)   Goya, G. F.; Berquó, T. S.; Fonseca, F. C.; Morales, M. P. Static and Dynamic Magnetic Properties of Spherical Magnetite Nanoparticles. *J. Appl. Phys.* **2003**, *94* (5), 3520.

(31)   Kleppe, A. K.; Jephcoat, A. P.; Smyth, J. R. Raman Spectroscopic Study of Hydrous γ -Mg 2 SiO 4 to 56.5 GPa. *Phys. Chem. Miner.* **2002**, *29* (7), 473–476.

(32)   Yang, X.; Dubrovinsky, L.; Manthilake, M. A. G. M.; Wei, Q. High-Pressure and High-Temperature Raman Spectroscopic Study of Hydrous Wadsleyite (β-Mg2SiO4). *Phys. Chem. Miner.* **2012**, *39* (1), 57–64.

(33)   Campos, C. E. M.; de Lima, J. C.; Grandi, T. a.; Machado, K. D.; Pizani, P. S. Structural Studies of Iron Selenides Prepared by Mechanical Alloying. *Solid State Commun.* **2002**, *123* (3–4), 179–184.

(34)   Campos, C. XRD, DSC, MS and RS Studies of Fe75Se25 Iron Selenide Prepared by Mechano-Synthesis. *J. Magn. Magn. Mater.* **2004**, *270* (1–2), 89–98.

(35)   Balamurugan, B.; Sellmyer, D. J.; Hadjipanayis, G. C.; Skomski, R. Prospects for Nanoparticle-Based Permanent Magnets. *Scr. Mater.* **2012**, *67* (6), 542–547.

(36)   Balamurugan, B.; Skomski, R.; Roy, D. Le; Hadjipanayis, G. C.; Shield, J. E.; Sellmyer, D. J. Cluster Synthesis, Direct Ordering and Alignment of Rare-Earth Transition- Metal Nanomagnets. In *Energy Technology 2012*; John Wiley & Sons, Inc.: Hoboken, NJ, USA, 2012; pp 382–390.

(37)   Balamurugan, B.; Skomski, R.; Li, X. Z.; Hadjipanayis, G. C.; Sellmyer, D. J. Magnetism of Directly Ordered Sm-Co Clusters. *J. Appl. Phys.* **2012**, *111* (7), 07B527.

(38)   Akdogan, N. G.; Hadjipanayis, G. C.; Sellmyer, D. J. Novel Nd 2 Fe 14 B Nanoflakes and Nanoparticles for the Development of High Energy Nanocomposite Magnets. *Nanotechnology* **2010**, *21* (29), 295705.

(39)   Wang, J.; Duan, H.; Lin, X.; Aguilar, V.; Mosqueda, A.; Zhao, G. Temperature Dependence of Magnetic Anisotropy Constant in Iron Chalcogenide Fe3Se4: Excellent Agreement with Theories. *J. Appl. Phys.* **2012**, *112* (10), 103905.

(40)   Zippel, J.; Lorenz, M.; Setzer, A.; Wagner, G.; Sobolev, N.; Esquinazi, P.; Grundmann, M. Defect-Induced Ferromagnetism in Undoped and Mn-Doped Zirconia Thin Films. *Phys. Rev. B* **2010**, *82* (12), 125209.

(41)   Joy, P. A.; Date, S. K. Comparison of the Zero-Field-Cooled Magnetization Behavior of Some Ferromagnetic and Ferrimagnetic Systems. *J. Magn. Magn. Mater.* **2000**, *218* (2), 229–237.

(42)   Joy, P. A.; Date, S. K. Unusual Magnetic Hysteresis Behavior of Oxide Spinel MnCo2O4. *J. Magn. Magn. Mater.* **2000**, *210* (1–3), 31–34.

(43)   Sun, S.; Zeng, H.; Robinson, D. B.; Raoux, S.; Rice, P. M.; Wang, S. X.; Li, G. Monodisperse MFe 2 O 4 (M = Fe, Co, Mn) Nanoparticles. *J. Am. Chem. Soc.* **2004**, *126* (1), 273–279.

Mousumi Sen

Chapter 3:

Study of thermal properties and magnetic entropy of Fe$_3$Se$_4$ nanoparticles

Mousumi Sen

Abstract

The magnetocaloric cooling technology based on magnetocaloric effect (MCE) is rapidly catching up as a potential alternative to gas based refrigeration technique as it is energy-efficient and environment-friendly. However, at present, very few materials exhibit MCE around room temperature or higher. In this chapter, the observation of MCE spanning a broad temperature range (~300 K to ~340 K) studied by a combination of external field (H) and temperature dependent magnetization (M) and heat capacity (C_p) measurements in Fe_3Se_4 nanorods (NRs) are discussed. The magnetic measurements of Fe_3Se_4 NRs show the characteristic bifurcation of M_{ZFC}, M_{FC} vs. T curves above its Curie temperature ($T_c \sim 317$ K) and a large coercivity of ~29 kOe at 10 K. The maximum in the isothermal magnetic entropy change (ΔS_M) is observed in the close proximity to the T_C. The ΔS_M and relative cooling power (RCP) showed linear dependence on H. RCP value of 12.45 J/kg was obtained for field change from 0 to 6 T. The results discussed here indicate that Fe_3Se_4 NRs holds a promise towards the development of a cheap, rare-earth-free, room-temperature magnetocaloric material.

Mousumi Sen

 Introduction:

3.1.1: Magnetocaloric effect

Magnetocaloric effect (MCE) is a magneto- thermodynamic phenomenon that has given birth to magnetic refrigeration, an environment-friendly and efficient energy conversion technology that enables cooling by exposing a magnetic material to an external magnetic field near its critical temperature. French physicist P. Weiss and Swiss physicist A. Piccard were first to observe MCE in nickel near its Curie temperature in the year 1917[1].

The alignment of spins along the external magnetic field direction leads to the decrease in the magnetic entropy of the system. When the magnetic field is applied adiabatically to the system, this decrease in magnetic entropy is compensated by increase in the crystal lattice entropy of the system, which in turn increases the system temperature. Although this method of refrigeration is not yet available in practical appliances in market, still magnetic refrigeration is gaining popularity among the research community across the globe specially in the niche areas such as space technology. Magnetic refrigeration offers several advantages over the conventional gas based compression systems including improved efficiency, freedom from ozone depleting gases.

The magnetocaloric cooling cycle consists of four thermodynamic steps (see figure 3.1)analogous to the Carnot refrigeration cycle. The steps are discussed below:

Adiabatic magnetization: The magnetic material is isolated from the environment. Magnetic field (+H) is applied to refrigerant material which results in increase in the refrigerant temperature as explained above.

Isomagnetic enthalpy transfer: This excess heat is then expelled to the surrounding by means of a fluid while maintaining the magnetic field constant so that reorientation of spins can be prevented.

Mousumi Sen

Adiabatic demagnetization: The magnetic field is removed(H=0) under adiabatic conditions. The magnetic entropy increases. To compensate this, the refrigerant material absorbs thermal energy from the crystal lattice lowering sample temperature.

Isomagnetic entropic transfer: The sample is then placed in thermal contact with the environment to be refrigerated. As the sample is cooler than the refrigerator environment, it absorbs heat from the environment. Then the cycle continues.

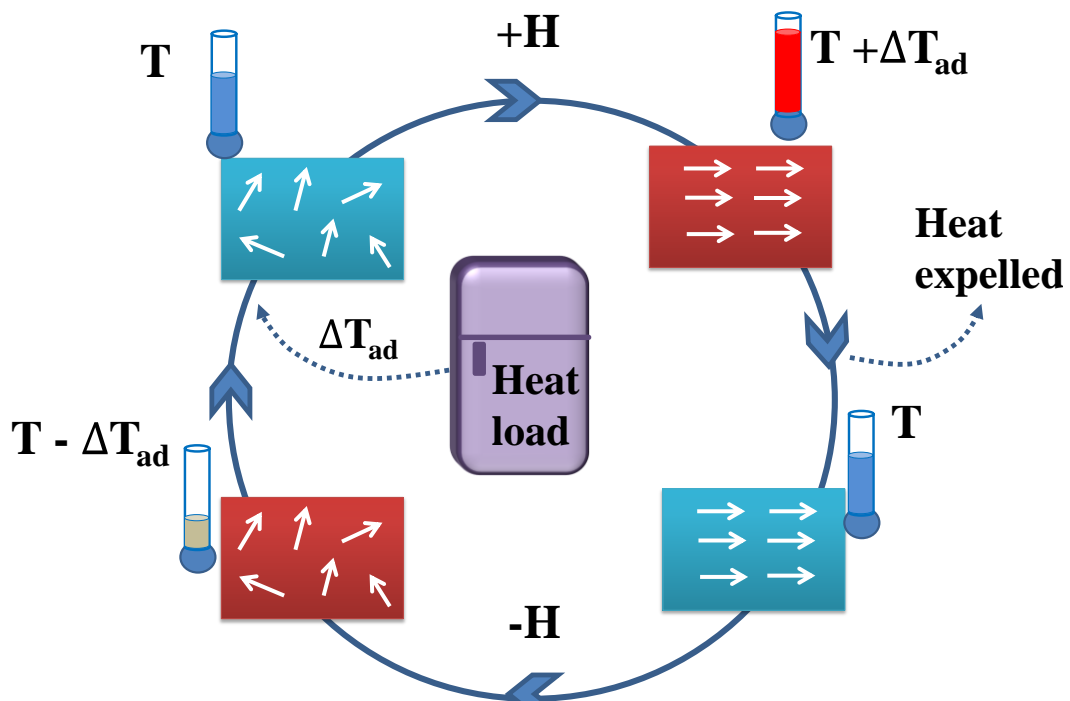**Figure 3.1**: Schematic to show the four thermodynamic steps of cooling by magneto-refrigeration.

3.1.2: Normal and inverse MCE

When the material heats up upon applying external magnetic field and cools down when field is removed, it is known as normal or conventional MCE. On the other hand, if the temperature derivative of the magnetization is positive, then the opposite effect occurs,

Mousumi Sen

i.e. the sample cools down when magnetic field is applied. Ni-Mn based Heusler alloys are perfect examples for showing inverse MCE[2,3]. The origin of inverse-MCE is associated with the antiparallel disorder of magnetic sublattices[4].The absolute amount of heat absorbed during the structural transition exceeds the heat release arising from the change of magnetic ordering, so the net temperature decreases on application of magnetic field[5].

3.1.3: Challenges in developing magnetocaloric materials:

Gadolinium and many of its alloys are considered as prototype magnetic refrigerant materials. After the discovery of giant magnetocaloric effect in $Gd_5(Si_2Ge_2)$ by Pecharsky *et al.*[6]there is a continuous hunt for newer and better materials which show good magnetocaloric effect near and above room temperature (RT).[6,7,8] Very few materials are available at present which show this effect above room temperature. Among the materials that exhibits MCE near RT, Gd metal, $Gd_5(Si_xGe_{1-x})_4$ alloys, MnAs[9], FeRh[6,9,10], and some manganites show good potential but, as indicated by Pecharsky *et al.*[11], it is not very logical to compare between different materials just by considering the isothermal entropy change (ΔS_M) value, as it is an extrinsic property and the adiabatic temperature change (ΔT_{ad}) is an intrinsic property of the system which depends on heat capacity of the materials. Most of the rare earth based materials perform best well below the room temperature. While, transition metal based compounds have an edge over these rare earth based compounds for use as room temperature refrigerants.[9,12]

The other challenge is associated with a narrow operating temperature range in which the change in magnetic entropy is large. This is due to the fact that the magnetic transitions, associated with the giant MCE are often very sharp and do not allow broader operating temperature window.

Mousumi Sen

Magnetic nanoparticles have added advantages of transition temperature tunability by varying the particle size and a larger surface area for better heat exchange. In addition, they can be assembled in the desired form e.g. thin film. Studies in superparamagnetic (SPM) ferrite nanoparticles show the maximum MCE near the blocking temperature (T_B) whereas in core-shell nanoparticles, large MCE has been assigned to the uncompensated surface spins.[13,14]

There lies a very close relationship between MCE and order-disorder transitions seen in magnetic materials. When we magnetize a paramagnetic solid sample near absolute zero or a ferromagnetic material near its spontaneous magnetic ordering temperature, the Curie temperature, T_C, in isothermal condition, it greatly reduces the disorder of a spin system, thus substantially lowering the magnetic part of the total entropy. It results in an increase of the lattice vibrations and the adiabatic temperature rise, ΔT_{ad}, which is an intensive (inherent to the material) thermodynamic quantity, also used to measure and express the MCE. Thus, the materials having ordering temperature near RT and a large $\left(\frac{\partial M}{\partial T}\right)_H$ value, associated with the transition, can be effectively used for applications related to the magnetocaloric refrigeration.

As seen in earlier chapters, Fe_3Se_4 is a ferrimagnetic compound with a monoclinic structure which orders below Curie temperature (~317 K). As Fe_3Se_4 has ordering temperature above its room temperature it has a potential as a room temperature refrigerant. Also, as no rare earth metal is involved in this material, so, this material can be a potential candidate in cheap, environment friendly rare earth free materials for room temperature magneto-refrigeration.

In this chapter, I have studied the magnetocaloric properties of Fe_3Se_4 nanorods by a combination of magnetization and heat capacity measurements.

3.2. Experimental details:

3.2.1. Measurement methods of magnetocaloric effect in Fe_3Se_4 nanoparticles:

Magnetocaloric effect can be measured in terms of either adiabatic temperature change ΔT_{ad} or isothermal change in magnetic entropy ΔS_M. The measurement can be either direct or indirect. In direct measurements, the initial and final temperature of the sample is measured directly on the magnetized and demagnetized sample for a particular value of external field. Direct measurements are very critical to perform and prone to error. The accuracy of measurement is compromised when the magnetic transitions are time dependent or when the change in magnetic field is away from instantaneous.

In the year 1999, Pecharsky *et. al.* explained in an article about the indirect ways to measure magnetocaloric effects in a sample through magnetization measurements or/and heat capacity measurements[15]. Indirect techniques allow the calculation of both $\Delta T_{ad}(T)_{\Delta H}$ and $\Delta S_M(T)_{\Delta H}$ from the experimentally measured heat capacity as a function of temperature in magnetic fields H_I and H_F, and the calculation of $\Delta S_M(T)_{\Delta H}$ from the magnetization experimentally measured at a number of different temperatures as a function of H from H_I to H_F. The MCE can be characterized by the magnetic entropy change due to the application of a magnetic field H. In this study, we have taken the indirect measurement methods to characterize the magnetocaloric properties of Fe_3Se_4.

Magnetic measurements: Static magnetic property measurements of Fe_3Se_4 nanoparticles were performed using a Physical Property Measurement System (PPMS) from Quantum Design Inc. The details about this measurement are discussed in previous chapter under section 2.2.2.

Mousumi Sen

3.2.2. Heat capacity measurements: The temperature and magnetic field dependence of the heat capacity at constant pressure C_p was measured using the heat capacity option in PPMS by Quantum Design. Each measurement comprised of a heating and cooling cycle followed by fitting the heat response from the sample according to two-tau model.

The powder sample was pressed to form a pellet and then a very small amount of grease was used to make proper thermal contact between the pellet and the sample platform. Measurement of C_p was done in two sets depending on the type of grease suitable in that temperature ranges (Apiezon N Grease for 1.9 K- 300 K and Apiezon H Grease for 260 K to 380 K).
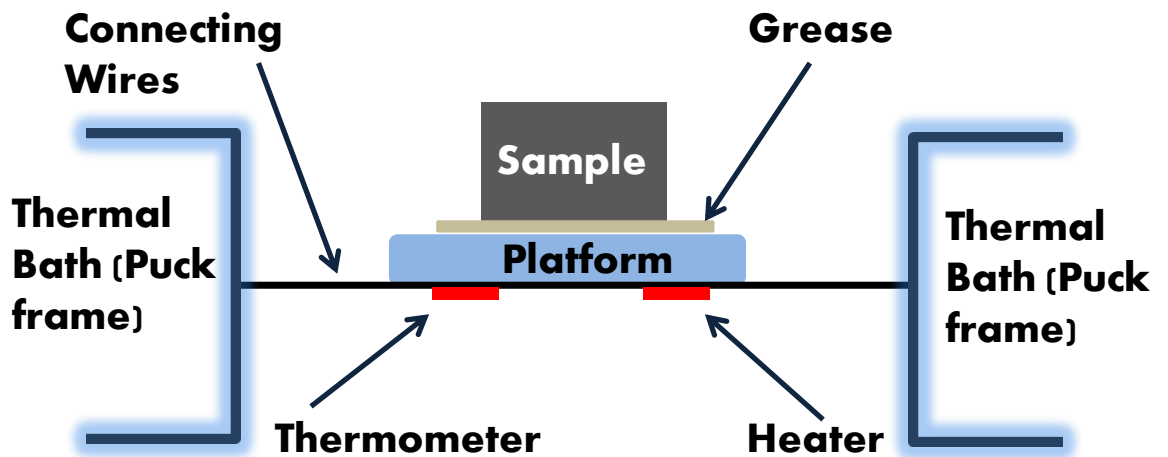
Figure 3.2: The placement of sample on the platform and connections inside the sample chamber for heat capacity measurement.

Figure 3.3: Sample puck for heat capacity measurements in PPMS[16] provided by Quantum Design *inc*.

3.3: Results and discussions:

3.3.1: Magnetism study:

Top panel of figure 3.4 shows the M_{ZFC} and M_{FC} vs. T curves of Fe_3Se_4 NRs at an external applied field of 100 Oe. The zoom view shows the bifurcation of both the curves below ~ 340 K, followed by a prominent peak in M_{ZFC} vs. T curve centered around ~ 317 K which is in close proximity to the Curie temperature (T_c) of Fe_3Se_4 NRs showing paramagnetic to ferrimagnetic transition.[17,18]As temperature decreases, the M_{FC} value increases rapidly as more and more moments align themselves in the presence of external field. The bottom panel of figure 3.4 reveals the hard magnetic nature of these samples as discussed in earlier reports[17,19,20].As we cool the sample from 300 K to 10 K, the coercivity H_C increases massively from 2.7 kOe (300 K) to 30 kOe (10) and loop appears almost

Mousumi Sen

squarish. Such high value of H_C is unusual for a compound not containing any rare earth or noble metal.
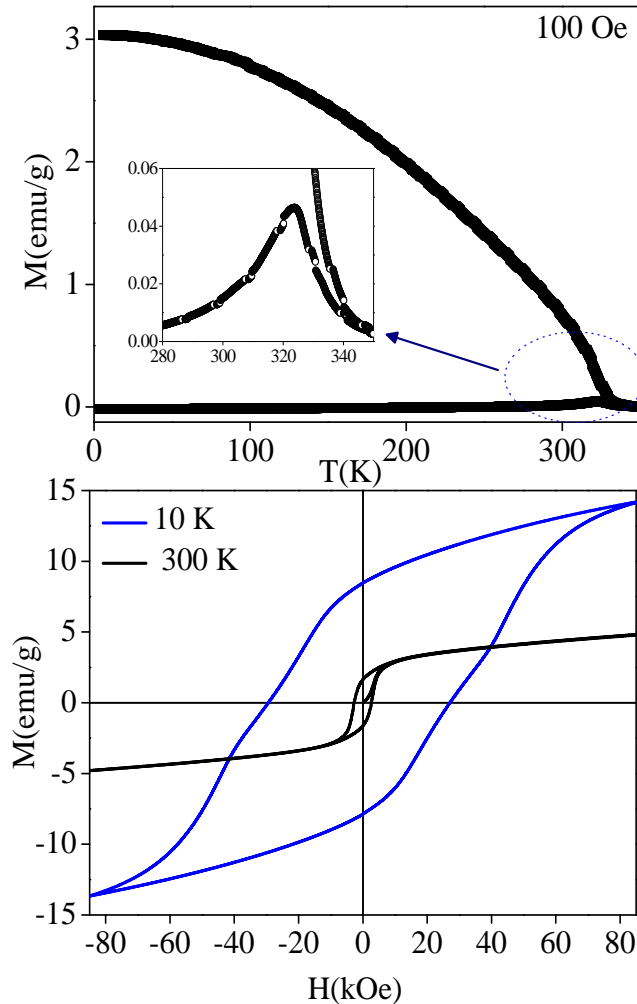
Figure 3.4: The top panel displays zero field cooled and field cooled magnetization vs. T curves (M_{ZFC}-T, M_{FC}-T) of as-synthesized Fe_3Se_4 nanoparticles at an external field ~100 Oe. The prominent peak at ~317 K in the inset can be ascribed to Curie transition. The bottom panel shows a comparison of magnetization versus field (M-H) hysteresis curves at 300 K and 10 K showing huge coercivity of ~29 kOe at 10 K.

We have chosen indirect measurements (isothermal magnetization measurements and heat capacity measurements) which is the most common method used to determine the MCE in

Mousumi Sen

most of the cases. The change in the magnetic entropy across any order-disorder transition can be obtained from the family of *M-H* curves (in first quadrant) at temperatures spanning the transition region according to the Maxwell's thermodynamic relation[15]

$$\left(\frac{\partial S}{\partial H}\right)_T = \left(\frac{\partial M}{\partial T}\right)_H$$

After integrating over the external magnetic field we get total entropy change as

$$\Delta S_M = \int_0^H \left(\frac{\partial M}{\partial T}\right)_{H'} dH' \qquad \qquad \dots\dots\dots\dots (1)$$

As, magnetization isotherms are measured as discrete temperature points, the equation (1) can be practically approximated as equation (2) where integral is substituted by numerical summation.

$$\Delta S_M = \sum_i \frac{M_i - M_{i+1}}{T_{i+1} - T_i} \qquad \qquad \dots\dots\dots\dots (2)$$

We have measured the magnetization isotherms in the first quadrant for Fe_3Se_4 nanoparticles over a field range of 0-9 T taken at intervals of 2 K from 301 to 341 K, which spans the region near the Curie transition, and, at an interval of 20 K in 220 to 300 K. After each measurement, the sample was heated over its Curie temperature to make the remanence from the previous measurement zero. Figure 3.5 shows the isothermal M-H curves measured in the above-mentioned temperature range. It can be seen from the figure that the magnetization does not saturate even at 9 T which is in consistent with earlier reports[17,18].This behaviour may come from the uncompensated surface spins at the surface of the particle. Figure 3.6 demonstrates M^2 vs. H/M isotherm curves near T_C, known as Arrott's plot. From the figure, it is clear that all H/M vs. M^2 curves show quasi-straight lines and the slopes are positive in high field range, which is the signature of a second-

Mousumi Sen

order or continuous phase transition.[21,22] Figure3.7shows the *M-T* curves at different magnetic field values extracted from the isothermal *M-H* curves presented in figure 2.
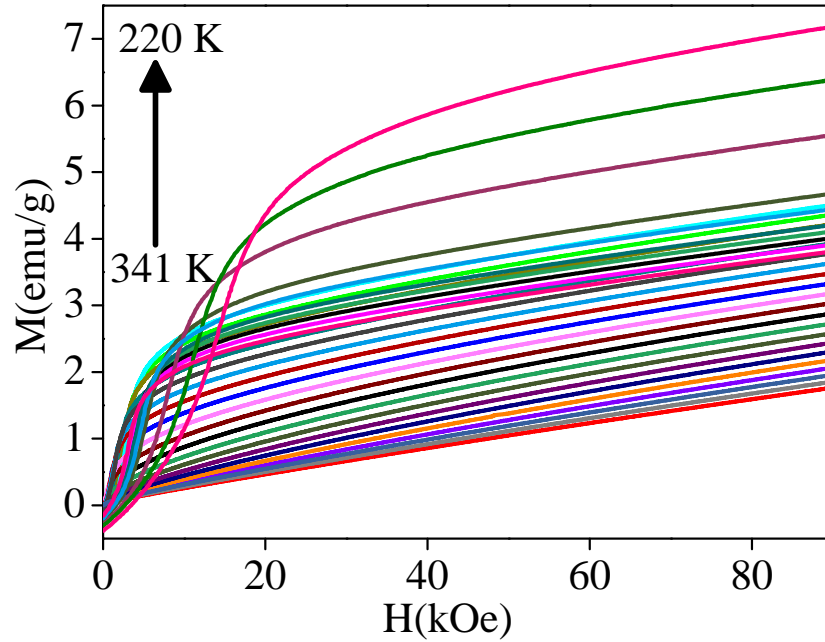

Figure 3.5. Magnetization isotherms in first quadrant of M-H loop recorded at two different sets of temperature range: from 341 K to 300 K (at an interval of 2 K) and from 300 to 220 K (at and interval of 20 K). Each measurement was taken after heating the sample over its Curie temperature.

Mousumi Sen
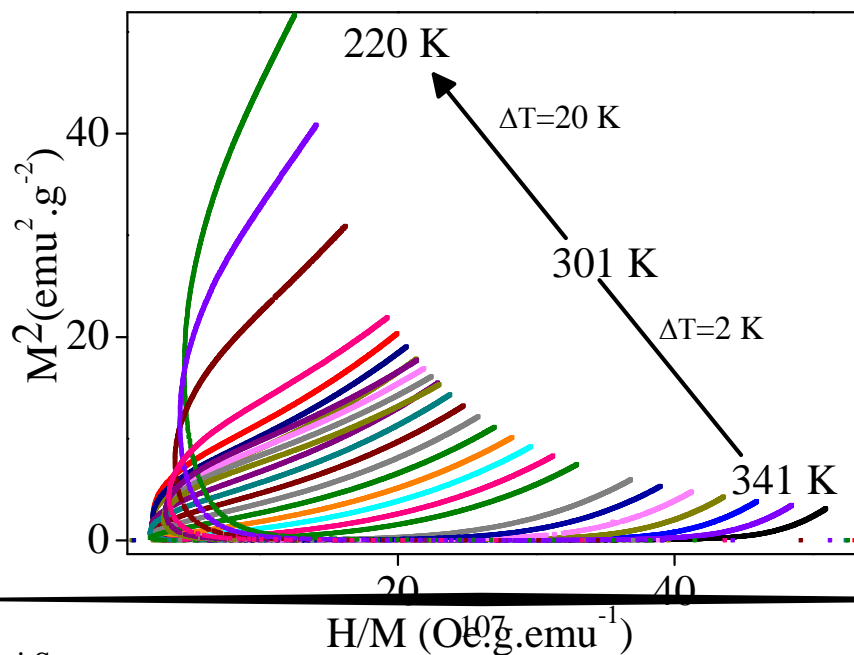
Figure 3.6: M^2 versus H/M plot (Arrott's plot) in the region near Curie temperature for Fe$_3$Se$_4$ nanoparticles showing positive slopes at higher field value characteristic of second order transition from paramagnetic to ferrimagnetic phase.
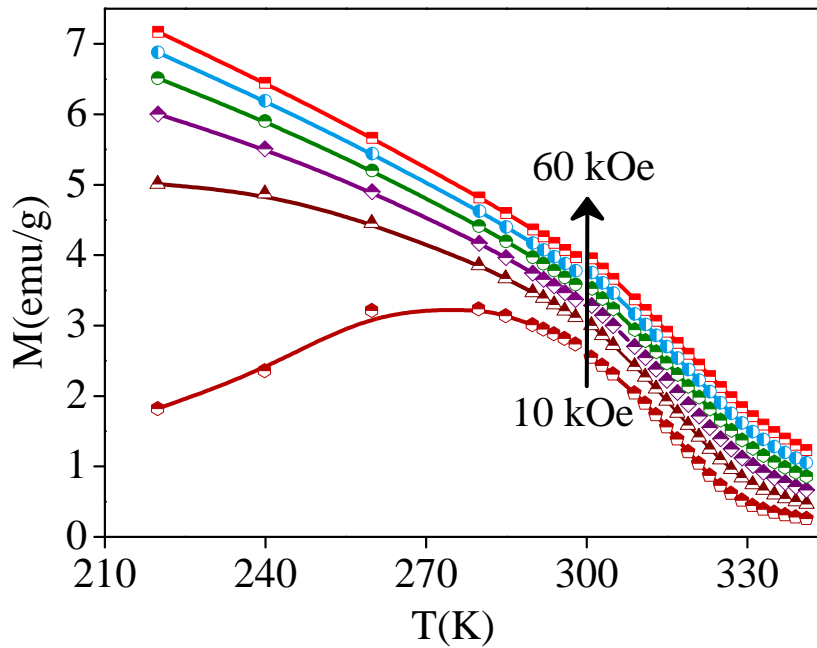
Figure 3.7: Magnetization versus temperature curves (extracted from the magnetization vs. magnetic field isotherms shown in Figure 2) for external field values from 10 kOe - 60 k Oe. Below the Curie temperature (~ 317 K), magnetization values increase rapidly with decreasing temperature.

The magnetic entropy change (ΔS_M) was calculated according to equation (1) from the field and temperature dependent magnetization data. In figure 3.8 we can see the variation in ΔS_M with T when the external field was varied from 0 to 1, 2, 3, 4, 5, and 6 T respectively. As it is evident from the figure,$\Delta S_M$is negative for Fe$_3$Se$_4$ NRs, i.e. the sample heats up while external field is applied and cools down when heat is removed. A prominent peak in the ΔS_M vs. T curve is observed around 317 K, which is in the close

Mousumi Sen

proximity to the T_C of the sample followed by the decrease in ΔS_M beyond T_C. The ΔS_M^{max} of $- 46 \times 10^{-2}$ J/kg-K was obtained at 317 K when the field was changed from 0 to 6 T.

Mousumi Sen
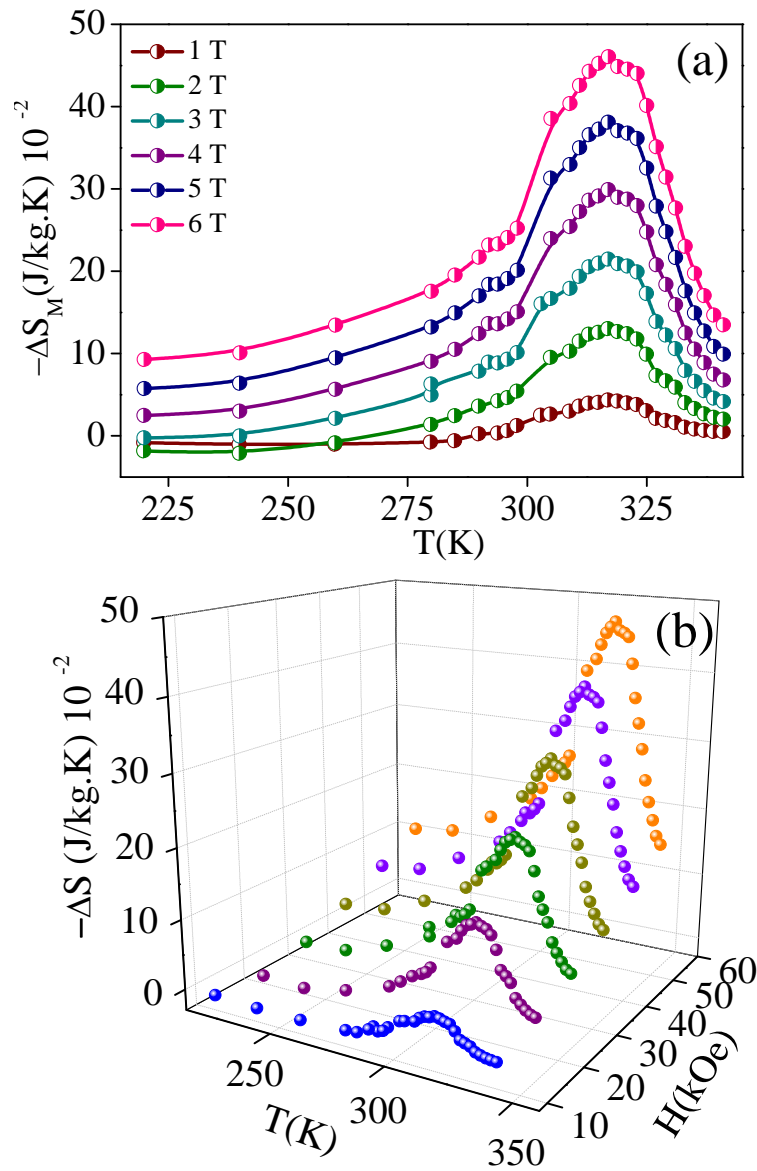
Figure 3.8. (a) Magnetic isothermal entropy change (ΔS_M) as a function of temperature is plotted when external field is switched from 0 to 10, 20, 30, 40, 50, and 60k Oe respectively.A peak in ΔS_M is observed around the Curie temperature for all the field values.(b) 3-dimensional graph showing the temperature and field dependence of magnetic isothermal entropy change.

Mousumi Sen

The ΔS_M^{max} values are more than two times higher than the maximum values reported for $CoFe_2O_4$ nanoparticles synthesized by solution chemistry[14,23]. Although the materials with second order phase transitions (SOT) usually tend to have a smaller ΔS_M^{max} value than materials with first order magnetic transition, but they have an advantage of showing a relatively broader range of operating temperatures (seen by large FWHM of the ΔS_M vs. T curve) and therefore these materials show better 'relative cooling power' (RCP) values, defined as below.[24,25]

$$RCP = \Delta S_M^{max} \times \delta_{FWHM} \quad\quad .....(2)$$

The δ_{FWHM} values were calculated by Gaussian fitting the peak observed in ΔS_M versus T curves. The external magnetic field dependence of RCP and ΔS_M^{max} is shown in figure 3.9. A linear dependence for both RCP and ΔS_M^{max} with H was found. The RCP value of 12.45 J/kg was obtained for field change from 0 to 6 T. Although the ΔS_M values are small, still a reasonable RCP value is obtained owing to the broad operating temperature range of this material.
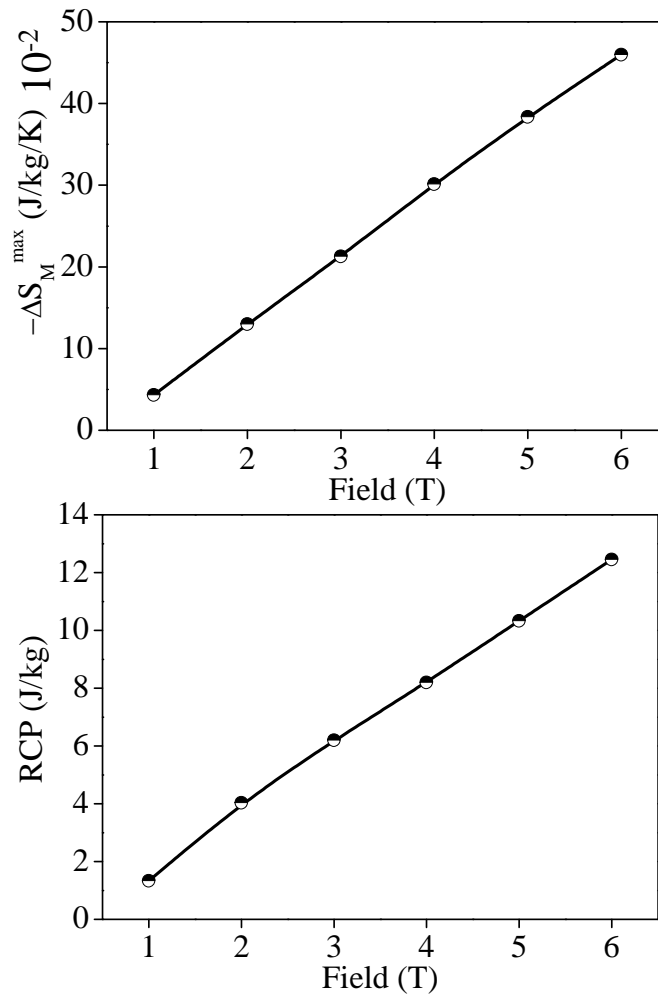
Figure 3.9. The top panel shows the external field (H) dependence isothermal entropy change and bottom panel show the field dependence of RCP. The linear dependence on H for both RCP and ΔS_M^{max} is found.

While designing the materials for magnetic cooling applications at room temperature, it is relevant to distinguish between the first order transitions and second order transitions to optimize the magnetic entropy change $\Delta S_M$and refrigerant capacity (RC).The maximum

Mousumi Sen

value of magnetic entropy change is obtained in compounds with first order magneto-structural transitions. But, the RC depends both on the height and width of ΔS_M curves. Optimization of RC makes SOT materials more suitable for practical applications.

Next, we investigated the presence of a universal behavior for the entropy change in materials with SOT which can be established by scaling the axes appropriately.[25,26] Then, all the curves collapse into a single curve independent of the external magnetic field. The universal curve was constructed by normalizing the ΔS_M to its peak value ΔS_M^{peak} and rescaling the temperature axis by defining a new parameter θ.

$$\theta = \begin{cases} -\dfrac{(T-T_C)}{(T_{R1}-T_C)}, T \leq T_C \\ \dfrac{(T-T_C)}{(T_{R2}-T_C)}, T > T_C \end{cases} \qquad \ldots\ldots\ldots\ldots\ldots\ldots\ldots(3)$$

Figure 3.10. The universal curve behavior of Fe_3Se_4 nanoparticles by scaling the temperature and isothermal entropy change value appropriately. Near T_c ($\theta=0$) all the curves merge into a single curve, far away from the T_c the dispersion in the curves can be observed.

Mousumi Sen

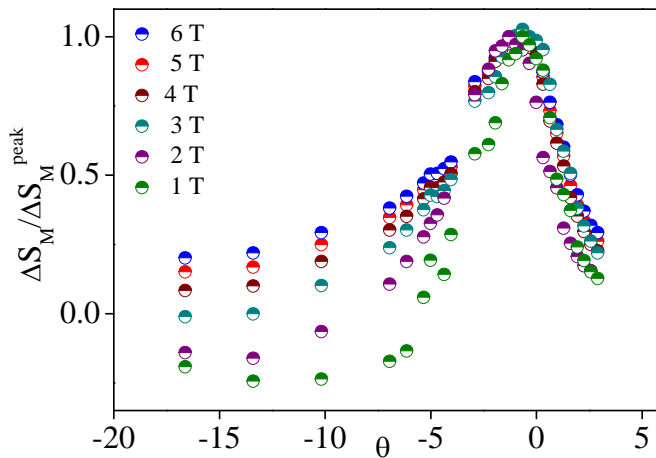Where, T_{R1} and T_{R2} are two reference temperature points that we have selected as temperatures corresponding to$\frac{1}{2}\Delta S_M^{Peak}$. The universal curve constructed according to these scaling is shown in figure 3.10. All the curves collapse into single curve in temperature regions near to Curie temperature ($\theta = 0$) validating that our treatment of data according to SOT in Fe$_3$Se$_4$. As we go far away from T$_c$ breakdown can be observed in the curve which is acceptable as scaling laws need not hold far away from T$_c$.

Although the formation of universal curve is a theoretical exercise, but these universal curves can also be used to characterize the magnetocaloric properties. Once the shape of the universal curve is known, the magnetic entropy value can be predicted for the larger values of magnetic fields which were not measured. Universal curve can also be used to make extrapolations of data in the temperature axis to ranges where the sample was notmeasured[27].

3.3.2: Heat capacity measurements:

Figures 3.11 and 3.12 show the temperature dependence of heat capacity for the as-synthesized Fe$_3$Se$_4$ NRs under zero field condition. A prominent λ- shaped anomalous peak is observed around 307 K (figure 3.11). Zero fieldC_p value for the as-synthesized Fe$_3$Se$_4$ NRs at 300 K is 30.61 J/mol/K. For bulk polycrystalline samples of Fe$_3$Se$_4$ a λ-transition is observed at 307 K in the C$_P$vs T curve and value of C$_p$ was found to be 31.61 J/mol/K at 300 K which is in good agreement with the results reported here[28,29]. The heat capacity in magnetic materials can be written as $C_p = \gamma T + \beta T^3 + \delta T^{3/2}$where the γT term gives the electronic contribution, βT^3gives the contribution from the lattice and, $\delta T^{3/2}$ gives the spin wave contribution. At low temperature, (2 K< T< 32 K) the experimental C$_p$ data is fitted according to the above equation and a good fit was observed (figure 10

Mousumi Sen

a).[30] For similar ferrimagnetic systems the plot of $C_pT^{-3/2}$ versus $T^{3/2}$ at low temperature range in zero field gives a straight line which is well in agreement with the experimental data obtained for Fe_3Se_4 NRs in this report (figure 3.13 b).[31] In presence of external magnetic field, the C_p values, as seen in the field dependent C_p vs. T curves remain almost unchanged. However, the anomalous λ-peak around T_c becomes flattened at higher fields and shifts marginally towards higher temperature, signifying that this peak is coupled to the magnetic transition (figure 3.14).[31,32]

Figure 3.11: The plots of (a) C_p versus T and (b) C_p/T versus T from 1.8 K to 300 K in
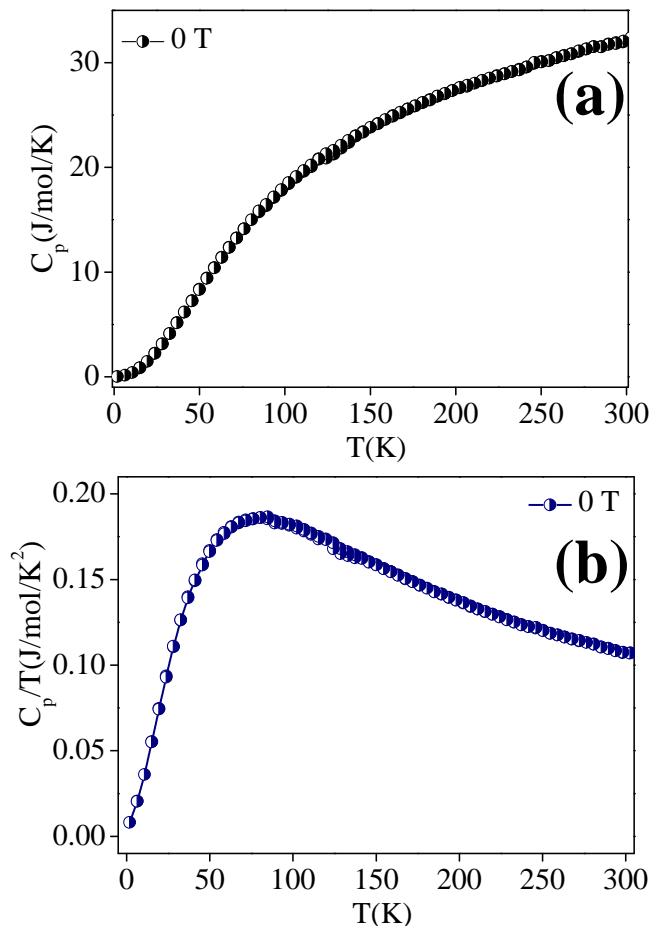
zero field condition are shown.

Mousumi Sen
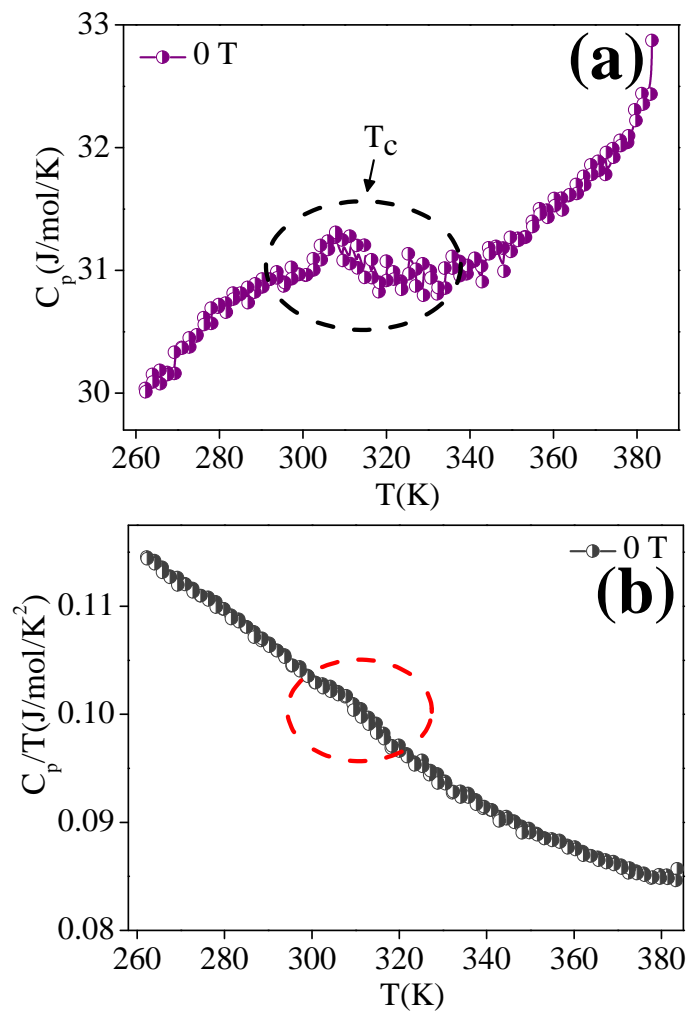
Figure 3.12: The plots of (a) C_p versus T and (b) C_p/T versus T from 260 K to 388 K in zero field condition are shown. The encircled region in both the plots shows the λ-anomaly around Curie transition.
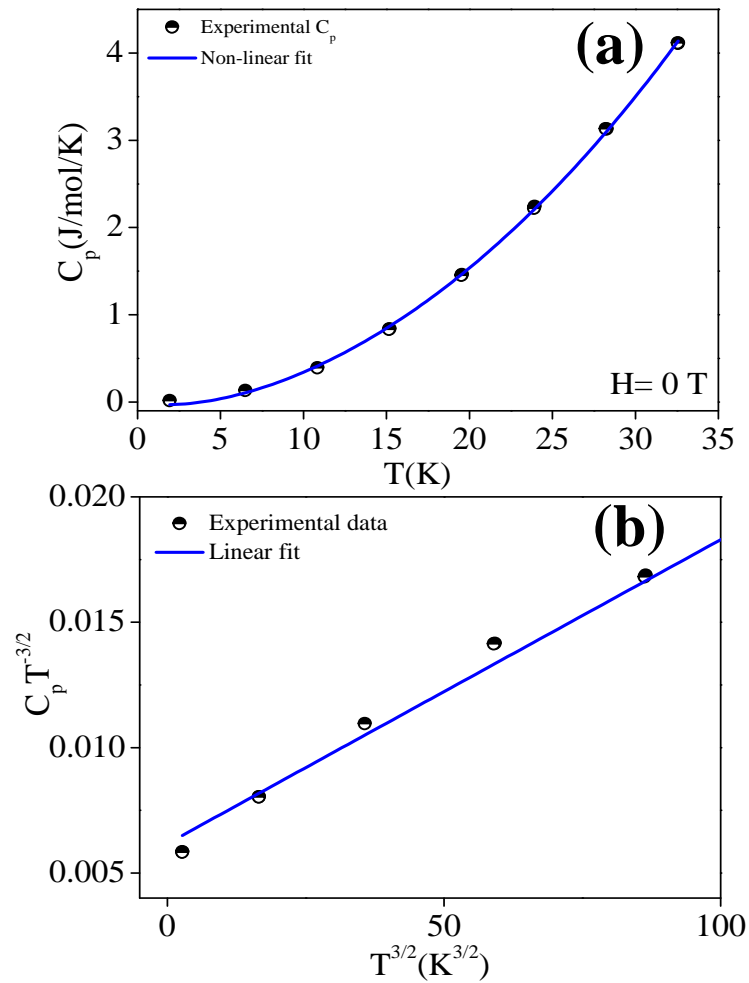
Figure 3.13: (a) Experimental C_p data is fitted according to the equation $C_p = \gamma T + \beta T^3 + \delta T^{3/2}$ at low temperature region in zero field condition. (b) plot of $C_p T^{-3/2}$ versus $T^{3/2}$ at low temperature range in zero field gives a straight line showing the presence of magnetic $T^{3/2}$ term in heat capacity data.

Mousumi Sen
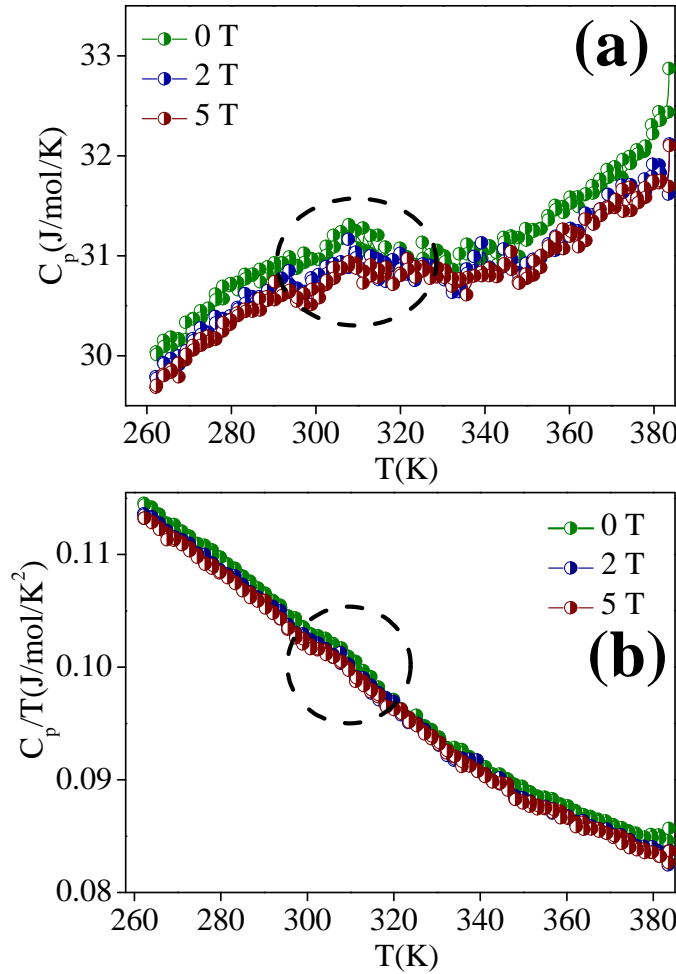
Figure 3.14: The plot of (a) C_p versus T and (b) C_p/T versus T from 260 K to 388 K shows the effect of external magnetic field on the heat capacity. The strong magnetic field suppresses and flattens the peak and also shifts marginally to higher temperature side characteristic for a magnetic transition.

The C_p values are used to calculate the adiabatic temperature change (ΔT_{ad}) associated with the paramagnetic to ferrimagnetic transition in Fe_3Se_4 NRs according to the equation given below:

$$\Delta T_{ad} = -\int_0^H \left(\frac{T}{C_p(T, H')}\right)\left(\frac{\partial M}{\partial T}\right)_{H'} dH' \quad \ldots\ldots\ldots\ldots (4)$$

Mousumi Sen

Then, under the assumption that magnetic field dependence of T/C_p (T, H')is much weaker than$\left(\frac{\partial M}{\partial T}\right)$,which is a quite decent approximation in the transition region, then the adiabatic temperature change can be written as[15,33]

$$\Delta T_{ad} \approx - \Delta S_M \left(\frac{T}{C_p(T, H')}\right) \dots \dots \dots \dots \dots \dots \dots . (5)$$
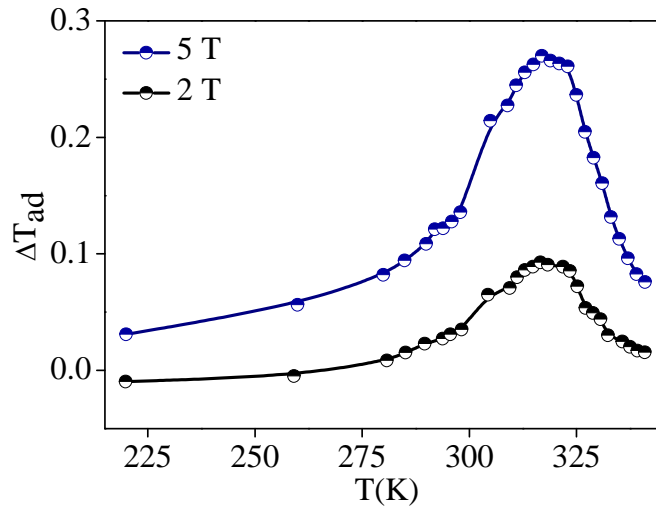
Figure 3.15: The plot of adiabatic temperature change with temperature calculated indirectly from magnetization and heat capacity measurements for two different field value 2 T and 5 T. ΔT_{ad} shows its maximum near room temperature which is near to its transition temperature is indicative of the potential of this material as room temperature magneto-refrigerant.

In figure 3.15, ΔT_{ad} is plotted with respect to temperature for two external field values and maximum value of ΔT_{ad} ~ 0.27 K is observed for ΔH of 5 T at ~ 317 K. As, we see that ΔT_{ad} shows its maximum near room temperature (figure 3.15) which is near to its

Mousumi Sen

transition temperature is indicative of the potential of this material in magnetocaloric refrigeration at room temperature.[34]

3.4: Conclusion:

The Fe_3Se_4 NRs, synthesized by one-pot high-temperature solution-phase method, are studied through magnetization and heat capacity measurements. Pronounced anomaly in the heat capacity that accompanies the magnetic phase transition at the Curie temperature $T_C \sim 317$ K was found. The heat capacity anomaly is flattened and shifted to higher temperatures by the application of a magnetic field and correlate well with the behavior of the anomalies in the magnetization. The adiabatic temperature change ΔT_{ad} was determined indirectly from heat capacity and magnetization measurements and a maximum of 0.27 K change in temperature is observed for a field change of 5 T at 317 K. These particles are found to have a broad range working temperature of ~ 30 K around room temperature which is highly beneficial from an applied perspective. In many earlier studies, it has been shown that with a very small amount of doping in Fe site the Curie temperature does not significantly change but the magnetization parameters can vary widely [17]. Research is under process in this direction to increase the ΔS_M^{max} values without compromising on the working temperature range.

Mousumi Sen

References:

(1)   Smith, A. Who Discovered the Magnetocaloric Effect? *Eur. Phys. J. H***2013**, *38* (4), 507–517.

(2)   Pal, D.; Ghosh, a.; Mandal, K. Large Inverse Magnetocaloric Effect and Magnetoresistance in Nickel Rich Ni52Mn34Sn14 Heusler Alloy. *J. Magn. Magn. Mater.***2014**, *360*, 183–187.

(3)   Krenke, T.; Acet, M.; Wassermann, E. F.; Moya, X.; Mañosa, L.; Planes, A. Martensitic Transitions and the Nature of Ferromagnetism in the Austenitic and Martensitic States of Ni-Mn-Sn Alloys. *Phys. Rev. B - Condens. Matter Mater. Phys.***2005**, *72* (1), 1–9.

(4)   von Ranke, P. J.; de Oliveira, N. a; Alho, B. P.; Plaza, E. J. R.; de Sousa, V. S. R.; Caron, L.; Reis, M. S. Understanding the Inverse Magnetocaloric Effect in Antiferro- and Ferrimagnetic Arrangements. *J. Phys. Condens. Matter***2009**, *21* (5), 56004.

(5)   Liu, J.; Gottschall, T.; Skokov, K. P.; Moore, J. D.; Gutfleisch, O. Giant Magnetocaloric Effect Driven by Structural Transitions. *Nat. Mater.***2012**, *11* (7), 620–626.

(6)   Pecharsky, V. K.; Gschneidner, Jr., K. A. Giant Magnetocaloric Effect in Gd5(Si2Ge2). *Phys. Rev. Lett.***1997**, *78* (23), 4494–4497.

(7)   Rostamnejadi, a.; Venkatesan, M.; Kameli, P.; Salamati, H.; Coey, J. M. D. Magnetocaloric Effect in La0.67Sr0.33MnO3 Manganite above Room Temperature. *J. Magn. Magn. Mater.***2011**, *323* (16), 2214–2218.

(8)   Phan, M. H.; Yu, S. C. Review of the Magnetocaloric Effect in Manganite Materials. *J. Magn. Magn. Mater.***2007**, *308* (2), 325–340.

(9)   Gama, S.; Coelho, A. a.; De Campos, A.; Magnus, a.; Carvalho, G.; Gandra, F. C. G.; Von Ranke, P. J.; De Oliveira, N. a. Pressure-Induced Colossal Magnetocaloric Effect in MnAs. *Phys. Rev. Lett.***2004**, *93* (23), 3–6.

Mousumi Sen

(10)   Annaorazov, M. P.; Nikitin, S. a; Tyurin, a L.; Asatryan, K. a; Dovletov, a K. Anomalously High Entropy Change in FeRh Alloy. *J. Appl. Phys.***1996**, *79* (3), 1689–1695.

(11)   Pecharsky, V. K.; Gschneidner, K. a. Some Common Misconceptions Concerning Magnetic Refrigerant Materials. *J. Appl. Phys.***2001**, *90* (9), 4614–4622.

(12)   Tegus, O.; Brück, E.; Buschow, K. H. J.; de Boer, F. R. Transition-Metal-Based Magnetic Refrigerants for Room-Temperature Applications. *Nature***2002**, *415* (6868), 150–152.

(13)   Poddar, P.; Srinath, S.; Gass, J.; Prasad, B. L. V.; Srikanth, H. Magnetic Transition and Large Magnetocaloric Effect Associated with Surface Spin Disorder in Co and CocoreAgshell Nanoparticles. *J. Phys. Chem. C***2007**, *111* (38), 14060–14066.

(14)   Poddar, P.; Gass, J.; Rebar, D. J.; Srinath, S.; Srikanth, H.; Morrison, S. A.; Carpenter, E. E. Magnetocaloric Effect in Ferrite Nanoparticles. *J. Magn. Magn. Mater.***2006**, *307* (2), 227–231.

(15)   Pecharsky, V. K.; Gschneidner, K. A. Magnetocaloric Effect from Indirect Measurements: Magnetization and Heat Capacity. *J. Appl. Phys.***1999**, *86* (1), 565.

(16)   Quantum Design. Physical Property Measurement System, Heat Capacity Option User's Manual, 2004.

(17)   Sen Bishwas, M.; Das, R.; Poddar, P. Large Increase in the Energy Product of Fe 3 Se 4 by Fe-Site Doping. *J. Phys. Chem. C***2014**, *118* (8), 4016–4022.

(18)   Zhang, H.; Long, G.; Li, D.; Sabirianov, R.; Zeng, H. Fe 3 Se 4 Nanostructures with Giant Coercivity Synthesized by Solution Chemistry. *Chem. Mater.***2011**, *23* (16), 3769–3774.

(19)   Long, G.; Zhang, H.; Li, D.; Sabirianov, R.; Zhang, Z.; Zeng, H. Magnetic Anisotropy and Coercivity of Fe3Se4 Nanostructures. *Appl. Phys. Lett.***2011**, *99* (20), 202103.

(20)   Wang, J.; Duan, H.; Lin, X.; Aguilar, V.; Mosqueda, A.; Zhao, G. Temperature Dependence of Magnetic Anisotropy Constant in Iron Chalcogenide Fe3Se4:

Mousumi Sen

Excellent Agreement with Theories. *J. Appl. Phys.***2012**, *112* (10), 103905.

(21)   Arrott, A. Criterion for Ferromagnetism from Observations of Magnetic Isotherms. *Phys. Rev.***1957**, *108* (6), 1394–1396.

(22)   Arrott, A.; Noakes, J. E. Approximate Equation of State For Nickel Near Its Critical Temperature. *Phys. Rev. Lett.***1967**, *19* (14), 786–789.

(23)   Hariharan, S.; Gass, J. Superparamagnetism and Magneto-Caloric Effect (MCE) in Functional Magnetic Nanostructures. *Rev. Adv. Mater. Sci.***2005**, *10* (5), 398–402.

(24)   Fitta, M.; Bałanda, M.; Mihalik, M.; Pełka, R.; Pinkowicz, D.; Sieklucka, B.; Zentkova, M. Magnetocaloric Effect in M–pyrazole–[Nb(CN) 8] (M = Ni, Mn) Molecular Compounds. *J. Phys. Condens. Matter***2012**, *24* (50), 506002.

(25)   Franco, V.; Blázquez, J. S.; Conde, A. Field Dependence of the Magnetocaloric Effect in Materials with a Second Order Phase Transition: A Master Curve for the Magnetic Entropy Change. *Appl. Phys. Lett.***2006**, *89* (22), 222512.

(26)   Bonilla, C. M.; Bartolomé, F.; García, L. M.; Parra-Borderías, M.; Herrero-Albillos, J.; Franco, V. A New Criterion to Distinguish the Order of Magnetic Transitions by Means of Magnetic Measurements. *J. Appl. Phys.***2010**, *107* (9), 09E131.

(27)   Franco, V.; Blázquez, J. S.; Ingale, B.; Conde, a. The Magnetocaloric Effect and Magnetic Refrigeration Near Room Temperature: Materials and Models. *Annu. Rev. Mater. Res.***2012**, *42* (1), 305–342.

(28)   Svendsen, S. R.; Åkesson, G.; Krogh-Moe, J.; Songstad, J.; Pilotti, Å. Decomposition Pressures and Standard Enthalpy of Formation for the Iron Selenides FeSe, Fe7Se8, Fe3Se4 and FeSe2. *Acta Chem. Scand.***1972**, *26*, 3757–3774.

(29)   Grønvold, F.; Westrum, Jr., E. F.; Stenhagen, E.; Andersson, G.; Stenhagen, E.; Palmstierna, H. Low Temperature Heat Capacities and Thermodynamic Properties of the Iron Selenides Fe1.04Se, Fe7Se8 and Fe3Se4 from 5 to 350 Degrees K. *Acta Chem. Scand.***1959**, *13*, 241–248.

Mousumi Sen

(30) Du, Y.; Cheng, Z. X.; Wang, X.; Dou, S. X. Structure, Magnetic, and Thermal Properties of Nd[sub 1−x]La[sub x]CrO[sub 3] (0≤x≤1.0). *J. Appl. Phys.***2010**, *108* (9), 93914.

(31) Tsurkan, V.; Mücksch, M.; Fritsch, V.; Hemberger, J.; Klemm, M.; Klimm, S.; Körner, S.; Krug von Nidda, H. -a.; Samusi, D.; Scheidt, E.-W.; et al. Magnetic, Heat Capacity, and Conductivity Studies of Ferrimagnetic MnCr2S4 Single Crystals. *Phys. Rev. B***2003**, *68* (13), 134434.

(32) Pecharsky, V. K.; Gschneidner, K. A.; Fort, D. Zero-Field and Magnetic-Field Low-Temperature Heat Capacity of Solid-State Electrotransport-Purified Erbium. *Phys. Rev. B***1993**, *47* (9), 5063–5071.

(33) Foldeaki, M.; Schnelle, W.; Gmelin, E.; Benard, P.; Koszegi, B.; Giguere, A.; Chahine, R.; Bose, T. K. Comparison of Magnetocaloric Properties from Magnetic and Thermal Measurements. *J. Appl. Phys.***1997**, *82* (1), 309.

(34) Sethulakshmi, N.; Al-Omari, I. a.; Suresh, K. G.; Anantharaman, M. R. Near Fifty Percent Sodium Substituted Lanthanum manganites—A Potential Magnetic Refrigerant for Room Temperature Applications. *Appl. Phys. Lett.***2014**, *104* (9), 92407.

Mousumi Sen

Chapter 4:

Is Fe$_3$Se$_4$ a room temperature multiferroic?

Mousumi Sen

Abstract

In this chapter, experimental evidences of the coexistence of magnetic and ferroelectric ordering and magnetoelectric coupling at room temperature in Fe_3Se_4 nanorods is discussed. The monoclinic iron selenide is known for its magnetic ordering but there is no report on its ferroelectric properties. We observed that Fe_3Se_4 nanorods show type-II multiferroicity, i.e. the ferroelectric and magnetic Curie temperature coincide and shows a coupling manifested by an anomaly in the dielectric constant and Raman shift at T_c. We do not completely understand the origin of the ferroelectric ordering at this point however the simultaneous presence of magnetic and ferroelectric ordering at room temperature in Fe_3Se_4 along with hard magnetic properties will open new research areas for memory and devices.

Mousumi Sen

4.1: Introduction:

4.1.1: Overview of multiferroics:

To achieve rich functionality in materials, one of the promising approaches is to combine different physical properties in one material. The materials combining more than one "ferroic" properties were called "multiferroics"[1,2]. The promising technical applications of these materials span large areas such as – energy-transformation, signal-generation and processing, information storage and many more. Multiferroicity provides substantial complexity that challenges our understanding of electrons in crystal, because of the huge diversity of materials with different structures and compositions where these properties are manifested. The physics of multiferroics is fascinating, involving crossovers of many sub-disciplines such as, symmetries, domains, hetero-structures, topology etc.[3]. Therefore, multiferroic materials have been in the limelight among researchers world-wide in last decade[4,5].

Based on the mechanisms, these materials can be classified in two broad classes explained below.

Type-I multiferroics are those materials where magnetism and ferroelectricity arises from independent mechanisms. Both, the time reversal and spatial reversal symmetries are broken in these systems. Generally, in type-I multiferroics, FE ordering temperature is much higher than magnetic ordering temperature.

Type-II multiferroics are those materials in which ferroelectricity occurs only in the magnetically ordered state. The ordering temperature for magnetism and ferroelectricity coincides for these types of compounds[6].

Mousumi Sen

Multiferroic compounds are full of surprises. Lately, there were reports of unconventional multiferroics where mechanisms for the origin of ferroelectricity were discussed in centro-symmetric materials based on charge-ordering and bond-ordering[5].

4.1.2: Proper and improper multiferroics:

In proper multiferroics, traditional ferroelectricity is observed. Most of these ferroelectrics are transition metal oxides (generally their structure is derivative of perovskite), where transition metal ions have empty d-orbitals[5]. The collective shift of positive and negative ions inside the crystal leads to bulk polarization in the materials.

Improper multiferroics, on the other hand, are a result of more complex lattice distortion where the origin of ferroelectricity is not the empty d-orbitals of transition metals. Improper multiferroics have drawn remarkable attention in past years due to the presence of strong coupling between magnetic and electrical ordering[7]. The mechanism of origin of ferroelectricity in improper multiferroics can be (a) charge ordering (b) spin ordering and (c) orbital ordering. $LuFe_2O_4$ is often discussed as a prototype where multiferroicity arises because of charge ordering. $LuFe_2O_4$ is a mixed valence material where an equal amount of Fe^{2+} and Fe^{3+} ions occupies the same lattice sites[8]. The charge frustration in the triangular lattice results in polar arrangements of electrons Fe^{3+} which in-turn gives rise to ferroelectricity in this compound. The famous Fe_3O_4, which shows the well-known Verwey transition (insulator-metal transition)[9] also exhibits ferroelectricity in the insulating state[7,10,11]. Fe_3O_4 has thus become the oldest known multiferroic to human kind. Below 38 K, ferroelectric switching was observed in magnetite thin films[12].
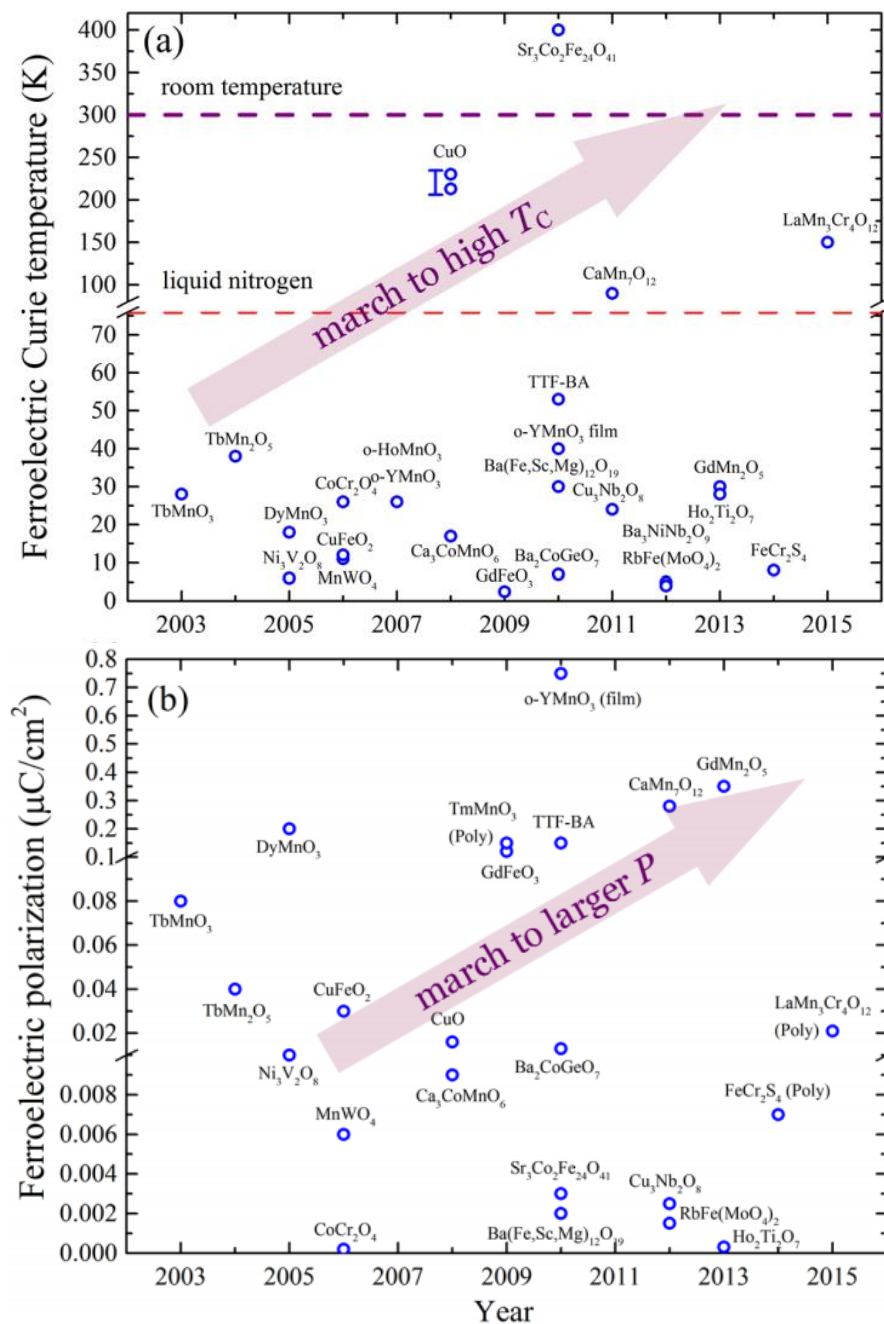
Figure 4.1: A brief summary of ferroelectricity [(a) Curie temperature and (b) polarization] of partial typical type-II multiferroics.[3]

Mousumi Sen

4.1.3: Room temperature multiferroics:

Since the renaissance of multiferroics in previous decade[13] the search for single-phase multiferroics with room temperature magneto-electric coupling has not yielded much result. There are, in fact very few materials discovered so far that show the coexistence of ferromagnetic (FM) ordering along with ferroelectric (FE) one, though some compounds like $BiFeO_3$ became hugely popular due to their antiferromagnetic (AFM) property along with FE properties[14–16]. Some of the non-stoichiometric compounds have achieved some of the desired properties through doping [17–19], although they are hard to reproduce and not suitable for large scale production. Some of the technical challenges associated with most of the compounds are – very low magnetic transition temperature, small polarization values and week coupling between them etc. Some of the room temperature and near room temperature multiferroic compounds are listed below in the table.

Mousumi Sen

Compound	Ferro-electric ordering	Magnetic ordering T	Magnetic ordering	Ref
$BiFeO_3$ (Bulk)	1103 K	643 K	Antiferromagnetic	[20]
$LuFeO_3$ Films	1050 K	440 K	Antiferromagnetic	[15]
$KNb_{0.95}Co_{0.05}O_3$	699 K	-	Weak ferromagnetism	[17]
Fe-doped $BaTiO_3$	365 K	670 K	Ferromagnetic	[21]
$BaFe_2Se_3$ (Theory)	255 K	256 K	Antiferromagnetic	[22]
$Pb(Fe_{0.5}Ta_{0.5})_{0.4}(Zr_{0.53}Ti_{0.47})_{0.6}O_3$	300 K hypothetical	475 K	Weak Ferro/ferrimagnetic	[19]
Fe_3Se_4	~317 K	~317 K	Ferrimagnetic	This work

Transition metal based chalcogenides possesses huge potential as magneto-electric materials. $CdCr_2S_4$ and $CdCr_2Se_4$ with Curie temperature 85 K and 125 K respectively were reported to show multiferroic behavior, [23] although the origin of this behavior was not clearly understood. Recently, high temperature multiferroicity was predicted in $BaFe_2Se_3$ phase, which was quite unexpected[22]. Later, it was shown experimentally with the help of photoemission spectroscopy that two kinds of electrons (localized and itinerant) coexist in $BaFe_2Se_3$ phase[24].

As discussed in earlier chapters, binary metal chalcogenide Fe_3Se_4 has gained attention quite recently because of its high uniaxial magnetic anisotropy constant without the presence of any rare earth metal or noble metal atom leading to very high coercivity at

Mousumi Sen

room temperature ($\sim$4 kOe)[25–27]. Fe_3Se_4 is ferrimagnetic at room temperature with Curie temperature $\sim$ 317 K and have monoclinic structure with a space group I2/m (12) [26]. But, till now, dielectric study of this material has not been reported either in bulk or nano forms.

In this chapter we investigate a novel and unexpected perspective of Fe_3Se_4 which establishes Fe_3Se_4 as a room temperature multiferroic material. Fe_3Se_4 shows magnetoelectric coupling at room temperature along with very strong ferrimagnetic properties which is very unique for a simple binary compound in undoped form. These behaviors are very surprising for Fe_3Se_4, as, at room temperature the single crystals of this compound is known to show metallic properties due to the overlapping of cation-cation forming bands[28].

4.1.4: Ferroelectric metals:

Metallic behavior and ferroelectricity are not mutually compatible as the conduction electrons screen the static internal electric field. In the year 1965, Anderson and Blount predicted a ferroelectric type metal showing a continuous structural transition in metallic state[29]. After almost half a century, $LiOsO_3$ was reported as the first example of a ferroelectric metal which undergoes a ferroelectric type transition at 140 K[30]. Comprehensive theoretical studies discussed the origin of ferroelectric behavior in structurally similar compound $LiNbO_3$[31]. Moreover, a new compound $MgReO_3$ was predicted to show ferroelectric metal type behavior. For a material to be termed as ferroelectric metal, the structural transition has to be continuous and the material at low temperature structure has to be ferroelectric.

Mousumi Sen

4.2: Experimental details and techniques:

Temperature dependent dielectric spectroscopy was performed using Novocontrol Beta NB Impedance Analyzer capable of measuring impedance response of sample from few µHz to MHz. the analyzer was connected with home built sample holder to couple with a helium closed cycle refrigerator (Janis Inc.) for temperature control of the sample space. The powdered sample was compressed in a hydraulic press in the form of circular pellet of diameter 13 mm and a custom designed sample holder was used to form parallel plate capacitor geometry. The principle of dielectric spectroscopy is illustrated schematically in figure 4.2.
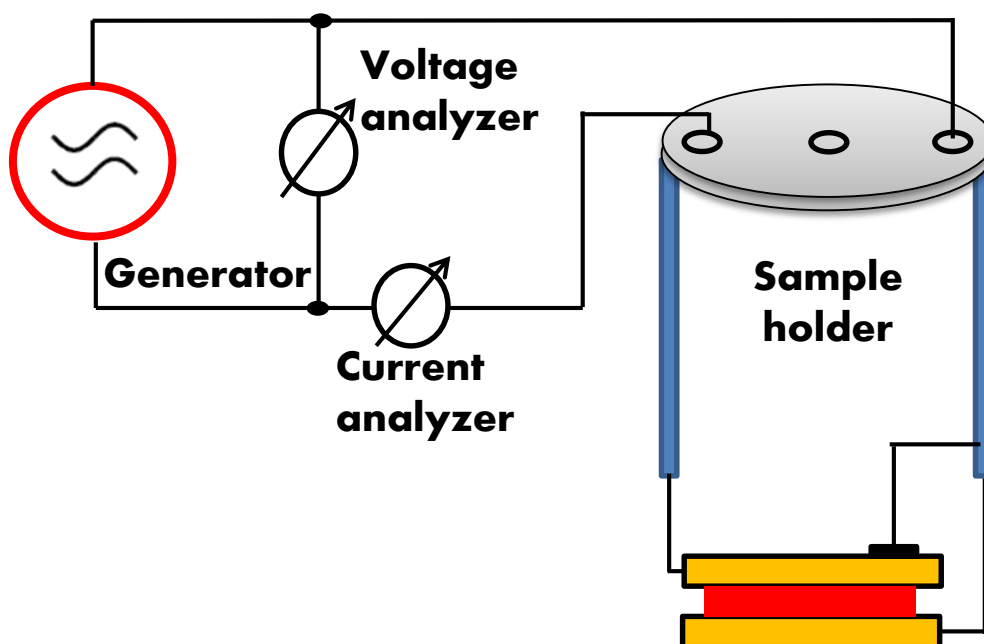

Figure 4.2: Principle of a dielectric/impedance measurement with a parallel plate geometry.

Ferroelectric hysteresis loop measurements were done with the help of a ferroelectric tester module of TF Analyzer 2000 Measurement System. Powder sample was pressed in hydraulic press on pellets of diameter 10 mm. No electric field was applied during pressing.

Raman spectra were collected using the same instrument whose details are mentioned in section 2.2.2 in chapter 2. Temperature dependent studies were done using a temperature controlling unit integrated with Raman spectrometer equipped with liquid nitrogen. For magneto-Raman measurements, a permanent bar magnet (rare-earth magnet) was kept near the sample to apply magnetic field. The intensity of magnetic field was measured with Gauss-meter. The Hall probe of the Gauss-meter was held as close as possible to the sample to get a fairly accurate idea of the magnetic field the sample is experiencing.

4.3: Results and discussion:

4.3.1: Observation of electrical polarization in Fe$_3$Se$_4$ nanorods:

The as-synthesized sample pressed in the form of pellet shows the evidence of the presence of spontaneous and reversible polarization in Fe$_3$Se$_4$ nanorods No electrical poling of the sample was done before the measurement. Figure 4.3. shows the P-E loop taken with frequency 50 Hz and at temperature 89 K, 140 K, 190 K and 240 K respectively. The hysteresis loops are symmetrical around the origin and do not show clear saturation. The shape of the P-E loops indicates towards the presence of relaxor-type ferroelectricity in these samples. The value of polarization is very small but comparable to other nanoparticles systems for e.g Fe$_3$O$_4$ and some other magnetic nanoparticles[23,32–34]. The shape of the loop resembles the hysteresis loop observed for Fe$_3$O$_4$ nanoparticles and its composites with PVDF[34]. The loop appears inflated due to significant contribution from the leakage current and other non-switchable polarization.

To evaluate the true switchable polarization Positive Up Negative Down (PUND) measurements were employed (figure 4.3.f). In PUND test, a train of 5 pulses is sent which is very efficient in extracting information regarding intrinsic ferroelectricity from the non-hysteric and leakage part. The switchable polarization is calculated as dP (as shown in figure 1f). Although, the magnitude of this true switchable polarization very small (0.08 μC/cm^2) at 240 K, but its presence confirms the intrinsic ferroelectricity in Fe$_3$Se$_4$.
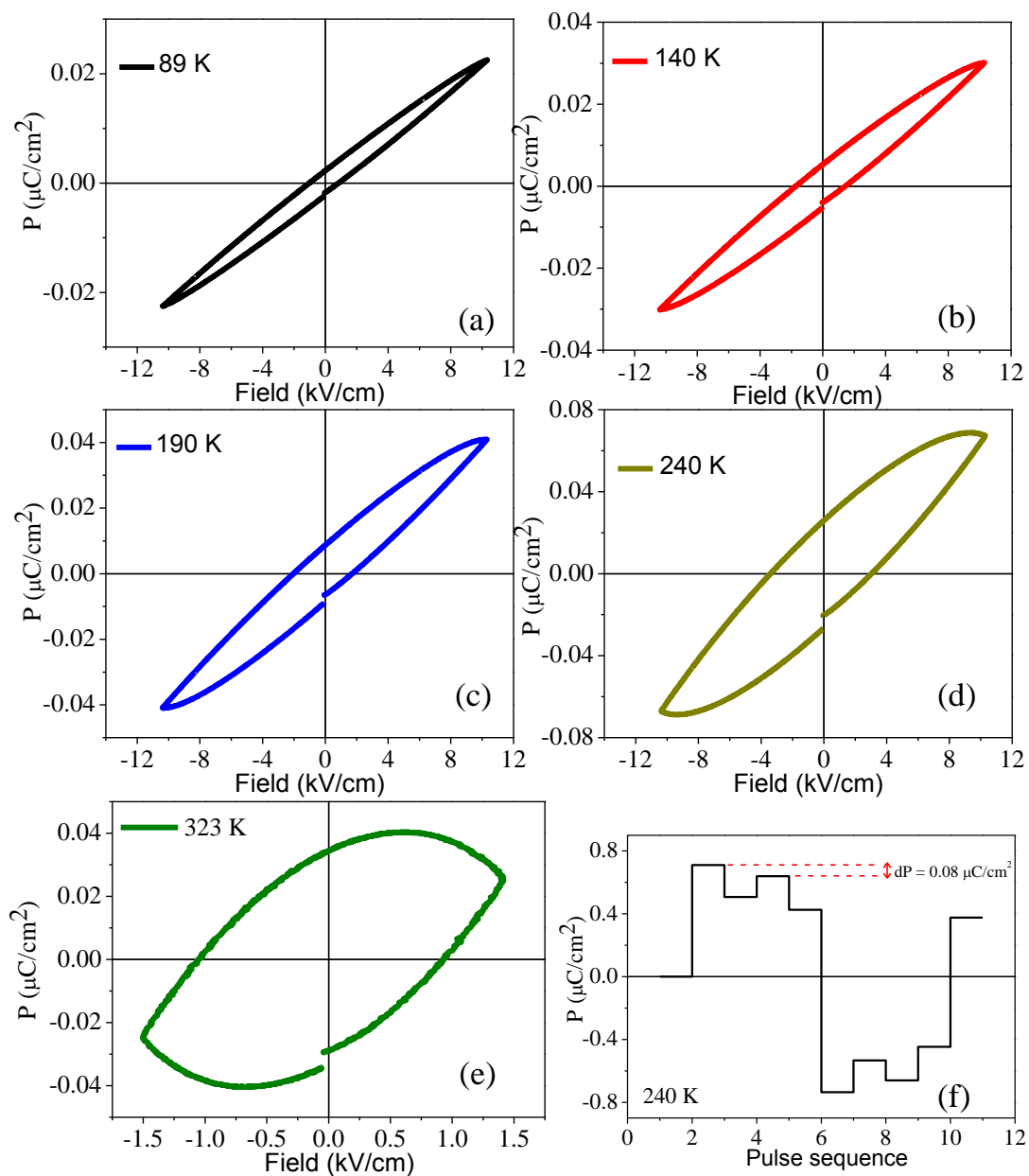
Mousumi Sen

Figure 4.3: Ferroelectric polarization loop of Fe_3Se_4 nanoparticles at frequency 50 Hz at temperatures 89, 140, 190, 240 and 323 K (a-e). The Positive-Up-Negative-Down results for knowing the true reversible polarization are shown (f) at temperature 240 K.

Mousumi Sen

4.3.2: Impedance spectroscopy:

The dielectric response from the sample was measured in a frequency range 1 Hz to 10^6 Hz spanning temperature range150 K to 350 K at 1 V rms. The frequency dependence of various parameters is plotted as a function of frequency in Figure 4.4. As perceived from the figure, both the real and out of phase part of permittivity (ε' and ε'' respectively) values decreases with increasing frequency. At low frequency, the permittivity values consists of contributions from all the dipolar, interfacial, atomic, ionic and electronic polarization, which can be explained by Maxwell-Wagner theory. The heavier dipoles are able to follow the external field at low frequency, so that values of ε are higher. As the frequency starts to increase the dipoles lag behind the field and ε value decreases. In many compounds large values of permittivity are seen owing to the presence of ionic impurities in the sample. This is revealed by high values of tan δ in these cases. Here, tan δ values of the order 10^{-1} are achieved (see figure 4.4 c).
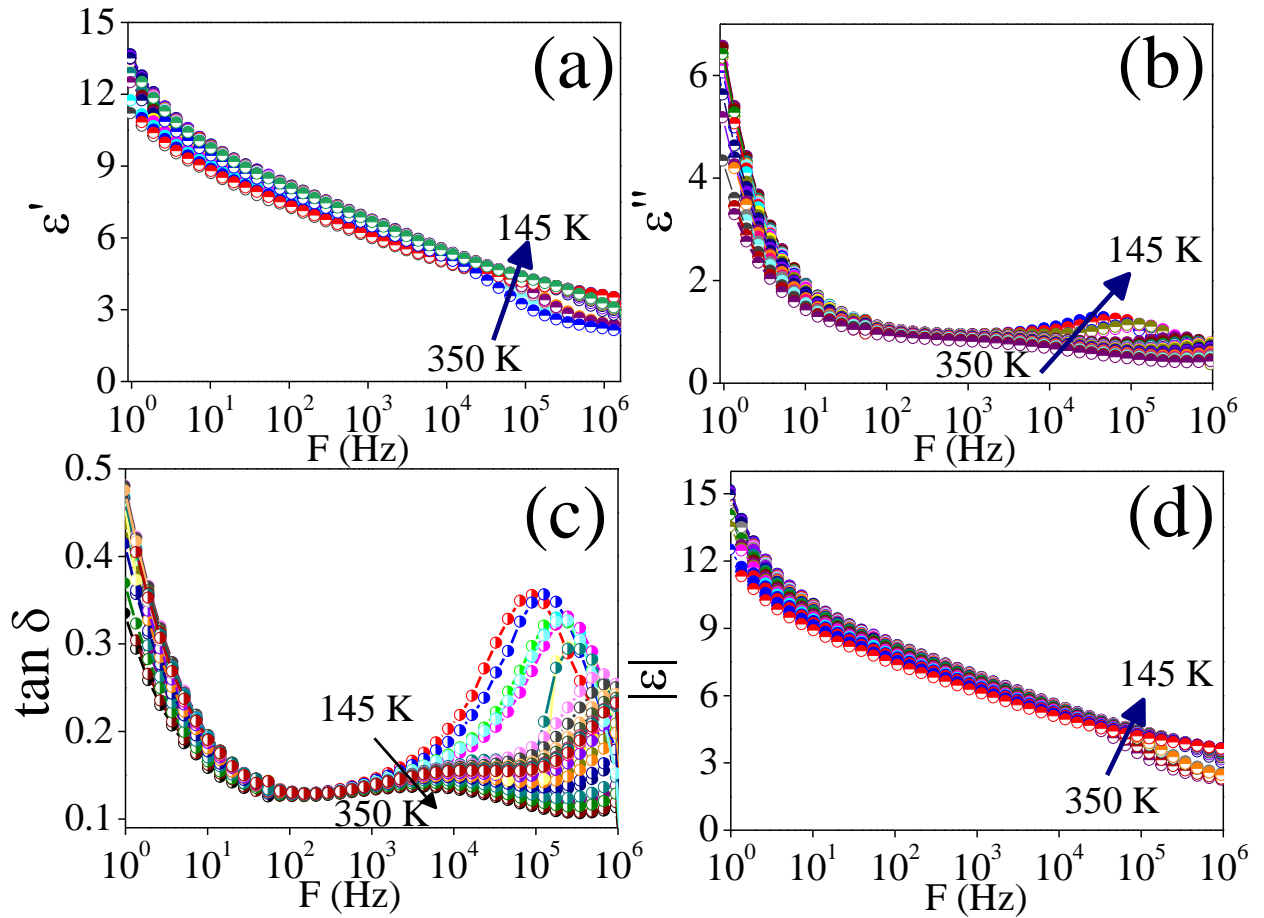
Mousumi Sen

Figure 4.4: Frequency dependence of (a) real part of permittivity (b) out of phase part of permittivity (c) loss factor (d) absolute permittivity measured with ac 1 V rms value at a temperature range from 200 K to 350 K.

The temperature dependence of ε' is extracted from the above figure (Figure 4.4) and shown in figure 4.5 at frequencies 107, 1587 and 11952 Hz. A small kink was observed around temperature 317 K in real part of ε verses temperature curve for all frequencies. For clear view the temperature dependence of dielectric constant and loss tangent is plotted in figure 4.6. The kink around the transition temperature is encircled. Above 317 K, the value of ε decreases sharply indicative of a ferroelectric to paraelectric transition.

Although the feature seen in very weak in nature, but the proximity of the kink observed with the magnetic Curie transition (T_c) in this compound indicates towards the presence of magneto-electric coupling in the compound.
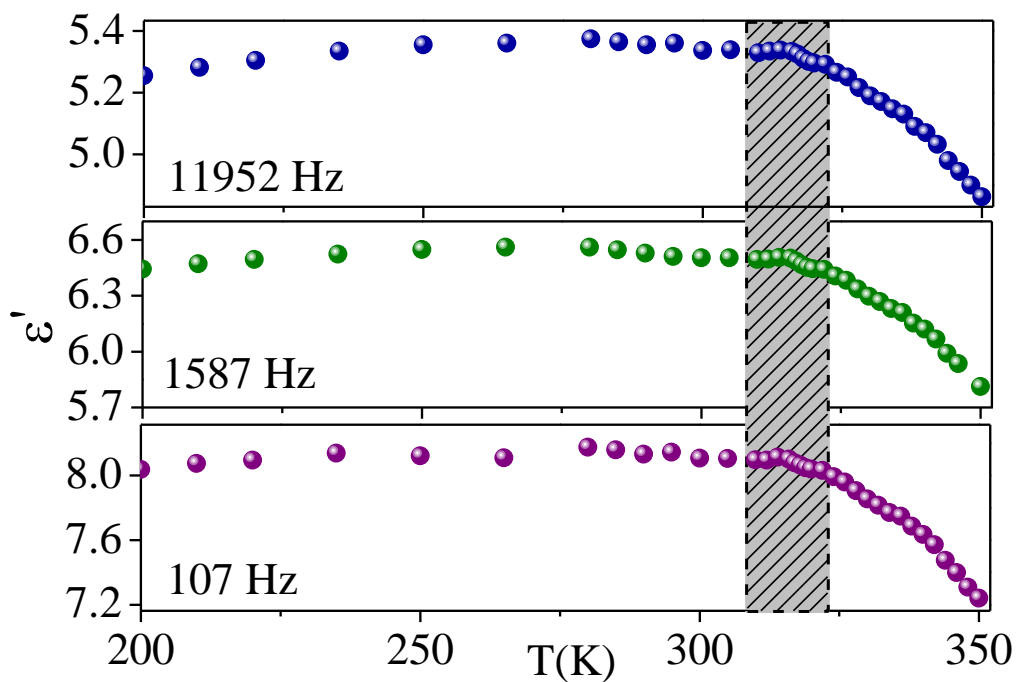

Figure 4.5: Temperature dependence of real part of permittivity at frequencies 11952 Hz, 1587 Hz, 107 Hz extracted from figure 4.4 (a). The shaded region shows the anomaly in ε' near the transition temperature.
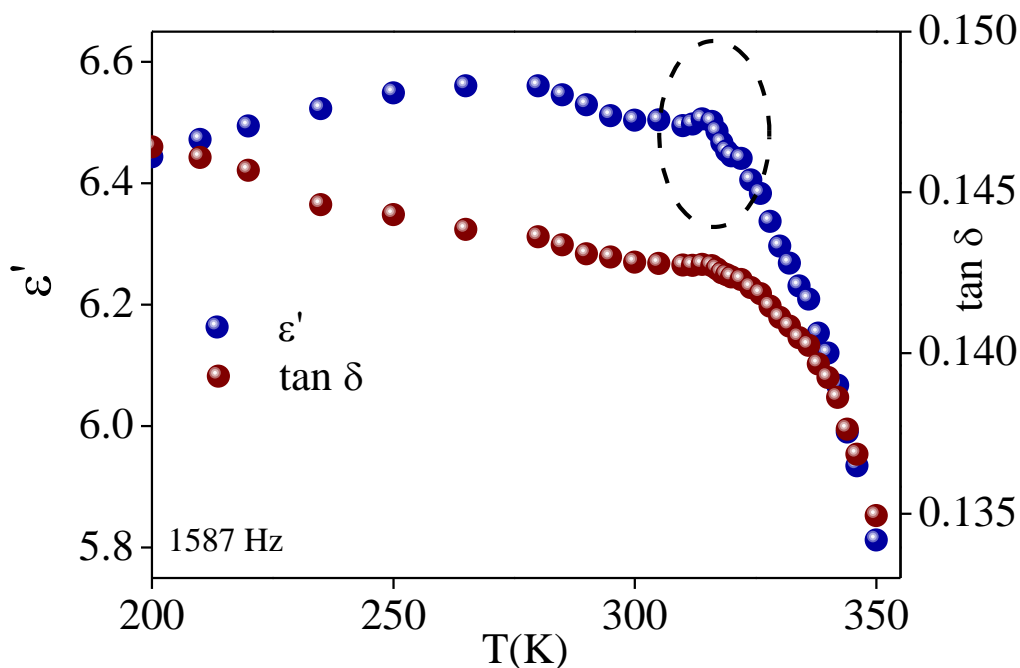
Mousumi Sen

Figure 4.6: Temperature dependence of real part of permittivity at frequency 1587 Hz and the loss tangent.

To understand the nature of dielectric relaxation in these nanorods, complex Argand plane plot ε'' and ε', also known as Cole-Cole plot, was examined. Figure 4.7 shows the plots between the real (ε') and imaginary (ε'') part of the impedance at different temperatures. It can be realized from the Cole-Cole plot that the center of the semicircle arcs are below the x-axis implying that the electrical response from the sample departs from the ideal Debye's relaxation process. As can be inferred from the figure, at very low temperatures (plots at 185 K, 220 K), there is only one semicircle which comes from the contribution from the grains. As the temperature increases and approaches near the Curie temperature another semicircle appears at lower frequency region associated with the contribution from the grain boundary (mostly the organic surfactants used in the synthesis). At Tc (~

Mousumi Sen

317 K), both the contributions from grain and grain boundary is prominent but when the temperature is raised much above Tc (plots at 336 K and 350 K), only the contributions due to grain boundary is prominent. The resistance from the grain and grain boundaries are calculated from the Cole-Cole plots and plotted against temperature in figure 4.8. The parameter α (spreading factor) characterizes the distribution of relaxation time signifying the departure from the ideal electrical response. α can be determined from the expression for the maximum value of the imaginary part of the permittivity given below.

$$\epsilon''_{max} = \frac{(\epsilon_s - \epsilon_\infty)\tan\left[(1-\alpha)\,{}^\pi/_4\right]}{2}$$

Here, ϵ_s and ϵ_∞ are the low and high frequency limit of ϵ' respectively. The spreading factor α was calculated from the above equation for both the semicircle arcs and the values for grain and grain boundary were found to be 0.54 and 0.57, respectively at 317 K. These non-zero values of α shows the poly-dispersive nature of dielectric relaxation as observed in literatures [35,36].

Mousumi Sen
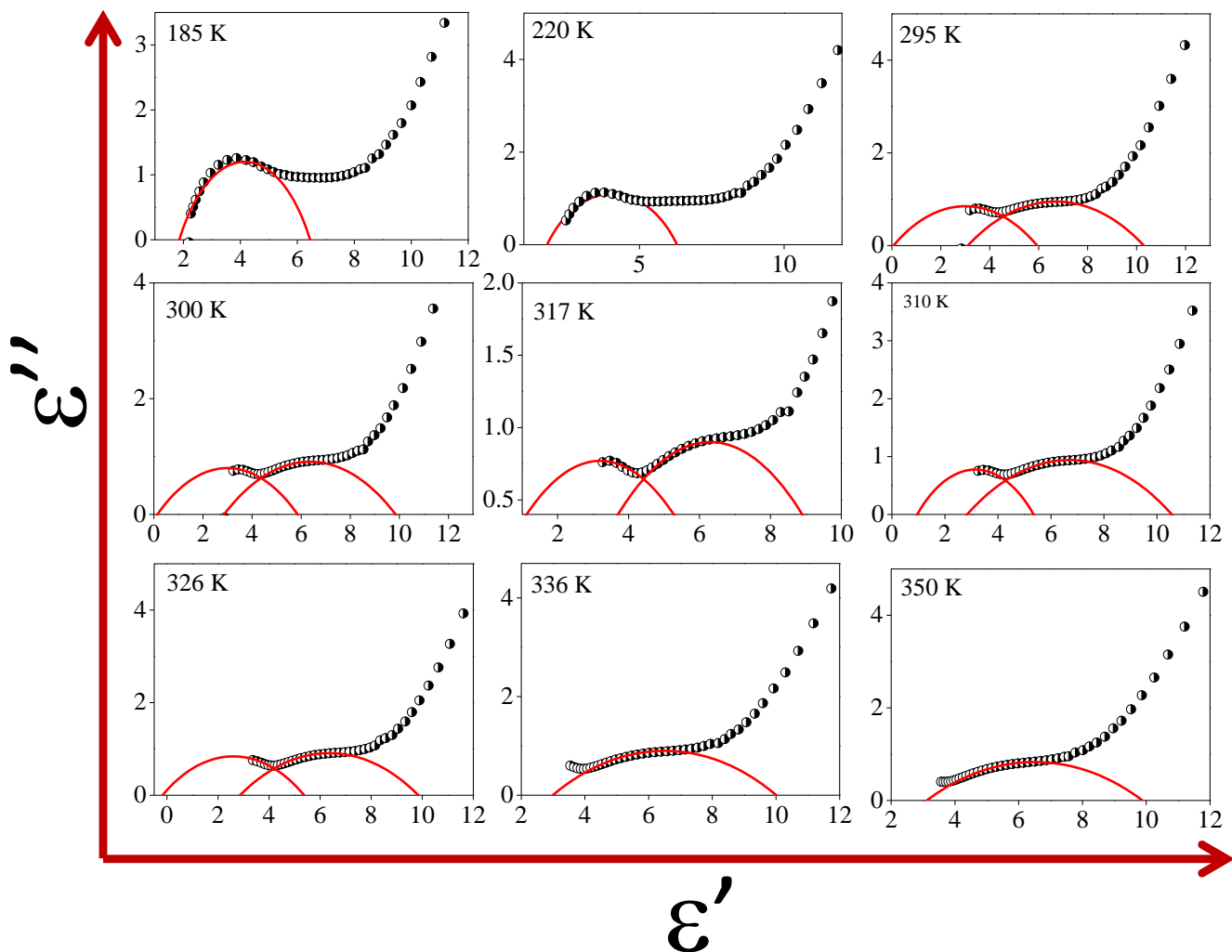
Figure 4.7: Cole-Cole plot of as synthesized Fe_3Se_4 nanoparticles (ε'' versus ε') measured by impedance spectroscopy at temperatures 185, 220, 295, 300, 317, 310, 326, 336 and 350 K respectively.

Mousumi Sen
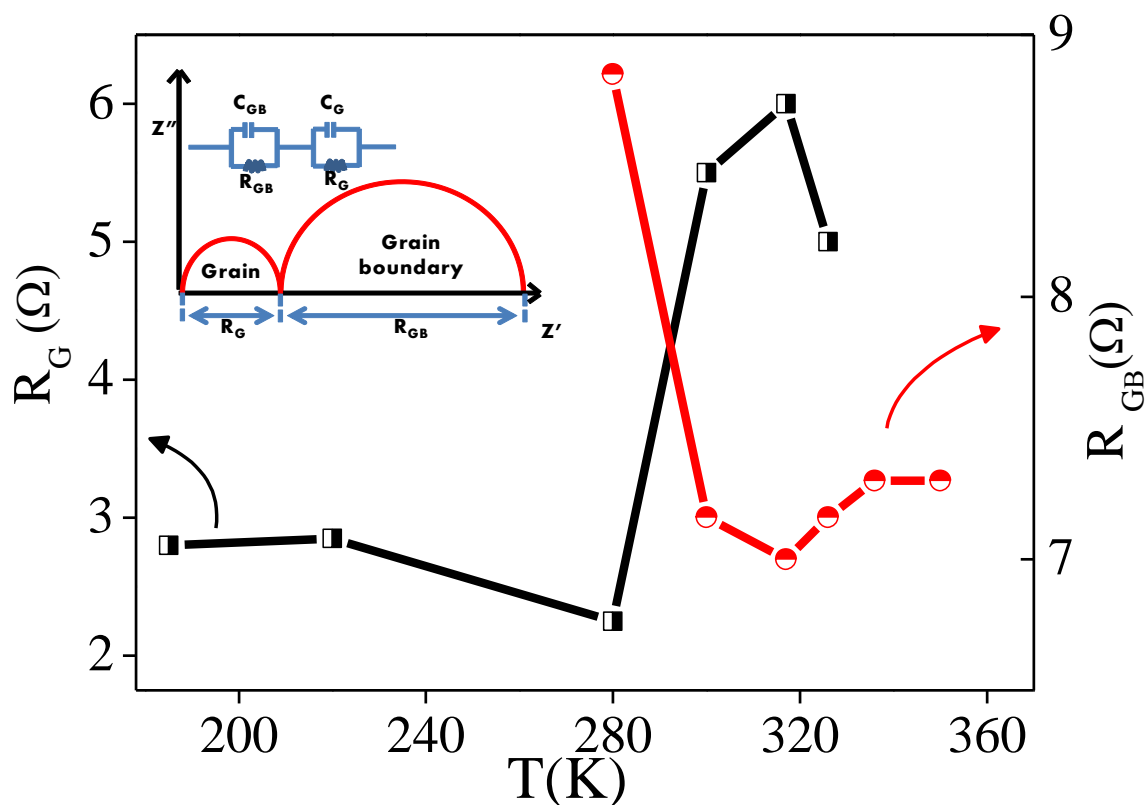
Figure 4.8: Temperature dependent of resistance contribution from grain and grain boundary extracted from Cole-Cole plot is plotted. Inset shows the circuit arrangements and parameters R_G and R_{GB} in a Cole-Cole plot.

4.3.3: Raman spectroscopy

In order to study the coupling between spin and the phonons in the present system Raman spectrum was measured from temperature 295 to 333 K. Top panel of Figure 4.9 shows the Raman spectra of as prepared Fe_3Se_4 nanoparticles taken at temperatures from 295 K to 333 K. The spectrum consists of sharp peaks at 224, 291, 409 cm^{-1}. The peak at 224 and 291 cm^{-1} can be ascribed to the Fe-Se vibration modes as it is close to the reported values of 220 and 285 cm^{-1} for the Fe-Se vibration in β-Fe_7Se_8 having similar monoclinic

Mousumi Sen

structure[37,38].As the temperature is increased, the peaks, 224, 291 cm^{-1}, show significant change in the peak position and peak width (FWHM).

To analyze the spectra, least square fit with Lorentzian line shape was used to fit the peaks. When the peak position and FWHM is plotted against temperature, a clear incongruity is seen around the magnetic/ferroeletric transition temperature ($\sim$ 317 K) (see figure 4.10 bottom panel). From the figure 4.9, it is appreciated that both the Raman modes softens as temperature is increased from 295 K. As the temperature further reaches the magnetic/ferroelectric ordering temperature the Raman mode starts hardening and peak shifts towards higher wavenumber and then immediately after T_c decreases sharply towards lower wavenumber. This anomaly in Raman modes observed near magnetic T_c provided a significant input indicating the presence of spin-phonon coupling in the system. This kind of anomaly near the magnetic transition temperature has been observed previously in case of some rare earth chromites[39], pure selenium element[40] and the concurrent anomaly around T_c is ascribed to the spin phonon coupling.

The effect of external magnetic field on these Raman modes was studied. At room temperature, (which is close to the magnetic transition temperature) even a very small external magnetic field (0.01 T) distorts the spectra significantly and intensity of Raman modes decreases sharply (Figure 4.10). The Raman signal was regained to its original form as soon as the external magnetic is removed. Raman spectra without field, without field and after removing the field are shown in figure 4.10. The external magnetic field also affects the sharpness of the peak, may be because the orderness in the sample increases with application of magnetic field. The line width of the 220 cm^{-1} peak decreases from 4.6 to 3.8 cm^{-1} with the application of external magnetic field.

Mousumi Sen

For Fe_3Se_4 single crystals it was observed that beyond magnetic ordering temperature the interatomic spacing rearranges such that the cation-cation overlapping disappears partially or completely[28].

Mousumi Sen

Mousumi Sen
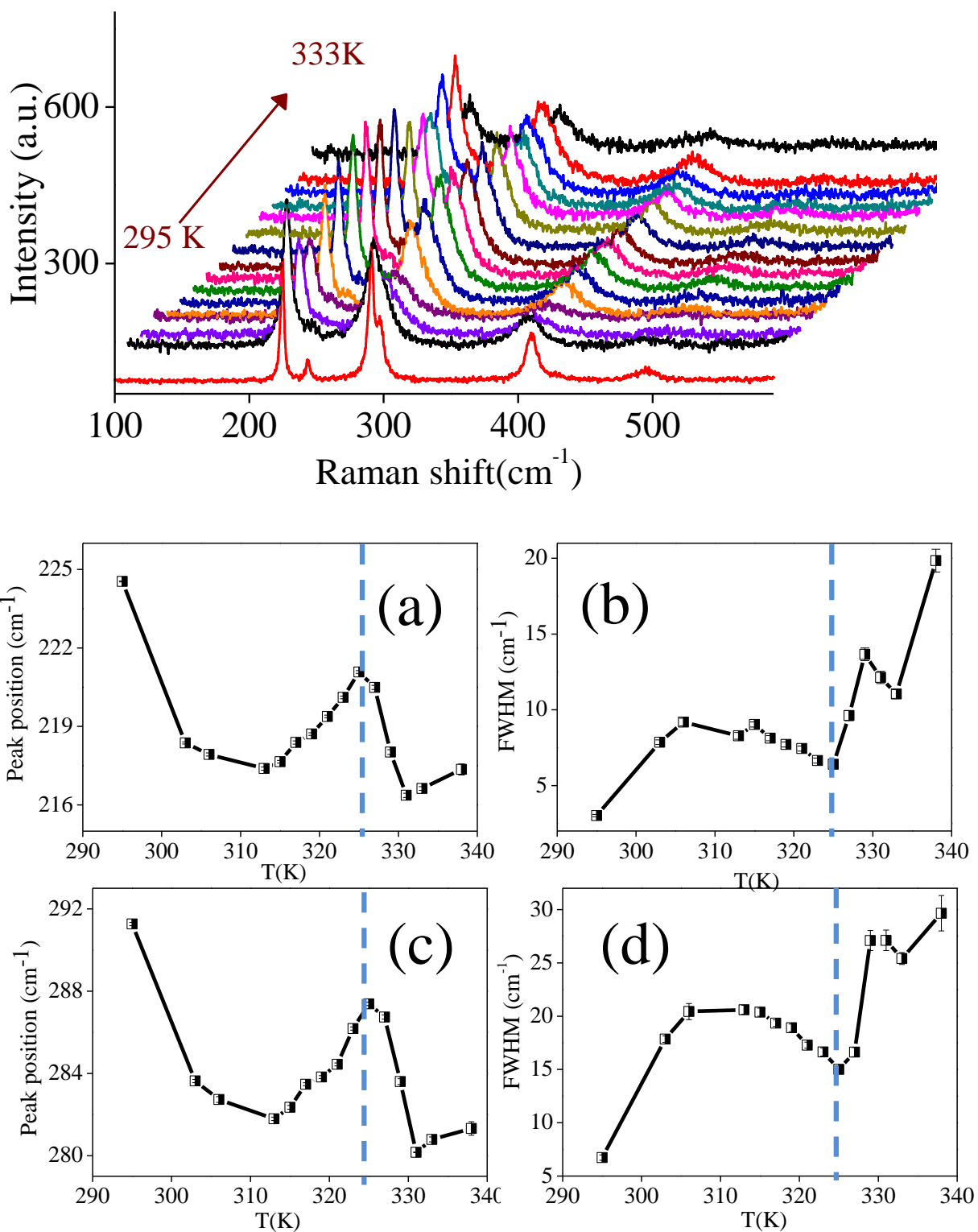
Figure 4.9: Temperature dependence of Raman scattered signal from Fe_3Se_4 nanoparticles recorded from temperature 295 K to 333 K (top panel).The peak position and FWHM of two Raman modes were deduced from these plots and plotted against temperatures (Bottom panel). (a) and (b) shows the variation for 224 cm^{-1} mode and (c) and (d) shows the variation for 291 cm^{-1} mode.
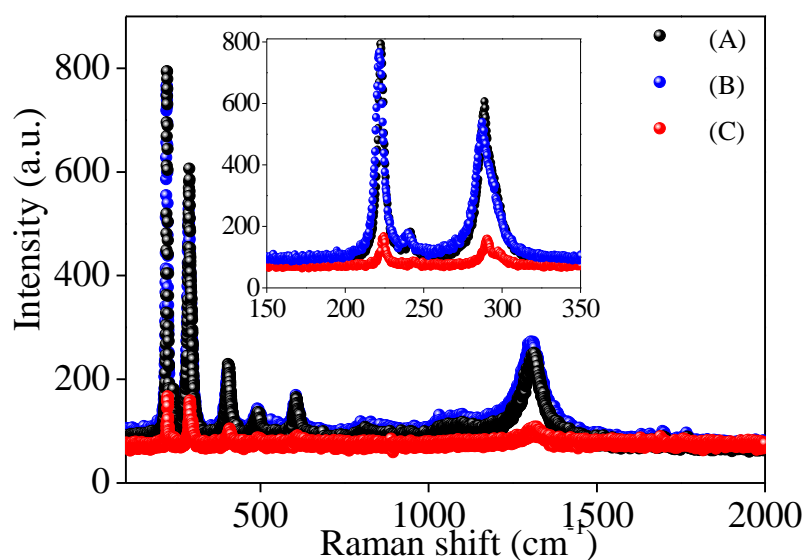
Figure 4.10: Effect of external magnetic field on the Raman mode intensity is shown. (A) shows the Raman scattering signal without exposure to external magnetic field (B) shows the Raman scattering signal after the removal of external magnetic field (C) Raman scattering signal with exposure to external magnetic field 100 Oe.

Mousumi Sen

4.3.4: Observation of spin-phonon-charge coupling:

Figure 4.11: Observation of spin-phonon-charge coupling can be seen as the anomaly seen at magnetization, dielectric permittivity, heat capacity and heat flow (from TGA measurement) at concurrent temperature indicated by the shaded region.

Mousumi Sen

The heat flow curves were measured from thermo gravimetric analysis (TGA) under nitrogen atmosphere from temperature 0 to 800 °C. A small exothermic peak was observed around 320 K, which is associated with change from paramagnetic to ferrimagnetic state. Evidence for the presence of spin-charge-phonon coupling in this system can been seen from figur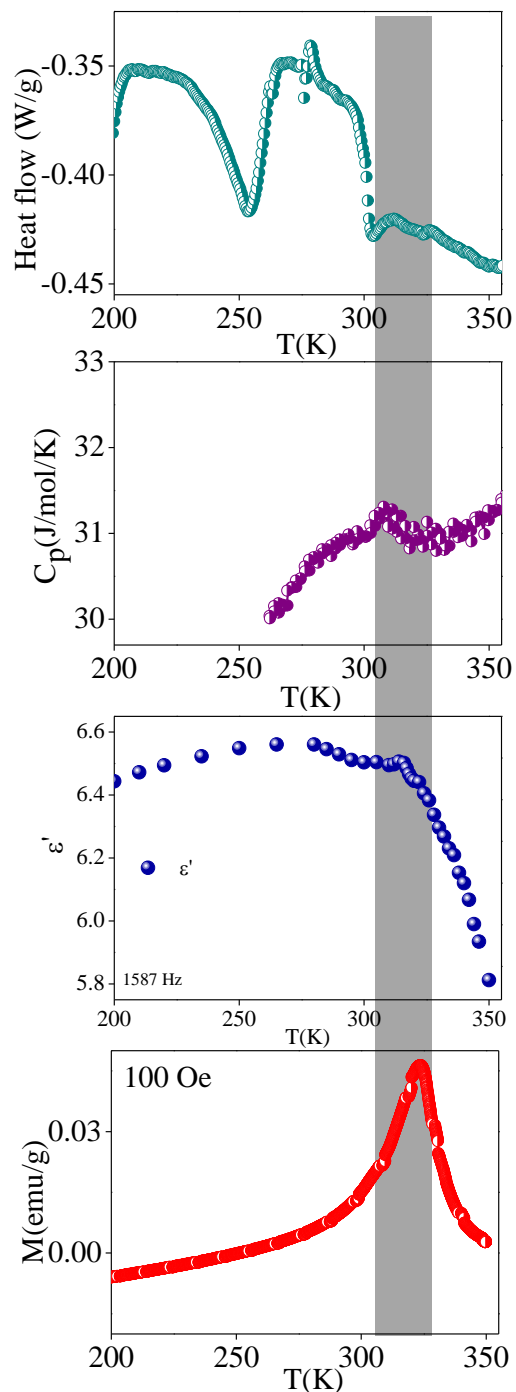e 4.11 where the magnetization (M), real part of dielectric permittivity (ε'), specific heat capacity at constant pressure (C_p) and the heat flow curves taken from thermo gravimetric analysis (TGA) measurements are plotted as a function of temperature. The anomaly in these parameters is highlighted in the shaded region.

4.4: Conclusion:

In this chapter, observation of ferroelectric order in Fe_3Se_4 nanoparticles at room temperature is discussed. These particles also show signatures of spin-charge coupling as an anomaly was observed in dielectric permittivity around magnetic transition temperature 317 K. Also, strong dependence of intensity of Raman spectra on external magnetic field indicates towards the presence of spin-phonon-charge coupling in the system. Ferroelectric polarization measurements revealed hysteresis loops in a broad frequency range. The microscopic origin of the coupling between spin-charge-phonon is not clearly understood. Vigorous theoretical calculations are required to probe this mechanism in this compound. Our important observation about the coexistence of both magnetic and charge ordering at room temperature proposes Fe_3Se_4 as a possible room temperature multiferroic compound.

Mousumi Sen

References

(1)   Khomskii, D. I. Multiferroics: Different Ways to Combine Magnetism and Ferroelectricity. *J. Magn. Magn. Mater.* **2006**, *306* (1), 1–8.

(2)   Schmid, H. Multi-Ferroic Magnetoelectrics. *Ferroelectrics* **1994**, *162* (1), 317–338.

(3)   Dong, S.; Liu, J.-M.; Cheong, S.-W.; Ren, Z. Multiferroic Materials and Magnetoelectric Physics: Symmetry, Entanglement, Excitation, and Topology. *Adv. Phys.* **2015**, *64* (5–6), 519–626.

(4)   Eerenstein, W.; Mathur, N. D.; Scott, J. F.; F, J. Scott: Multiferroic and Magnetoelectric Materials. *Nature* **2006**, *442759* (August), 759–765.

(5)   Cheong, S.-W.; Mostovoy, M. Multiferroics: A Magnetic Twist for Ferroelectricity. *Nat. Mater.* **2007**, *6* (1), 13–20.

(6)   van den Brink, J.; Khomskii, D. I. Multiferroicity due to Charge Ordering. *J. Phys. Condens. Matter* **2008**, *20* (43), 434217.

(7)   Yamauchi, K.; Fukushima, T.; Picozzi, S. Ferroelectricity in Multiferroic Magnetite Fe3O4 Driven by Noncentrosymmetric Fe2+/Fe3+ Charge-Ordering: First-Principles Study. *Phys. Rev. B* **2009**, *79* (21), 212404.

(8)   Ikeda, N.; Ohsumi, H.; Ohwada, K.; Ishii, K.; Inami, T.; Kakurai, K.; Murakami, Y.; Yoshii, K.; Mori, S.; Horibe, Y.; et al. Ferroelectricity from Iron Valence Ordering in the Charge-Frustrated System LuFe2O4. *Nature* **2005**, *436* (7054), 1136–1138.

(9)   Poddar, P.; Fried, T.; Markovich, G. First-Order Metal-Insulator Transition and Spin-Polarized Tunneling in Fe3O4 Nanocrystals. *Phys. Rev. B* **2002**, *65* (17), 3–6.

(10)   Ziese, M.; Esquinazi, P. D.; Pantel, D.; Alexe, M.; Nemes, N. M.; Garcia-Hernández, M. Magnetite (Fe 3 O 4): A New Variant of Relaxor Multiferroic? *J. Phys. Condens. Matter* **2012**, *24* (8), 86007.

(11)   Poddar, P.; Fried, T.; Markovich, G.; Sharoni, A.; Katz, D.; Wizansky, T.; Millo, O. Manifestation of the Verwey Transition in the Tunneling Spectra of Magnetite

Mousumi Sen

Nanocrystals. *Europhys. Lett.* **2003**, *64* (1), 98–103.

(12)   Alexe, M.; Ziese, M.; Hesse, D.; Esquinazi, P.; Yamauchi, K.; Fukushima, T.; Picozzi, S.; Gösele, U. Ferroelectric Switching in Multiferroic Magnetite (Fe3O 4) Thin Films. *Adv. Mater.* **2009**, *21* (44), 4452–4455.

(13)   Hill, N. a. Why Are There so Few Magnetic Ferroelectrics? *J. Phys. Chem. B* **2000**, *104* (29), 6694–6709.

(14)   Seidel, J.; Martin, L. W.; He, Q.; Zhan, Q.; Chu, Y.-H.; Rother, A.; Hawkridge, M. E.; Maksymovych, P.; Yu, P.; Gajek, M.; et al. Conduction at Domain Walls in Oxide Multiferroics. *Nat. Mater.* **2009**, *8* (3), 229–234.

(15)   Wang, W.; Zhao, J.; Wang, W.; Gai, Z.; Balke, N.; Chi, M.; Lee, H. N.; Tian, W.; Zhu, L.; Cheng, X.; et al. Room-Temperature Multiferroic Hexagonal LuFeO3 Films. *Phys. Rev. Lett.* **2013**, *110* (23), 237601.

(16)   Jaiswal, A.; Das, R.; Vivekanand, K.; Mary Abraham, P.; Adyanthaya, S.; Poddar, P. Effect of Reduced Particle Size on the Magnetic Properties of Chemically Synthesized BiFeO 3 Nanocrystals. *J. Phys. Chem. C* **2010**, *114* (5), 2108–2115.

(17)   Min, K.; Huang, F.; Lu, X.; Kan, Y.; Zhang, J.; Peng, S.; Liu, Y.; Su, J.; Zhang, C.; Liu, Z.; et al. Room-Temperature Multiferroic Properties of Co-Doped KNbO3 Ceramics. *Solid State Commun.* **2012**, *152* (4), 304–306.

(18)   Raghavan, C. M.; Kim, H. J.; Kim, J. W.; Kim, S. S. Room Temperature Multiferroic Properties of (Bi0.95La0.05)(Fe0.97Mn0.03)O3/NiFe2O4 Double Layered Thin Film. *Mater. Res. Bull.* **2013**, *48* (11), 4628–4632.

(19)   Schiemer, J.; Carpenter, M. A.; Evans, D. M.; Gregg, J. M.; Schilling, A.; Arredondo, M.; Alexe, M.; Sanchez, D.; Ortega, N.; Katiyar, R. S.; et al. Studies of the Room-Temperature Multiferroic Pb(Fe 0.5 Ta 0.5) 0.4 (Zr 0.53 Ti 0.47) 0.6 O 3 : Resonant Ultrasound Spectroscopy, Dielectric, and Magnetic Phenomena. *Adv. Funct. Mater.* **2014**, *24* (20), 2993–3002.

(20)   Wang, J.; Neaton, J. B.; Zheng, H.; Nagarajan, V.; Ogale, S. B.; Liu, B.; Viehland, D.; Vaithyanathan, V.; Schlom, D. G.; Waghmare, U. V; et al. Epitaxial BiFeO3 Multiferroic Thin Film Heterostructures. *Science* **2003**, *299* (5613), 1719–1722.

Mousumi Sen

(21) Xu, B.; Yin, K. B.; Lin, J.; Xia, Y. D.; Wan, X. G.; Yin, J.; Bai, X. J.; Du, J.; Liu, Z. G. Room-Temperature Ferromagnetism and Ferroelectricity in Fe-Doped BaTiO3. *Phys. Rev. B* **2009**, *79* (13), 134109.

(22) Dong, S.; Liu, J.-M. M.; Dagotto, E. BaFe2Se3: A High TC Magnetic Multiferroic with Large Ferrielectric Polarization. *Phys. Rev. Lett.* **2014**, *113* (18), 187204.

(23) Hemberger, J.; Lunkenheimer, P.; Fichtl, R.; Weber, S.; Tsurkan, V.; Loidl, A. Multiferroic Behavior in. *Phys. B Condens. Matter* **2006**, *378–380*, 363–366.

(24) Ootsuki, D.; Saini, N. L.; Du, F.; Hirata, Y.; Ohgushi, K.; Ueda, Y.; Mizokawa, T. Coexistence of Localized and Itinerant Electrons in BaFe2X3 (X=S and Se) Revealed by Photoemission Spectroscopy. *Phys. Rev. B* **2015**, *91* (1), 14505.

(25) Zhang, H.; Long, G.; Li, D.; Sabirianov, R.; Zeng, H. Fe 3 Se 4 Nanostructures with Giant Coercivity Synthesized by Solution Chemistry. *Chem. Mater.* **2011**, *23* (16), 3769–3774.

(26) Sen Bishwas, M.; Das, R.; Poddar, P. Large Increase in the Energy Product of Fe 3 Se 4 by Fe-Site Doping. *J. Phys. Chem. C* **2014**, *118* (8), 4016–4022.

(27) Wang, J.; Duan, H.; Lin, X.; Aguilar, V.; Mosqueda, A.; Zhao, G. Temperature Dependence of Magnetic Anisotropy Constant in Iron Chalcogenide Fe3Se4: Excellent Agreement with Theories. *J. Appl. Phys.* **2012**, *112* (10), 103905.

(28) Akhmedov, N. R.; Yalilov, N. Z.; Abdinov, D. S. Electrical Properties of Fe7Se8, Fe3Se4, and NiFe2Se4 Single Crystals. *Phys. Status Solidi* **1973**, *20* (1), K29–K31.

(29) Anderson, P. W.; Blount, E. I. Symmetry Considerations on Martensitic Transformations: "Ferroelectric" Metals? *Phys. Rev. Lett.* **1965**, *14* (13), 532–532.

(30) Shi, Y.; Guo, Y.; Wang, X.; Princep, A. J.; Khalyavin, D.; Manuel, P.; Michiue, Y.; Sato, A.; Tsuda, K.; Yu, S.; et al. A Ferroelectric-like Structural Transition in a Metal. *Nat. Mater.* **2013**, *12* (11), 1024–1027.

(31) Xiang, H. J. Origin of Polar Distortion in LiNbO3 -Type "ferroelectric" Metals: Role of A -Site Instability and Short-Range Interactions. *Phys. Rev. B* **2014**, *90* (9), 94108.

Mousumi Sen

(32)   Masud, M. G.; Ghosh, A.; Sannigrahi, J.; Chaudhuri, B. K. Observation of Relaxor Ferroelectricity and Multiferroic Behaviour in Nanoparticles of the Ferromagnetic Semiconductor La(2)NiMnO(6). *J. Phys. Condens. Matter* **2012**, *24* (29), 295902.

(33)   Hemberger, J.; Lunkenheimer, P.; Fichtl, R.; Krug von Nidda, H. -a.; Tsurkan, V.; Loidl, A. Relaxor Ferroelectricity and Colossal Magnetocapacitive Coupling in Ferromagnetic CdCr2S4. *Nature* **2005**, *434* (7031), 364–367.

(34)   Prabhakaran, T.; Hemalatha, J. Ferroelectric and Magnetic Studies on Unpoled Poly (Vinylidine Fluoride)/Fe3O4 Magnetoelectric Nanocomposite Structures. *Mater. Chem. Phys.* **2013**, *137* (3), 781–787.

(35)   Jaiswal, A.; Das, R.; Maity, T.; Vivekanand, K.; Adyanthaya, S.; Poddar, P. Temperature-Dependent Raman and Dielectric Spectroscopy of BiFeO 3 Nanoparticles: Signatures of Spin-Phonon and Magnetoelectric Coupling. *J. Phys. Chem. C* **2010**, *114* (29), 12432–12439.

(36)   Jaiswal, A.; Das, R.; Maity, T.; Poddar, P. Dielectric and Spin Relaxation Behaviour in DyFeO3 Nanocrystals. *J. Appl. Phys.* **2011**, *110* (12), 124301.

(37)   Campos, C. XRD, DSC, MS and RS Studies of Fe75Se25 Iron Selenide Prepared by Mechano-Synthesis. *J. Magn. Magn. Mater.* **2004**, *270* (1–2), 89–98.

(38)   Campos, C. E. M.; de Lima, J. C.; Grandi, T. a.; Machado, K. D.; Pizani, P. S. Structural Studies of Iron Selenides Prepared by Mechanical Alloying. *Solid State Commun.* **2002**, *123* (3–4), 179–184.

(39)   Gupta, P.; Poddar, P. Using Raman and Dielectric Spectroscopy to Elucidate the Spin Phonon and Magnetoelectric Coupling in DyCrO 3 Nanoplatelets. *RSC Adv.* **2015**, *5* (14), 10094–10101.

(40)   Pal, A.; Shirodkar, S. N.; Gohil, S.; Ghosh, S.; Waghmare, U. V; Ayyub, P. Multiferroic Behavior in Elemental Selenium below 40 K : Effect of Electronic Topology. *Sci. Rep.* **2013**, *3* (2051), 1–7.

Mousumi Sen

Chapter 5:

Conclusion and scope for future work

Mousumi Sen

Section 5.1: Conclusion:

In this thesis, efforts are dedicated to understand the physical properties and explore new properties which were not studied before in monoclinic iron selenide. As evident from the results of previous chapters, Fe_3Se_4 holds tremendous potential for both fundamental studies and technical applications.

It is observed that the magnetic properties can be tuned and optimised by modifying the parent compound Fe_3Se_4. For the manganese doped iron selenide nanostructures, the magnetization value increased from 4.84 to7.54 emu/g, without any change in the Curie temperature; which is important for its hard magnetic applications. More than 130% increase in the energy product value is obtained. The energy product of Fe_3Se_4 can be also increased by pairing it with another material with high magnetization (Fe_3O_4). With precise control over the interface and proper tuning of the size of hard and soft phases, clean single phase behaviour in the magnetization is obtained in spite of having two different crystallographic phases present in the sample. Bottom-up assemblage using pre-synthesized nanoparticles gives us precise control over the dimension of the hard and the soft phase. The magnetic properties were studied with the amount of soft phase present in the composite and the magnetic parameters were found to be enhanced monotonically with increased volume of soft phase in the nanocomposite. The Fe_3Se_4:Fe_3O_4 nanocomposite behaves as exchange spring magnet and with inclusion of 10% soft phase energy product was increased by 115%. These efforts provide possible solution for dropping or eliminating the expensive rare earth elements that are often crucial in the development of permanent magnetic materials.

As the ferrimagnetic to paramagnetic transition of Fe_3Se_4 occurs around room temperature, the material is studied for its magnetocaloric properties. Magnetization and

Mousumi Sen

heat capacity measurements were done to estimate the magnetic entropy and adiabatic temperature change. Pronounced anomaly was observed in the heat capacity that accompanies the magnetic phase transition at the Curie temperature. The heat capacity anomaly is flattened and shifted to higher temperatures by the application of a magnetic field and correlate well with the behaviour of the anomalies in the magnetization. Maximum 0.27 K change in temperature is observed for a field change of 5 T at 317 K.

The most important and fundamental result of this work is the observation of ferroelectric order in Fe_3Se_4 nanoparticles at room temperature. These particles also show signatures of spin-charge coupling as an anomaly was observed in dielectric permittivity around magnetic transition temperature 323 K. Also, strong dependence of intensity of Raman spectra on external magnetic field indicates towards the presence of spin-phonon-charge coupling in the system. Ferroelectric polarization measurements revealed hysteresis loops in a broad frequency range. The microscopic origin of the coupling between spin-charge-phonon is not clearly understood. Our important observation about the coexistence of both magnetic and charge ordering at room temperature proposes Fe_3Se_4 as a possible room temperature multiferroic compound.

Mousumi Sen

Section 5.2: Scope of future work

The monoclinic phase of iron selenide (Fe_3Se_4) has been studied for last seven decades now; still, this material is full of surprises. Although the oxygen counterpart of the material, magnetite (Fe_3O_4), has always been in the limelight among the researchers for its widespread applications, Fe_3Se_4 is relatively very less explored and understood. As seen from the earlier chapters, Fe_3Se_4 has huge potential both in the fields of fundamental understandings of some physical processes and applications in modern technologies.

As discussed, the semi hard magnetic property is the key attraction of this material. The low magnetization of Fe_3Se_4 has to be increased to bring the sample to the permanent magnet market. Also, the energy product of the sample is highly dependent on processing of the material. The application of high magnetic fields during the pressing of powder samples to pellets helps in orienting the sample along the fields eventually increasing the energy product to much higher values. The study of effect of external magnetic field and shape anisotropy on the hard magnetic properties is subject to future research in this field.

The most important and surprising observations regarding the ferroelectric properties of Fe_3Se_4 nanoparticles were made in this thesis. But, the microscopic origin of spontaneous and polarization in Fe_3Se_4 is not clearly understood. To understand the intrinsic nature of ferroelectricity and effect of particle size on the ferroelectric properties, studies on single crystal and bulk polycrystalline samples are required. For understanding the mechanism of ferroelectricity, the magneto-electric coupling detail theoretical study is necessary.

The presence of both ferrimagnetic and ferroelectric ordering at room temperature makes Fe_3Se_4 a potential room temperature multiferroic. However, the polarization value is very small at room temperature. There is huge scope of improvement in the ferroelectric properties to make the material suitable for practical applications. Also, it will be very

Mousumi Sen

interesting to study this material in thin film form. It has been seen in some cases that the polarization values increases many fold when the material is casted in the form of thin films (for e.g. bismuth ferrite, $BiFeO_3$).

It will be challenging to address the dual nature of Fe_3Se_4 as it behaves as metal and ferroelectric both at the same time. This behaviour is extremely rare and has been found experimentally to exist in only one material till now ($LiOsO_3$) and predicted in few other materials. The metallic and ferroelectric behaviour are traditionally mutually exclusive and therefore, it will be exciting to study the origin and nature of such dual behaviour.

There are ample scopes of study for the applications of Fe_3Se_4 nanoparticles as theranostic agents in photo-thermal therapy, where these nanoparticles may absorb laser irradiations and burn the cancer cells.

Mousumi Sen

List of publications:

1) Large Increase in the Energy Product of Fe_3Se_4 by Fe-Site Doping, **Mousumi Sen Bishwas**, Raja Das, and Pankaj Poddar, *J. Phys. Chem. C* 2014, **118**, 4016−4022.http://pubs.acs.org/doi/abs/10.1021/jp411956q

2) Study of magnetic entropy and heat capacity in ferrimagnetic Fe_3Se_4 nanorods, **Mousumi Sen Bishwas**, Pankaj Poddar, *Journal of Physics D: Applied Physics* 49 (19), 195003-195008 http://iopscience.iop.org/article/10.1088/0022-3727/49/19/195003

3) Exchange spring mechanism induced enhancement in the energy product of magnetically hard-soft Fe_3Se_4:Fe_3O_4 nanocomposites with excellent interface coupling, **Mousumi Sen Bishwas**, Raja Das, and Pankaj Poddar, *communicated*.

4) Evidence of room temperature multiferroicity in Fe_3Se_4, **Mousumi Sen Bishwas**, and Pankaj Poddar, *communicated*.

5) Construction of Polynuclear Lanthanide (Ln = DyIII, TbIII, and NdIII) Cage Complexes Using Pyridine−Pyrazole-Based Ligands: Versatile Molecular Topologies and SMM Behavior, SukhenBala, **Mousumi Sen Bishwas**, BhaskarPramanik, SumitKhanra, Katharina M. Fromm, Pankaj Poddar, and RajuMondal, *Inorganic chemistry*, 54 (17), 8197-8206

6) Observation of Magnetic Anomalies in One-Step Solvothermally Synthesized Nickel-Cobalt Ferrite Nanoparticles, Gopal Datt, **Mousumi Sen Bishwas**, M. Manivel Raja and A. C. Abhyankar, *Nanoscale* 8 (9), 5200-5213

7) Room temperature vapour phase detection of nitro analytes by MOF UiO-67 through Raman signal quenching, **Mousumi Sen Bishwas**, Sanjog Nagarkar, S.K. Ghosh, Pankaj Poddar. (Manuscript under preparation)

Mousumi Sen